

REPORT DOCUMENTATION PAGE

Form Approved
OMB No. 0704-0188

Public reporting burden for this collection of information is estimated to average 1 hour per response, including the time for reviewing instructions, searching existing data sources, gathering and maintaining the data needed, and completing and reviewing the collection of information. Send comments regarding this burden estimate or any other aspect of this collection of information, including suggestions for reducing this burden, to Washington Headquarters Services, Directorate for Information Operations and Reports, 1215 Jefferson Davis Highway, Suite 1204, Arlington, VA 22202-4302, and to the Office of Management and Budget, Paperwork Reduction Project (0704-0188), Washington, DC 20503.

1. AGENCY USE ONLY (Leave blank)		2. REPORT DATE 25 July 1995	3. REPORT TYPE AND DATES COVERED
4. TITLE AND SUBTITLE Thin Film Growth with Ions, Clusters, and Metal Compounds			5. FUNDING NUMBERS
6. AUTHOR(S) John H. Weaver			
7. PERFORMING ORGANIZATION NAME(S) AND ADDRESS(ES) University of Minnesota Department of Chemical Eng. & Materials Science 421 Washington Avenue, SE Minneapolis, MN 55455			8. PERFORMING ORGANIZATION REPORT NUMBER
9. SPONSORING/MONITORING AGENCY NAME(S) AND ADDRESS(ES) U.S. Army Research Office P.O. Box 12211 Research Triangle Park, NC 27709-2211			10. SPONSORING/MONITORING AGENCY REPORT NUMBER
11. SUPPLEMENTARY NOTES The views, opinions and/or findings contained in this report are those of the author(s) and should not be construed as an official Department of the Army position, policy, or decision, unless so designated by other documentation.			
12a. DISTRIBUTION/AVAILABILITY STATEMENT Approved for public release; distribution unlimited.			12b. DISTRIBUTION CODE
13. ABSTRACT (Maximum 200 words) This is a final report for Grant number DAAL03-92-G-0216. Research accomplishments obtained through this grant are described herein. A list of publications and participating scientific personnel is also included, as are copies of the publications and reprints.			

19951005 038

DTIC QUALITY INSPECTED 5

14. SUBJECT TERMS Clusters; ions; energetic depositions; sputtering			15. NUMBER OF PAGES 57
			16. PRICE CODE
17. SECURITY CLASSIFICATION OF REPORT UNCLASSIFIED	18. SECURITY CLASSIFICATION OF THIS PAGE UNCLASSIFIED	19. SECURITY CLASSIFICATION OF ABSTRACT UNCLASSIFIED	20. LIMITATION OF ABSTRACT UL

Thin Film Growth with Ions, Clusters, & Metal Organic Compounds

Final Report

J.H. Weaver

15 July 1995

U.S. Army Research Office

Grant Number DAAL03-92-G-0216

University of Minnesota

Accession. For	
NTIS CRA&I	<input checked="checked" type="checkbox"/>
DTIC TAB	<input type="checkbox"/>
Unannounced	<input type="checkbox"/>
Justification	
By	
Distribution /	
Availability Codes	
Dist	Avail and/or Special
A-1	

Approved for public release;
distribution unlimited

The view, **opinions**, and/or findings contained in this report are those of the author and **should not be construed** as an official Department of the Army position, policy, or decision unless so designated by other documentation.

TABLE OF CONTENTS

List of Appendixes	1
Statement of the Problem Studied	2
Summary of the Most Important Results	2
List of All Publications and Technical Reports.....	5
List of All Scientific Personnel.....	6
Report of Inventions	6
Appendixes.....	7
Appendix 1: Reprint of Supersonic Cluster Source with Mass Selection and Energy Control.....	8
Appendix 2: Reprint of Interaction of 300-5000 eV Ions with GaAs(110).....	14
Appendix 3: Preprint of Vacancy Kinetics and Sputtering on GaAs(110).....	17
Appendix 4: Preprint of Ion Sputtering of GaAs(110): From Individual Bombardment Events to Multilayer Removal.....	32
Appendix 5: Preprint of Trends in Surface Rougning: STM Analyses of Ion-Sputtered GaAs(110).....	50

LIST OF APPENDIXES

- Appendix 1: Reprint of "Supersonic Cluster Source with Mass Selection and Energy Control," by R.T. Laaksonen, D.A. Goetsch, D.W. Owens, D.M. Poirier, F. Stepniak, and J.H. Weaver. Published in Rev. Sci. Instrum. **65**, 2267-2275 (1994).
- Appendix 2: Reprint of "Interaction of 300-5000 eV Ions with GaAs(110)," by X.S. Wang, R.J. Pechman, and J.H. Weaver. Published in Appl. Phys. Lett. **65**, 2818-2820 (1994).
- Appendix 3: Preprint of "Vacancy Kinetics and Sputtering on GaAs(110)," by R.J. Pechman, X.-S. Wang, and J.H. Weaver. To be published in Phys. Rev. B.
- Appendix 4: Preprint of "Ion Sputtering of GaAs(110): From Individual Bombardment Events to Multilayer Removal," by X.-S. Wang, R.J. Pechman, and J.H. Weaver. To be published in J. Vac. Sci. Technol.
- Appendix 5: Preprint of "Trends in Surface Roughening: STM Analyses of Ion-sputtered GaAs(110)," by X.-S. Wang, R.J. Pechman, and J.H. Weaver. Submitted to Phys. Rev. Lett.

STATEMENT OF PROBLEM STUDIED

The central theme of the project involved the interaction of ionized beams with solid surfaces. Such studies are relevant to materials synthesis problems because advanced manufacturing processes involve thin film growth and etching under conditions where energetic ions and clusters are present. While it is known that these ions play an important role, the details of their interactions are poorly understood.

A significant part of the program during this funding period dealt with the development of instrumentation that would allow the formation of a beam of ionized clusters, the selection from that beam of those clusters that had a particular mass and energy, and then the deposition of those clusters onto a surface with full control over the parameters of deposition. The source was successfully built and tested. The goal was to study the atomic-scale processes of this ionized cluster beam deposition (ICBD). The plan was to use scanning tunneling microscopy to characterize the clusters that were deposited and to determine the effect on the surface as a function of cluster energy and cluster size.

SUMMARY OF MOST IMPORTANT RESULTS

During 1992 and 1993, we designed and constructed the ionized cluster beam deposition system, developing what is a state-of-the-art source for mass selected and energy selected ions (discussed in end-of-year-reports). In 1994, we completed construction and interfaced the source with one of our scanning tunneling microscopy systems. Early studies showed that the structures of the ionized clusters were modified upon deposition and that the role of the support would preclude analysis as to cluster morphology. Moreover, studies of the flux of large clusters from the source indicated that the number was insufficient to allow formation of a thin film via this technique with complete mass selection. While alternatives were identified that could allow a 100-fold increase in flux of large clusters, the expense of such a procedure was judged to be too great. Accordingly, a different set of experiments were undertaken that emphasized the interaction of small ionized clusters (monomers, dimers, trimers) with a surface. This represents the thrust of the follow-on program.

Several studies were completed that examined the interaction of nonreactive ions of Ar and Xe with GaAs(110). These studies were done in parallel with instrumentation development, using

the STM and a conventional ion source. In a first series of studies, we investigated in detail the effects of ion mass (Ar^+ , Xe^+), energy (0.3 - 5 keV), trajectory, and sample temperature on ion sputtering processes for GaAs(110). Scanning tunneling microscopy images revealed that most ion bombardment events at 300 K created pits that were 1–5 unit cells in size, indicating that direct knock-on collisions dominated. The average pit size increased only moderately with ion energy. However, the pit size showed a significant dependence on the incident angle. Vacancies were sufficiently mobile at 625–775 K that vacancy islands formed and the yield could be determined directly. The sputtering yields for these nearly ideal surfaces exhibited structure that could be related to the nuclear stopping power and ion channeling, showing the influence of such geometric factors as surface path-length, ion radius, and projected atom column density. Temperature dependent results for monolayer and multilayer sputtering showed that adatoms ejected onto the surface refilled vacancies but that the surface roughness, as measured by surface width, increased with ion fluence. While inter-layer atomic transport was measurable at 625 K and increased with temperature, it was not sufficient to achieve layer-by-layer removal because As_x desorption competed with interlayer transport above ~800 K.

In the second series of studies, we emphasized the evolution of the vacancy islands on GaAs(110). Again, bombardment of the surface at $300 \leq T \leq 775$ K with Ar^+ ions at normal incidence created surface-layer defects, as shown by scanning tunneling microscopy. Vacancies produced in this way diffused via thermal activation to form single-layer vacancy islands. The diffusion of divacancies favored $[1\bar{1}0]$, and accommodation at islands produced approximately isotropic islands. Modeling of growth showed an overall Arrhenius behavior for diffusion with an activation energy of 1.3 ± 0.2 eV. Investigations of the surface morphology during multilayer erosion revealed deviation from layer-by-layer removal with scaling exponents between 0.4 and 0.5 for $625 \leq T \leq 775$ K.

In the third series of studies, we evaluated trends in surface roughening during exposure to energetic beams. For non-reactive ion sputtering of GaAs(110), we investigated the effects of diffusion kinetics on surface roughness by measuring the dependence of the surface width and step density on the amount of material removed as a function of temperature. We found that surfaces that were characterized by the removal of several monolayers of material at 625 K were rougher on a small scale than those sputtered at 725 K. These same surfaces were smoother on a large scale. Following detailed analysis using STM to relate local surface morphology to sputtering conditions,

we concluded that the increased large-scale roughness at high temperature was caused by increased atom diffusion on terraces and along step edges under conditions where there was insufficient cross-step transport to give smooth surfaces. Such atomic scale insights are relevant to sputtering of surfaces, on the one hand, and to growth of films on the other since the surface mechanisms responsible for the morphology are common to both processes.

LIST OF PUBLICATIONS

1. R.T. Laaksonen, D.A. Goetsch, D.W. Owens, D.M. Poirier, F. Stepniak, and J.H. Weaver, "Supersonic Cluster Source with Mass Selection and Energy Control," *Rev. Sci. Instr.* **65**, 2267-2275 (1994).
2. X.-S. Wang, R.J. Pechman, and J.H. Weaver, "Interaction of 300-5000 eV Ions with GaAs(110)," *Appl. Phys. Lett.* **65**, 2818-2820 (1994).
3. R.J. Pechman, X.-S. Wang, and J.H. Weaver, "Vacancy Kinetics and Sputtering on GaAs(110)," *Phys. Rev. B* (in press).
4. X.-S. Wang, R.J. Pechman, and J.H. Weaver, "Ion Sputtering of GaAs(110): From Individual Bombardment Events to Multilayer Removal," *J. Vac. Sci. Technol.* (in press).
5. X.-S. Wang, R.J. Pechman, and J.H. Weaver, "Trends in Surface Roughening: STM Analyses of Ion-sputtered GaAs(110)," *Phys. Rev. Lett.* (submitted).

Invited papers:

1. J.H. Weaver, "Photoelectron Spectroscopy and STM of Etched Semiconductor Surfaces," Gordon Research Conference on Excitations at Semiconductor Surfaces -- Fundamental Concepts and Application to Semiconductor Processing, Oahu, November 1994.
2. J.H. Weaver, "STM Characterization of Surface Processing," Microphysics of Surfaces, Santa Fe, February 1994.
3. J.H. Weaver, "STM Imaging of Atomic Scale Processes," Gordon Research Conference on Dynamics at Surfaces, Andover, August 1995.

Contributed papers:

1. X.-S. Wang, R.J. Pechman, and J.H. Weaver, "Scanning Tunneling Microscopy Studies of Ion Bombardment of GaAs(110)," March Meeting of the American Physical Society, Pittsburgh, March 1994.
2. R.J. Pechman, X.-S. Wang, and J.H. Weaver, "Sputtering of GaAs(110) Studied with Scanning Tunneling Microscopy," 41st National Symposium of the American Vacuum Society, Denver, October 1994.
3. J. Brake, X.-S. Wang, and J.H. Weaver, "STM Study of Ge Growth on Sputtered GaAs(110)," 42nd National Symposium of the American Vacuum Society, Minneapolis, October 1995.
4. X.-S. Wang, R.J. Pechman, and J.H. Weaver, "Trends in Surface Roughening: STM Analyses of Ion-Sputtered GaAs(110)," 42nd National Symposium of the American Vacuum Society, Minneapolis, October 1995.

SCIENTIFIC PERSONNEL SUPPORTED BY THIS PROJECT

1. R.T. Laaksonen, postdoc (partial)
2. X.-S. Wang, postdoc (partial)
3. R.J. Pechman, graduate student (partial)
4. Duane Goetsch, graduate student
5. Dale Owens, graduate student (partial)

REPORT OF INVENTIONS (BY TITLE ONLY):

There were no inventions under this grant.

APPENDIXES

Appendix 1

Reprint of "Supersonic Cluster Source with Mass Selection and Energy Control"

R.T. Laaksonen, D.A. Goetsch, D.W. Owens, D.M. Poirier,
F. Stepniak, and J.H. Weaver

Published in Rev. Sci. Instrum. **65**, 2267-2275 (1994).

Supersonic cluster source with mass selection and energy control

R. T. Laaksonen, D. A. Goetsch, D. W. Owens, D. M. Poirier, F. Stepniak, and J. H. Weaver

Department of Materials Science and Chemical Engineering, University of Minnesota, Minneapolis, Minnesota 55455

(Received 15 December 1993; accepted for publication 4 April 1994)

We have developed an apparatus that produces an ionized beam of mass selected clusters of controllable energy. It uses a pulse of second-harmonic light from a Nd:YAG laser to vaporize atoms from a target disk. The clustering rate of the atoms in this expanding plume is controlled with the pressure of a He pulse injected from a fast pulsed valve. A Wiley-McLaren type time-of-flight mass spectrometer with a shield lens is used to monitor the cluster distribution and to optimize the control parameters of the system. The shield lens doubles the resolution and the signal-to-noise ratio of the spectrometer. A 4000 amu rf quadrupole with 1.2 amu resolution is used to select the mass of charged clusters. An electrostatic quadrupole is used to separate the charged clusters from the neutral clusters and the He gas. The ionized clusters are then focused onto a suitably prepared substrate by using electrostatic lenses. Time averaged deposition current densities on the order of 100 pA cm^{-2} have been measured when the vaporization laser is fired at 10 Hz. The deposition energy of the clusters is controlled by applying a bias voltage to the substrate. A mobile vacuum chamber is used to transfer samples to various diagnostic systems.

I. INTRODUCTION

An understanding of the nucleation and the growth kinetics for thin films is crucial to our ability to control the formation of these films. Film growth, as used in modern optical components and microelectronic circuits, has traditionally been controlled via the deposition rate and the substrate temperature. Control over the deposition energy is, in general, exercised by exposing the substrate during the deposition process to a beam of accelerated ions.¹ Further control over film growth can be achieved if the form in which the material is deposited is also restricted. This is the idea behind the ionized cluster beam (ICB) technique developed by Takagi and co-workers at the University of Kyoto.² In the ICB technique, part of the material is deposited in the form of large energetic ionized clusters that are thought to provide good initial nucleation sites.³ This technique has been used to grow high quality metal, semiconductor, insulator, and organic films on semiconductor or insulator substrates at room temperature.⁴ However, the ICB technique has remained controversial. Indeed, experiments have shown that the number of large ionized clusters in the ICB apparatus is very small and it has been questioned whether clusters have anything to do with film quality.^{5,6}

To our knowledge, there has been no cluster-assisted film growth experiment done where the size and amount of the deposited clusters have been well known. On the other hand, where the mass and number of deposited clusters has been known, the focus has been on the chemical, geometric, and electronic properties of isolated supported clusters.⁷⁻⁹ In those experiments, the deposition energy has been a few eV whereas the best results with the ICB technique have been achieved when the deposition energy is of the order of a few keV.

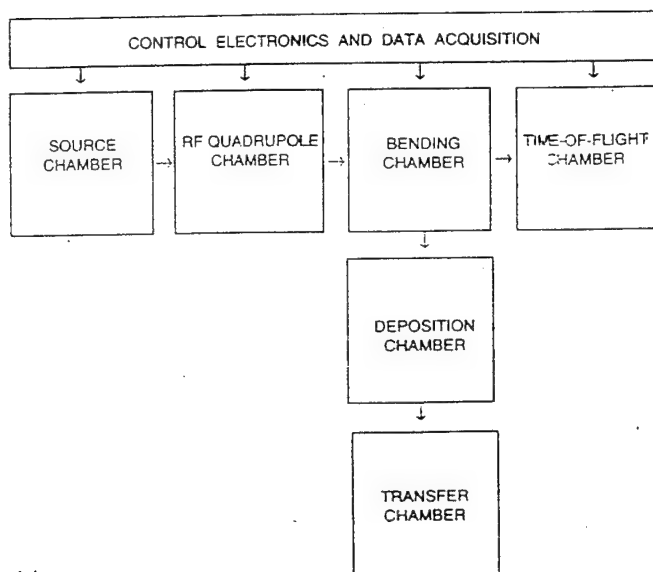
The early stages of the deposition process play a critical role in thin film growth using different deposition techniques.^{3,10} With this in mind, we have planned a series of

experiments that will study the role of clusters and the effect of their deposition energy on film formation. In this paper, we describe the design and performance of an apparatus that can be used to produce mass-selected, monoenergetic ionized clusters.

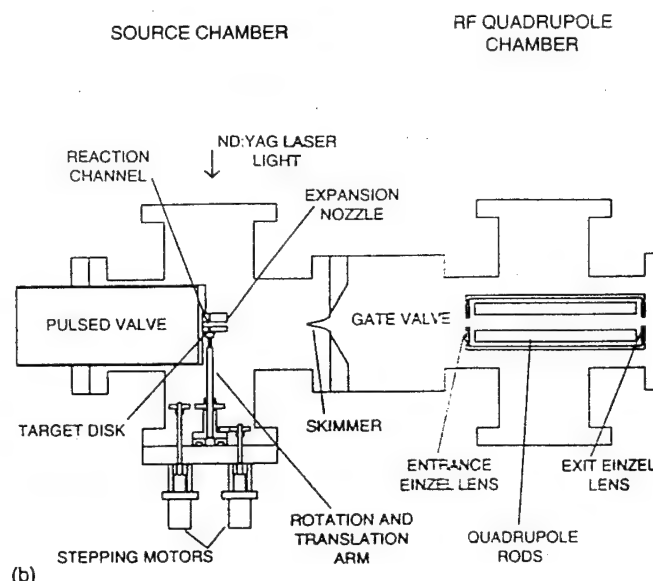
II. EXPERIMENT

Figure 1(a) shows the block diagram of the cluster generation apparatus developed for these experiments and Figs. 1(b)–1(d) provide details. The apparatus can be divided into parts according to function: (1) the source chamber where clusters are created; (2) the rf quadrupole chamber where the size of the cluster is selected; (3) the bending chamber where the neutral, positive, and negative clusters are separated from one another; (4) the time-of-flight chamber where the mass spectrum of the ICB is measured; (5) the deposition chamber where the clusters are deposited onto a substrate; (6) the transfer chamber used to transfer the sample to other systems for microscopic studies; and (7) the control electronics and data acquisition systems. Not depicted are the analytic systems used to examine the growth processes, including scanning tunneling microscopy, electron microscopy, x-ray photoemission, and synchrotron radiation photoemission.

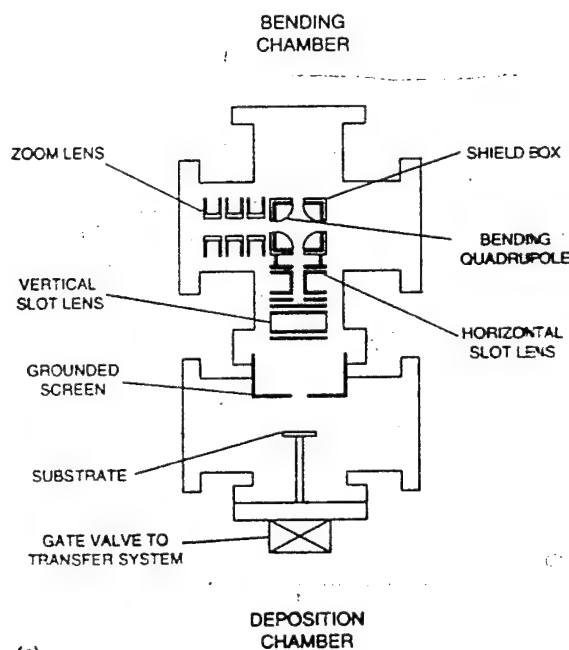
The vacuum portion of the apparatus consists of four six-way 6 in. crosses that house the cluster source, the rf quadrupole, the bending quadrupole, and time-of-flight systems; one five-way 6 in. cross that houses the deposition target; and one six-way 2.75 in. cross with a magnetic manipulator that serves as the transfer system. Differential pumping of He is used to optimize the pressure throughout the system during operation. The source chamber is pumped by a 450 l s^{-1} two-stage pump that incorporates turbomolecular and molecular drag operation. The rf quadrupole and bending chambers are pumped by conventional turbomolecular pumps (170 and 330 l s^{-1} , respectively). The time-of-flight chamber is pumped by a 150 l s^{-1} differential ion



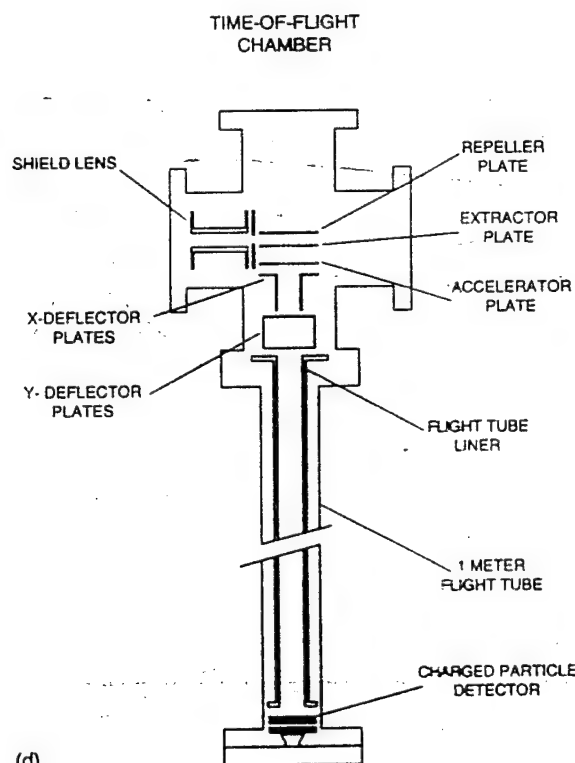
(a)



(b)



(c)



(d)

FIG. 1. (a) A schematic of the cluster source consisting of the source chamber, the rf quadrupole chamber, the bending chamber, the TOF chamber, the deposition chamber, the transfer chamber, and the data acquisition and control electronics. A detailed drawing of the source and rf quadrupole chambers is shown in (b). The bending chamber and deposition chamber details are shown in (c). The TOF chamber is shown in (d).

pump. The portable transfer system uses a $150 / \text{s}^{-1}$ differential ion pump with additional pumping supplied by titanium sublimation. Gate valves isolate the source chamber and the transfer systems from the other components.

A. Source chamber

The source chamber is based on the system developed by Maruyama, Anderson, and Smalley.¹¹ The design has been modified to increase the operational reliability and the cluster flux so as to enable the growth of thin films. The main components, shown in Fig. 1(b), are the pulsed valve (R. M. Jordan Co.), the nozzle block, the target motion control sys-

tem, and a skimmer (Beam Dynamics). The nozzle block consists of the reaction channel and the expansion nozzle. Target motion is accomplished via stepping motors and two rotary feedthroughs. The target manipulator contains the target disk, the rotation arm, and a translation stage.

The target disk must be moved after each laser pulse to prevent the laser from drilling holes or grooves, an effect that decreases the flux. Controlled disk irradiation comes from rotation and translation that is accomplished via two computer-controlled stepping motors. Translation is controlled by a rack-and-pinion system. A stepping motor turns a

64 pitch gear against a rack that is mounted to the translational stage through a bellows-sealed rotational motion feedthrough. The stage slides along two linear bearings and holds a rotating shaft. The target is mounted to the opposite end of this shaft. Rotation is accomplished via a belt-driven mechanism. A second stepping motor turns a pulley through another rotational feedthrough. This pulley drives another that is mounted to the target shaft via a Viton belt. The belt needs to stretch slightly, because the distance between the pulleys changes during stage translation.

The cluster generation process begins when a pulse from a Nd:YAG laser (Continuum model YG661, 532 nm, 30–50 mJ) is focused to a 0.8-mm-diam spot on the target disk. The interaction of the laser pulse with the target forms a plasma that expands into the reaction channel. These atoms collide with one another to form energized complexes that are then stabilized by collision with a third body. A buffer gas of He enhances the rate of stable cluster formation since there are too few vaporized atoms to stabilize more than a small fraction of the complexes. The distance from the target disk to the nozzle block is kept small (0.35 mm) to maximize the solid angle subtended by the entrance to the reaction channel. This optimizes the collection of vaporized atoms. Friction between the target disk and the nozzle block is minimized by placing a Teflon ring around the target disk. We place a 0.1 mm stainless steel ring between the Teflon ring and the target holder, after sanding the ring and target disk flush, to ensure that the target-to-block spacing and orientation are consistent and reproducible. Experiments show that a high cluster yield is obtained only if the Teflon ring forms a tight seal with the nozzle block. Therefore, the target holder must be pushed against the nozzle block evenly. In practice, this is achieved by using a universal joint from the target holder and shaft. The universal joint accommodates any misalignment and it facilitates target replacement.

Care was taken to keep the He free of oxygen-bearing species since many target materials readily form stable oxides. We use research purity He gas (99.9999% pure) that is passed through a molecular sieve trap (3A) cooled by liquid nitrogen and through a lithium-bearing getter trap (Supelco model OMI-1). All tubing used for the gas manifold is chromatography grade.

The pulsed valve operates at 10 Hz and injects approximately 1.6×10^{-2} Torr of He per pulse into the reaction channel (full width at half-maximum $\sim 40 \mu\text{s}$) prior to the laser pulse. The He gas backpressure in the valve is ~ 10 atm and, since the entrance to the reaction channel is small, the gas experiences a supersonic expansion along the main axis of the reaction channel. Collisions with the gas bend the plasma toward the exit. Without these collisions, most of the vaporized atoms would be deposited on the walls of the reaction channel. The He gas pressure controls the plasma expansion rate into the reaction channel. This determines the number density of target atoms and the temperature in the reaction channel. These factors determine the cluster growth rate. The ability to control the cluster size distribution by suitably selecting the time of vaporization is one of the most important features of this type of source. The He gas and

clusters exit the reaction channel through a 10° expansion nozzle.

A high He pressure at the skimmer can disperse the beam.¹² The nozzle angle or the distance to the skimmer, Fig. 1(b), must be large enough to avoid this problem. The clusters must have a sufficient number of collisions with the He gas during adiabatic expansion to reach the He gas velocity. Hence, the angle cannot be too large nor the cone too short. It is desirable for the clusters and He to travel at the same velocity. The 4 mm orifice skimmer collimates the beam, contains most of the carrier gas in the source chamber, and prevents shock waves from dispersing the beam.

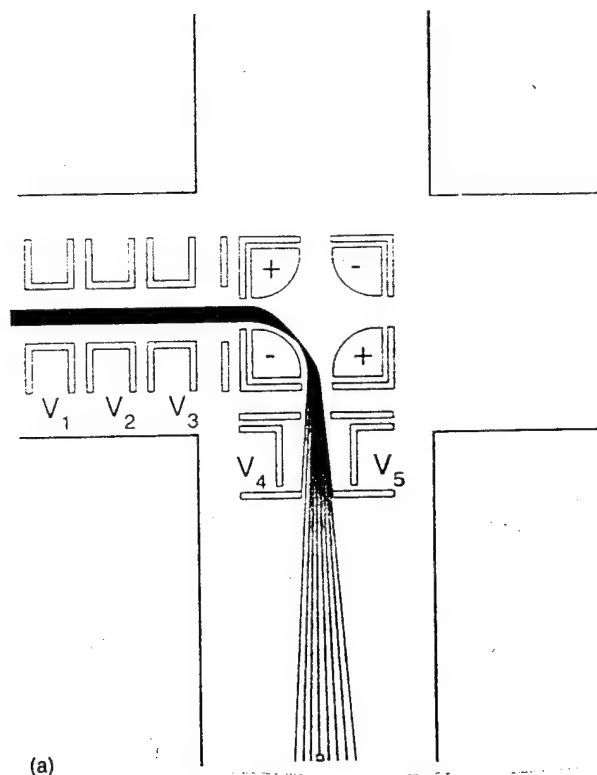
B. rf quadrupole chamber

The quadrupole chamber contains the rf quadrupole and the appropriate entrance and exit einzel lenses, as shown in Fig. 1(b). When in operation, ions with a specific charge-to-mass ratio are passed along the quadrupole axis. Our quadrupole has a mass range of 4000 amu and a resolution of 1.2 amu for singly charged species (Extrel Corporation model 7-162-8). It has a 350 W power supply that provides the dc and 880 kHz ac voltages. The electrostatic lenses focus and minimize dispersion of the cluster beam. An additional einzel lens can be mounted to the front of the quadrupole to further minimize the dispersion in the ionized beam.

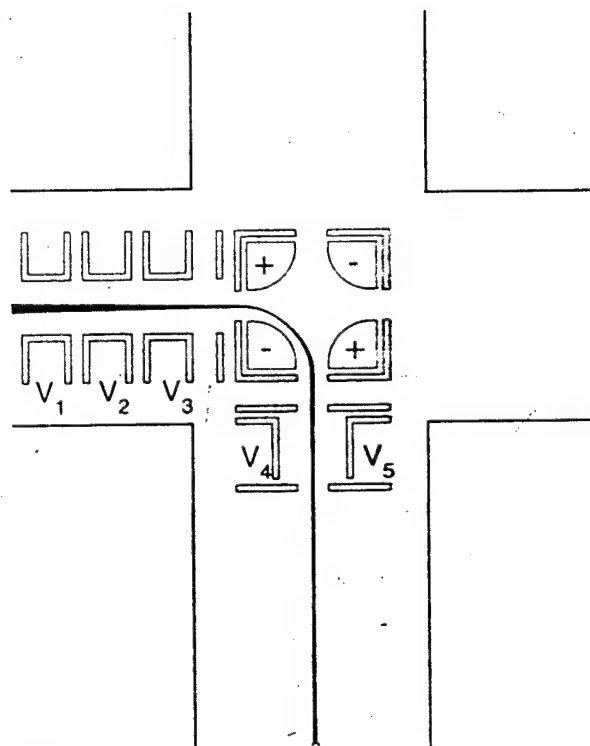
C. Bending chamber

Clusters that leave the quadrupole chamber enter the bending chamber shown in Fig. 1(c). The main elements of this chamber are the zoom lens, the electrostatic bending quadrupole, and the horizontal and vertical slot lenses. The bending quadrupole consists of a grounded box that contains four quarter-round electrodes that are perpendicular to the main beam. Zeeman¹³ showed that a hyperbolic field bends ions through 90° without dispersion. We can approximate hyperbolic fields using round electrodes if the rod radius, r , and the distance from the center of the quadrupole to the nearest point of any rod, r_0 , satisfy the relation¹⁴ $r = 1.15r_0$. Trajectory calculations indicate that end effects are minimized if the length of the rods is at least five times the rod separation. Since the bending quadrupole and the grounded shield box must fit inside the vacuum chamber, we have built a bending quadrupole that is 6.22 cm square and 7.00 cm tall. The rods are 1.97 cm in radius, 6.86 cm long, and are separated by 1.27 cm.

Figure 2(a) shows a SIMION¹⁵ calculation of Si_2^+ trajectories through the quadrupole. The ions are assumed to have a kinetic energy of 3.78 eV that would be the kinetic energy of these clusters ions if the stagnation temperature of the He gas were 300 K and if the clusters were able to reach the terminal velocity of the He gas during the adiabatic expansion. The quadrupole rods marked with a (+) are held at 4.25 V and the (−) rods are at −4.25 V. The other elements, V_1 – V_5 and the vertical slot lens elements (not shown), remain at ground potential. The clusters are bent 90° , as expected, but entrance effects cause dispersion. To minimize



(a)



(b)

FIG. 2. SIMION calculations for 3.78 eV Si_4^+ ions traversing the bending quadrupole. The (+) and (-) rods are held at 4.25 and -4.25 V, while all other voltages are at ground potential in (a). The dispersion in the beam results from entrance effects. These effects are minimized by focusing the beam by applying voltages of -4, -2, and -4 V to V_1 , V_2 , and V_3 , respectively. The beam is centered on the substrate by applying -0.15 V to V_5 while holding V_4 at ground potential. These results can be seen in (b).

dispersion, we use a zoom lens to provide a focused beam that passes through the bending quadrupole at the geometric center of the electrodes.

The zoom lens consists of three consecutive cylindrical elements. It is typically operated with the end two elements at equal potentials and the central element at one-half of this potential. For example, a tightly focused beam that is slightly displaced from the axis of the system is achieved with voltages of -4, -2, -4 V for V_1 , V_2 , and V_3 while maintaining the slot lenses at ground potential. The deviation from the center line can be eliminated by applying an asymmetric potential to the horizontal slot lens. The overall beam profile is demonstrated in Fig. 2(b) where -0.15 V has been applied to V_5 while V_4 is still at ground potential. Applying an additional offset potential to the slot lenses leads to enhanced beam focusing.

The beam loses its original cylindrical symmetry while traversing the bending quadrupole and a separate set of lenses is used to focus it in the horizontal and vertical planes. The vertical slot lens (not shown in Fig. 2) operates in the same manner as the horizontal lens, but a symmetric potential is used. Finally, we note that the ionized clusters move through the bending chamber to the time-of-flight chamber if no voltages are applied to the bending quadrupole rods. In this case, the voltage applied to the zoom lens is adjusted to provide a longer focal length and optimize cluster fluence into the time-of-flight chamber.

To our knowledge, an electrostatic quadrupole has not been used to separate charged clusters from neutrals in cluster source instruments. Unlike pulsed techniques, the use of an electrostatic quadrupole allows the collection of the entire pulse for a given energy range. If all cluster sizes travel at the velocity of the He gas, then the quadrupole functions as a mass filter. Our design makes it possible to enhance the number of charged clusters by irradiating them with excimer laser light before they enter the quadrupole. This is important as the intensities of ionized clusters are small.

D. Time-of-flight chamber

The main elements of the time-of-flight (TOF) chamber, shown in Fig. 1(d), are the shield lens and the R. M. Jordan time-of-flight system. The TOF system contains an extraction stack, x- and y-deflector plates, a liner, and a charged particle detector. The extraction stack is a Wiley-McLaren¹⁶ pulsed stack composed of the repeller plate, the extractor plate, and the accelerator plate. The charged particle detector consists of three microchannel plates and a detector anode.

A high positive voltage pulse, used to select positive clusters, is applied to the plates when the beam emerges from the shield lens and is between the repeller and extractor plates. The voltage difference between these plates creates an electric field that is perpendicular to the original flight direction of the beam. Clusters are then deflected toward the accelerator plate, pass through it, and move toward the flight tube. Most of the initial velocity of the clusters perpendicular to the flight tube is negated by applying a voltage to deflector plates located between the accelerator plate and the liner. The clusters hit the charged particle detector system after traversing the flight tube.

A liner is used in the TOF system to increase the collection efficiency. The accelerator plate, the deflector plates, and the liner are held at high negative voltage for positive clusters. Figure 3(a) shows a SIMION calculation where the

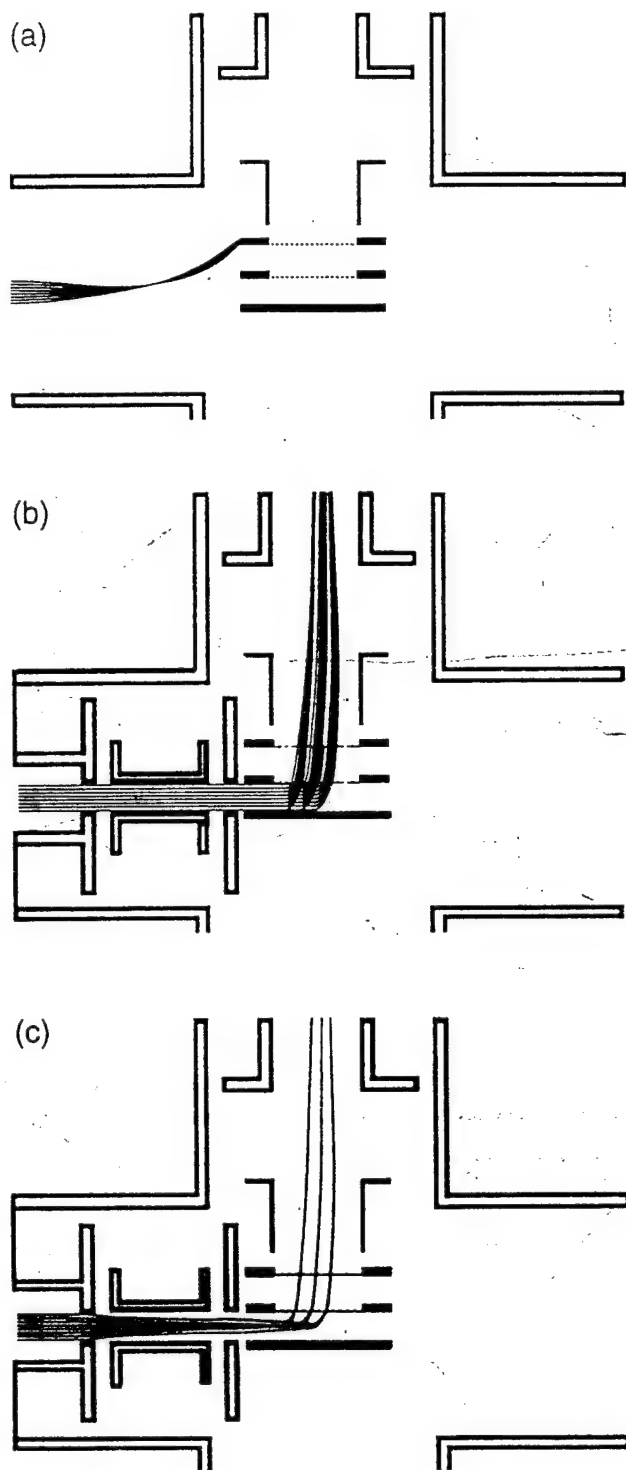


FIG. 3. SIMION calculation for 3.78 eV Si_n^+ clusters that enter the extraction stack of the TOF system. The repeller and extractor plates are pulsed from ground to 600 and 492 V, respectively. The accelerator, the left-hand deflection plate, and the liner are held at -500 V. The right-hand deflection plate is held at -380 V. In (a) the shield lens has been removed. In (b) the central element of the shield lens has been grounded. In (c) this element is held at -3 V. In (b) and (c) the three groups of trajectories denote the limits of the pulse that successfully traverse the flight tube to the charged particle detector.

large static electric field associated with these static potentials prevents the incoming Si_n^+ clusters from entering the extraction stack if no shield is used. The kinetic energy of the clusters is 3.78 eV in this example. The liner potential and that of one of the deflector plates is -500 V. The second deflector plate is held at -380 V. The repeller and the extraction plates are held at ground potential.

Ion beams are typically analyzed by inserting a floating shield tube in front of the extraction stack. This shield tube is kept at the same potential as the repeller plate. Figure 3(b) shows Si_n^+ cluster trajectories when a floating shield tube is used. The shield tube and the repeller are pulsed to 600 V potential and the extractor is pulsed to 492 V after the clusters enter the extraction stack. All other electrodes have the same value as in the previous case. Overall resolution is space resolution limited, as shown by the large acceptance region. Use of a small diameter skimmer improves the space resolution at the expense of signal intensity.

Better results are achieved with an einzel lens as shown in Fig. 3(c). The outer electrodes are grounded and the center electrode is held at -3 V. The other electrodes remain unchanged. The lens focuses the cluster beam. Our experiments show that the shield lens doubles both the resolution and the signal-to-noise ratio.

E. Deposition chamber

A mass selected cluster beam can be focused to a small spot on a substrate placed in the deposition chamber, Fig. 1(c). The deposition energy of the clusters can be controlled by biasing the substrate. We have placed a grounded screen with a small hole between the vertical slot lens and the substrate to prevent the cluster beam from spreading as a consequence of this bias voltage. Hence, the bias voltage does not influence cluster trajectories between the slot lenses and the screen.

The deposition process can be studied under a wide variety of conditions. The substrate can be cooled or heated for investigations that emphasize the effects of substrate temperature on film growth. It can also be exposed to reactive gases during deposition by using a doser located above the substrate that allows the study of, e.g., the growth of oxide and nitride films under conditions of energetic deposition.

F. Transfer chamber

The sample can be moved from the deposition chamber into the transfer chamber via a load-lock system situated beyond the deposition chamber. The load-lock system is pumped with a 145 l s^{-1} turbomolecular pump and a titanium sublimation pump. The pressure in the sample chamber is maintained with a 150 l s^{-1} differential ion pump.

G. Data acquisition and control electronics

Figure 4 shows a schematic of the data acquisition and control electronics for the cluster source. Depicted are all of the modules in the control hierarchy with arrows that represent the signal direction. An IBM PS/2 40 SX personal computer controls the entire experiment. The software source code was written using the graphics and menu creation utility.

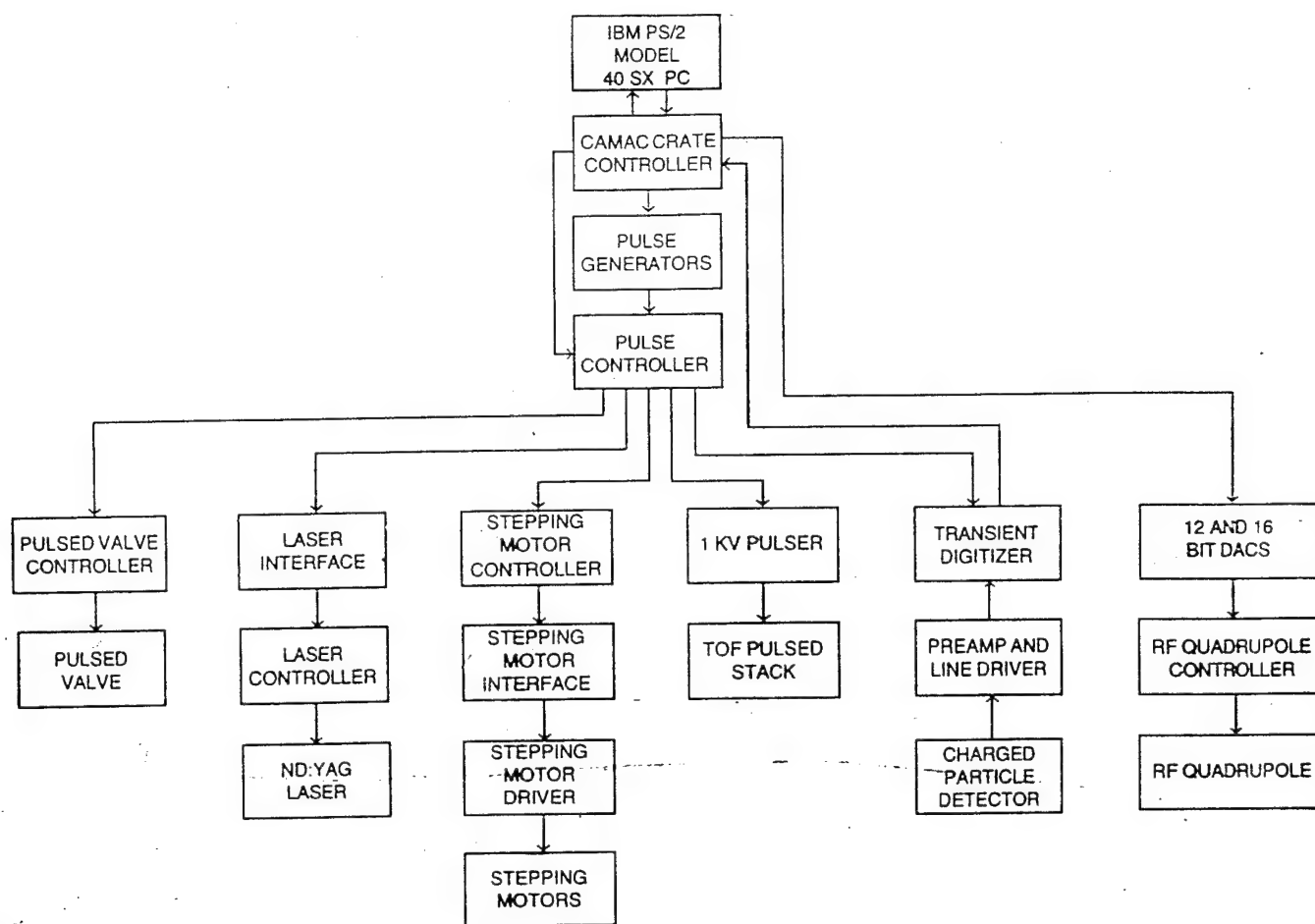


FIG. 4. Schematic diagram of the control electronics and data acquisition systems for the cluster source. A personal computer controls the experiment through a camac crate controller. Timing pulses come from two pulse generators whose output is fed to a pulse controller. The pulse controller sends a pulse through the pulsed valve controller and to the pulsed valve. It also controls the laser by sending another pulse through the laser interface and laser controller. The target disk moves when pulses are sent to the rotational and translational stepping motors through the stepping motor controller, the stepping motor interface, and the stepping motor driver. The rf quadrupole is operated by the quadrupole controller that is accessed through 2 DACs by the camac controller. The TOF system is pulsed by signals from the pulse controller, sent through the 1 kV pulser to the extraction stack. Data acquisition commences when a pulse from the pulse controller reaches the transient digitizer. The transient digitizer records the data from the charged particle detector that has passed through the pre-amp and line driver and sends it to the computer for display.

ties of the LabWindows system. The program accepts initial values provided by the operator and sends them to various parts of the apparatus. It allows for changes between the opening of the valve, the firing of the flash lamp, the triggering of the Q switch, and the pulsing of the extraction stack.

The computer communicates with the central components through a KineticSystems model 1502 camac crate with DSP Technology model 6002 controller. The control signals are loaded into two eight-channel pulse generators (KineticSystems model 3655) that send 200 ns pulses at the prescribed times. Since these pulses are too short to be used directly as trigger pulses by the other components, they are first sent to another camac module, the pulse controller, that increases their length to 70 μ s. Additionally, the computer can order the pulse controller to block any of the incoming signals.

Mechanically, the cluster generation process involves opening the pulsed valve, triggering the laser, and moving the target disk. Helium gas is injected into the cluster chamber when the pulse controller signals the pulsed valve controller to open the valve. A pulse is sent from the pulse con-

troller to the laser interface that increases the pulse height from TTL levels to 15 V. The larger pulse is then sent to the laser through the laser controller, firing the Q switch. A new portion of the target disk is exposed to the laser by rotating or translating the disk. The appropriate motor is activated by a pulse sent from the pulse controller through the stepping motor controller, the stepping motor interface, and stepping motor driver.

Once created, the clusters proceed out of the source chamber and into the rf quadrupole chamber. The rf quadrupole controller receives its commands from two 10 V digital-to-analog converters (DACs) that are, in turn, controlled by the computer through the camac controller. A 16-bit DAC (Joerger Enterprise model D/A-16) generates the mass command signal. All other potentials for the controller are provided by an 8-channel, 12-bit DAC (Jorway Corp. model 232).

A TOF mass spectrometer measures the cluster distribution. The pulse controller sends two signals to the 1 kV pulser. The first one pulses the stack to accelerate the ionized clusters toward the charged particle detector. The second sig-

nal resets the stack to its initial grounded state, allowing the next cluster pulse to enter. The pulse controller sends an additional signal to the transient digitizer that orders it to begin digitizing the signal coming from the charged particle detector through the preamp and line driver (Perry Amplifier models 481-50 and 491-50, respectively). The camac crate passes the digitized signal to the computer which stores and displays the data.

In addition to the active electrical components noted above, there are ten electrostatic lenses, not represented in Fig. 4, that minimize the beam dispersion as it travels from the source to either the TOF or the deposition chamber. Applying a potential to the bending quadrupole or leaving it grounded determines the destination of the clusters. If the clusters are to be deposited on the substrate in the growth chamber, then their final kinetic energy can be altered by biasing the substrate up to 5 kV.

III. DISCUSSION AND DESIGN CONSIDERATIONS

Cluster sources can operate in a continuous or a pulsed mode.^{11,17-20} Effusion and ion-sputter sources are examples of continuous sources. Laser vaporization and arc-discharge sources are examples of pulsed sources. The instantaneous fluence of a pulsed source is high but the overall fluence is lower than for a continuous source because of the duty cycle of the pulsed source. Continuous sources are limited in their control over the cluster distribution. Pulsed sources utilizing continuous gas flow operate at constant pressure and suffer this same limitation. The pulsed gas source gives greater control over the cluster distribution. This source can minimize the fluence disadvantage by shifting the cluster distribution mean toward the size of interest. As we are interested in studying film growth, it is useful to review the design and operational principles of a pulsed gas source in order to maximize the fluence.

The intensity of the laser determines how much material is vaporized from the target disk. Thus, increasing laser intensity will increase fluence. However, a point is reached where further increase in laser power causes little or no change in fluence. The amount of incident laser power at the surface of the target disk will be reduced due to absorption or reflection by the plasma. The rate of vaporization of the material from the surface will also be limited by flow conditions in the reaction channel.²¹

To reach the vaporization point, heat must be supplied faster than it can be removed. The laser power and spot size determine the heat transfer rate to the surface while the thermal and optical properties of the material determine the heat transfer rate from the surface. A differential heat balance that takes into account conductive, evaporative, and radiative losses can be used to estimate the surface temperature. The pressure at the surface can be determined from the Clausius-Clapeyron relation and vapor pressure data.²² This model predicts a surface temperature of 6500 K, assuming evaporative losses are negligible compared to the incident laser power ($\sim 10^8$ W cm⁻²) during the 7 ns laser pulse.

The mass transfer rate can be estimated for a given surface temperature from gas dynamics.^{21,23} For vapor pressures larger than ambient pressure, translational equilibrium does

TABLE I. Si flux from target disk as a function of surface temperature and cluster chamber source pressure.

Surface temperature (K)	Fluence, Si atoms s ⁻¹	
	11 Torr	110 Torr
3000	4.0×10^{18}	1.3×10^{18}
3500	5.7×10^{19}	3.4×10^{19}
4000	2.9×10^{20}	2.7×10^{20}
5000	2.8×10^{21}	2.8×10^{21}
6000	1.2×10^{22}	1.2×10^{22}
7000	3.6×10^{22}	3.7×10^{22}

not exist at the interface. However, collisions between particles will establish translational equilibrium within a few mean free paths. The resulting nonequilibrium region is called the Knudsen layer. The pressure and temperature at the Knudsen layer can be related to the pressure and temperature at the surface from mass, momentum, and energy conservation. It can be shown²⁴ that these nonequilibrium processes cannot drive the velocity beyond the sonic velocity at the Knudsen layer. Thus, the maximum flux across the Knudsen layer can be determined by using the equation of state and the continuity relations.

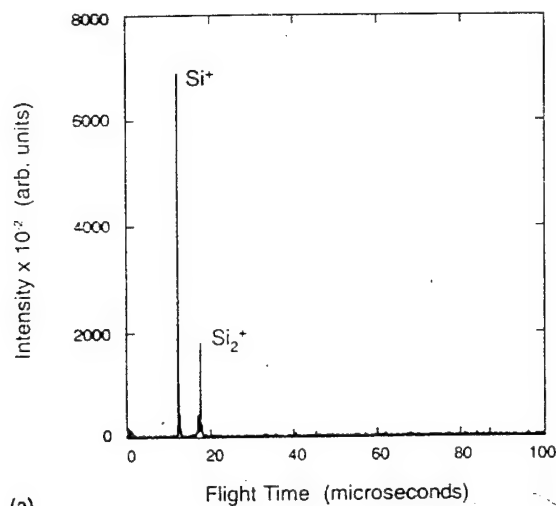
Table I gives the calculated Si flux into He as a function of target disk temperature and He pressure. These parameters are determined by the stagnation pressure and temperature of the He and by the reaction channel geometry. The pulsed valve typically operates at 10 atm and 300 K, giving a He pressure of 11 Torr and a temperature of 23 K above the target disk. The maximum Si flux is 2×10^{22} at cm⁻² s⁻¹ for a surface temperature of 6500 K. This corresponds to a maximum heat loss of 1.5×10^{-4} W cm⁻². This is insignificant compared to the incident laser intensity, validating the assumption above.

The velocity at the expansion nozzle exit can be used to verify independently the surface temperature. The velocity can be directly related to the temperature at the edge of the Knudsen layer by assuming steady-state isentropic flow, and using mass, momentum, and energy conservation and the equation of state. If the laser fires before the pulsed valve opens, no collider gas is present to cool the plasma. Velocities corresponding to a temperature of 4100 K at the edge of the Knudsen layer and a surface temperature of 6100 K were determined. Increasing the laser power from 40 to 70 mJ per pulse had no effect on arrival time or measured intensity.

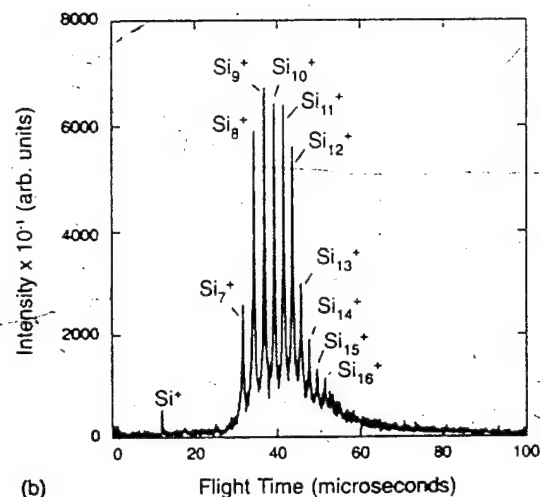
The condensation reactions that comprise clustering are described by the Lindeman mechanism.²⁵ The rate for the reaction, $A_n + A \rightarrow A_{n+1}$, is given by

$$R = \frac{k_s k_f [He]}{k_d + k_s [He]} [A_n] [A],$$

where R is the reaction rate, k_s is the stabilization rate constant, k_f is the rate constant for activated complex formation, k_d is the rate constant for dissociation, and brackets denote concentration. Accordingly, an increase in the pressure in the reaction channel will increase the rate of cluster formation and will shift the product distribution toward larger sizes. We



(a)



(b)

FIG. 5. TOF spectra of ionized Si clusters produced when the laser Q switch is (a) triggered at the leading edge of the gas pulse and (b) the laser firing time has been delayed 4 μs . Small delay times give lower He partial pressures than large delay times and this results in significant dissociation of small clusters. Higher partial pressures lead to stabilization due to an increased number of collisions.

can vary the pressure in the reaction channel by changing the delay time between the opening of the valve and the triggering of the Q switch.

Figures 5(a) and 5(b) illustrate the effect of gas pressure on the cluster distribution. In Fig. 5(a), the Q switch fires on the leading edge of the gas pulse, 2 μs after the valve opens. In Fig. 5(b), the laser firing time has been delayed by 4 μs . Thus, we are able to optimize the cluster size distribution by changing the reaction conditions, thereby decreasing deposition time. Comparison of Figs. 5(a) and 5(b) also shows that the fluence of a given ionized cluster decreases as the size distribution broadens. The intensity of the smaller clusters in Fig. 5(b) is decreased due to the effect of the electrostatic lens system. SIMION calculations show that Si^+ will arrive at the extraction stack approximately 40 μs before Si_{10}^+ for the conditions used. Since the evaporative cooling rate gives pulse widths on the order of 30–40 μs , we should not expect to see any significant intensity for the lightest clusters.

A significant decrease in cluster flux occurs during su-

personic expansion in the expansion nozzle. The cluster fluence at the skimmer in a supersonic beam, w_s , can be described as

$$w_s = \frac{1}{2} \gamma M^2 \frac{A_s}{\pi z_s^2} w_0,$$

where γ is the ratio of the heat capacities at constant pressure to constant volume, M is the Mach number at the expansion nozzle orifice, A_s is the skimmer orifice area, z_s is the separation between the nozzle and the skimmer, and w_0 is the cluster fluence at the nozzle.²⁶ This equation indicates that Si atoms will enter the rf quadrupole chamber at a maximum rate of $\sim 10^{14} \text{ s}^{-1}$ for a skimmer with a 4 mm diam located 10.8 cm from the plasma injection point, an exit Mach number of 4 and a duty cycle of 0.0004. This value is achieved by assuming that the laser and pulsed valve are operated at 10 Hz and that the evaporation occurs over a period of 40 μs . Since mass selection is accomplished by electrostatic methods, the number of clusters available for selection corresponds to the number of ionized clusters leaving the growth chamber. The percentage of atoms ionized depends on the type of source. For example, about 5%–15% of transition metal clusters are charged in arc discharge sources,²⁰ while up to 80% of metal clusters are charged in gas discharge sputtering sources.²⁷ Ion yields in laser desorption mass spectrometry suggest that about 0.1% of Si is positively charged under our operating conditions.²⁸ Thus, we would expect that the maximum fluence of ionized Si would be approximately $2 \times 10^{11} \text{ s}^{-1}$. The average fluence of ionized Si would be about $5 \times 10^9 \text{ s}^{-1}$, assuming that the evaporative cooling cycle spans temperatures from the maximum surface temperature to the boiling point at the reaction channel pressure. This fluence corresponds to 800 pA, a value that compares favorably to Faraday cup measurements of 125 pA made in the bending chamber. Space charge effects can explain the difference in observed and estimated Si^+ fluence.

Although the observed ion fluence is small, the instantaneous value is large because of the short pulse duration. Space charge effects produce radial dispersion in the beam that can be calculated from²⁹

$$\frac{d^2 r}{dt^2} = 1.73 \times 10^{24} \left(\frac{I}{mrv} \right),$$

where r is the beam radius in cm, t is time in s, I is the instantaneous current in amps, m is the mass in amu, and v is the beam velocity in cm s^{-1} . The dispersion expected from purely hydrodynamic considerations gives a beam radius of 3.65 cm at the skimmer. Figure 6 shows that space charge effects are important for small clusters, while they can be neglected for large heavy clusters. A comparison between the hydrodynamic and space charge broadening of the beam results in a 16-fold decrease in fluence for the atomic species. Figure 6 also shows that for larger clusters this effect is small relative to the hydrodynamic effects.

Mass selection will further reduce the cluster fluence available for deposition. Figure 5(b) shows that the yield of Si_{12}^+ is less than 10% of the ionized clusters. Assuming no losses, this corresponds to a fluence of about 60 pA. Figure 7 shows that the Si_{12}^+ signal intensity decreases by an order of

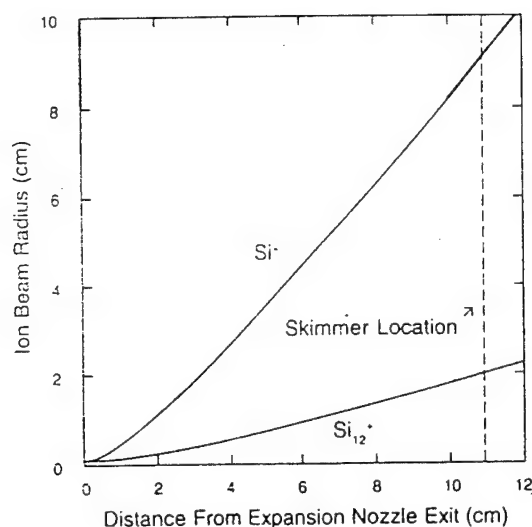


FIG. 6. Space charge calculations of the cluster beam radius as a function of cluster mass and distance from the expansion nozzle throat. An ion current of 10^{-8} A and a beam velocity of 1.8×10^5 cm s $^{-1}$ were used. At the skimmer, radial dispersion due to space charge effects is significant for Si ions compared to the hydrodynamic beam radius (~ 3.65 cm). Space charge effects are negligible for Si $_{12}^+$.

magnitude when using the rf quadrupole as a result of dispersion, giving at best, $\sim 2\text{--}5 \times 10^7$ clusters of Si $_{12}^+$ per second. This value compares favorably with results of Kuk *et al.*⁷ that were obtained in a continuous gas flow source using a laser operating at 200 Hz. We can deposit 10^{14} Si $_{12}^+$ clusters cm $^{-2}$ in 10 h assuming a deposition spot size of 1 mm 2 .

In summary, we have the ability to prepare thin films of mass selected clusters sufficiently fast to avoid surface contamination problems. This gives us the capability to study nucleation and the initial growth of films produced from clusters. However, to grow thick films we need to deposit a

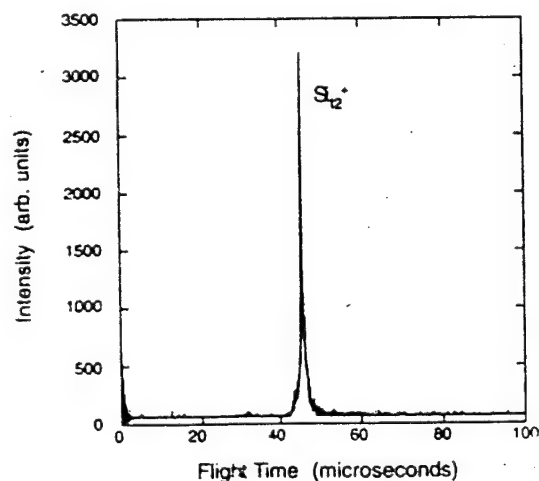


FIG. 7. TOF spectrum of cluster beam shown in Fig. 4(b) after mass selection by the rf quadrupole. The lower intensity is due to exit dispersion produced by sinusoidal trajectories within the rf quadrupole.

range of cluster sizes or alter the source to increase the fluence. For instance, the vaporization laser repetition rate can be increased and/or an excimer laser can be used to photo-ionize neutral clusters.

ACKNOWLEDGMENTS

This work was supported by the Army Research Office under Grant No. DAAL03-92-G-0216. The authors thank R. E. Smalley for useful discussions and design specifications for the cluster source, L. D. Schmidt for the use of his Nd:YAG laser, Beam Dynamics for donating the skimmers used in our system, and J. M. Alford for helpful discussions.

- ¹ See, for example, *Ion Beam Assisted Film Growth*, edited by T. Itoh (Elsevier, Amsterdam, 1989).
- ² T. Takagi, I. Yamada, M. Kunori, and S. Kobiyama, in *Proceedings of the 2nd International Conference on Ion Sources* (Österreichische Studiengesellschaft für Atomenergie, Vienna, 1972).
- ³ I. Yamada, G. H. Takaka, H. Usui, S. K. Koh, F. Sato, and T. Yamada, in *Proceedings of the 14th Symposium on Ion Sources and Ion-Assisted Technol.*, Tokyo, 1991, edited by T. Takagi (unpublished).
- ⁴ I. Yamada, in *Proceedings of the 13th Symposium on Ion Sources and Ion-Assisted Technol.*, Tokyo, 1990, edited by T. Takagi (unpublished).
- ⁵ W. L. Brown, M. F. Jarrold, R. L. McEachern, M. Sosnowski, G. Takaka, H. Usui, and I. Yamada, *Nucl. Instrum. Methods B* 59/60, 182 (1991).
- ⁶ R. L. McEachern, W. L. Brown, M. F. Jarrold, M. Sosnowski, G. Takaka, H. Usui, and I. Yamada, *J. Vac. Sci. Technol. A* 9, 3105 (1991).
- ⁷ Y. Kuk, M. F. Jarrold, P. J. Silverman, J. E. Bower, and W. L. Brown, *Phys. Rev. B* 39, 11 168 (1989).
- ⁸ W. Eberhardt, P. Fayet, D. M. Cox, Z. Fu, A. Kaldor, R. Sherwood, and D. Sondericker, *Phys. Rev. Lett.* 64, 780 (1990).
- ⁹ D. M. Cox, B. Kessler, P. Fayet, W. Eberhardt, Z. Fu, D. Sondericker, R. Sherwood, and A. Kaldor, *Nanostruct. Mater.* 1, 161 (1992).
- ¹⁰ I. Yamada, *Nucl. Instrum. Methods B* 37/38, 770 (1989).
- ¹¹ S. Maruyama, L. R. Anderson, and R. E. Smalley, *Rev. Sci. Instrum.* 61, 3686 (1990).
- ¹² J. B. Anderson, in *Molecular Beams and Low Density Gas Dynamics*, edited by P. P. Wegener (Dekker, New York, 1974), Chap. 1.
- ¹³ H. D. Zeeman, *Rev. Sci. Instrum.* 48, 1079 (1977).
- ¹⁴ D. R. Denison, *J. Vac. Sci. Technol.* 8, 266 (1971); A. P. Bandford, *The Transport of Charged Particle Beams* (Spon, London, 1966).
- ¹⁵ D. A. Dahl and J. E. Delmore, SIMION PC/PS2 User's Manual Version 4.0, Idaho National Engineering Lab, EG&G Idaho Inc., P.O. Box 1625, Idaho Falls, ID 83415.
- ¹⁶ W. C. Wiley and I. H. McLaren, *Rev. Sci. Instrum.* 26, 1150 (1955).
- ¹⁷ B. G. De Boer and G. D. Stein, *Surf. Sci.* 106, 84 (1981).
- ¹⁸ W. Begemann, K. H. Meiwes-Broer, and H. O. Lutz, *Phys. Rev. Lett.* 56, 2248 (1986).
- ¹⁹ E. K. Parks, B. H. Weiler, P. S. Bechtold, W. F. Hoffman, G. C. Nieman, L. G. Lobs, and S. J. Riley, *J. Chem. Phys.* 88, 1622 (1988).
- ²⁰ H. R. Sickmann, Ch. Lüder, J. Fachmann, H. O. Lutz, and K. H. Meiwes-Froer, *Z. Phys. D* 20, 417 (1991).
- ²¹ C. J. Knight, *AIAA J.* 17, 159 (1979).
- ²² *JANAF Thermochemical Tables*, 3rd ed. (National Bureau of Standards, Washington, DC, 1986).
- ²³ S. Anisimov, *Sov. Phys. JETP* 27, 182 (1968).
- ²⁴ C. J. Knight, *J. Fluid Mech.* 75, 469 (1976).
- ²⁵ P. J. Robinson and K. A. Holbrook, *Unimolecular Reactions* (Wiley-Interscience, London, 1972).
- ²⁶ J. B. Anderson, R. P. Andres, and J. B. Fenn, *Adv. Chem. Phys.* 10, 275 (1966).
- ²⁷ H. Haberland, M. Kraits, and M. Mall, *Z. Phys. D* 20, 413 (1991).
- ²⁸ H. E. Duckworth, R. C. Barber, and V. S. Venkatasubramanian, *Mass Spectroscopy*, 2nd ed. (Cambridge University Press, Cambridge, 1990).
- ²⁹ R. Hutter, in *Focusing of Charged Particles*, edited by A. Septier (Academic, New York, 1967), Vol. II.

Appendix 2

Reprint of "Interaction of 300-5000 eV Ions with GaAs(110)"

X.S. Wang, R.J. Pechman, and J.H. Weaver

Published in Appl. Phys. Lett. **65**, 2818-2820 (1994).

Interaction of 300–5000 eV ions with GaAs(110)

X.-S. Wang, R. J. Pechman, and J. H. Weaver

Department of Materials Science and Chemical Engineering, University of Minnesota, Minneapolis, Minnesota 55455

(Received 11 July 1994; accepted for publication 26 September 1994)

The interaction of 0.3–5 keV Ar^+ and Xe^+ ions with GaAs(110) in the initial stages of sputtering was studied with scanning tunneling microscopy. At normal incidence, these ions create pits typically of 1–5 unit cells and, on average, each ion leads to the removal of about 1.5 surface atoms from the surface. The sputtering yield depends weakly on ion mass and energy. The bombardment events are mainly in the single knock-on regime, with some in the linear cascade regime. The mechanism of ion-surface impact is discussed. © 1994 American Institute of Physics.

The interaction of energetic ions with crystal surfaces holds current and historic scientific interest with many important technical implications.¹ Apart from channeling where ions travel in open columns, ion-crystal interactions can be classified into three regimes.^{1,2} For low ion energy and/or ion mass, the collisions take place with a few atoms by displacing them from their original sites, some of which are ejected from the surface, but they do not displace other atoms. Such a collision process is said to be in the single knock-on regime. With increasing energy (a few keV) and mass (e.g., Ar), the ions collide with more target atoms and transfer sufficient energy to knock a few other atoms off their lattice positions, forming a linear cascade event. At even higher energy, a massive ion initiates a large number of cascade collisions so that all atoms in a volume are in motion, with a high density of vibrational and electronic excitations induced. This situation is called collision in the spike regime, and the high density of excited states is often described as local melting.³ The defect structures created in these three regimes must be quite different.

Although these ion-surface interaction scenarios have long been accepted, experimental evidence of them has been rare⁴ due to the lack of a proper probe for characterizing damage by an individual ion. Direct observations of the defect structures induced by ions with energy on the order of 10^2 – 10^3 eV were made only recently using scanning tunneling microscopy (STM).^{5–8} STM has also been used to accurately measure the sputtering yield of a single crystal.^{5,9} These pioneering investigations notwithstanding, there are very few direct experimental results to substantiate the basic propositions and to assess the effects of ion energy, mass, sample orientation, and other physical properties on the bombardment process. Such direct assessments are important for the accurate description of the ion bombardment process and for the application of ion beams in nanostructure fabrication.

Here, we report results of systematic STM investigations of medium energy ion bombardment of GaAs(110) at normal incidence. In particular, we examined variations of the single-collision damage structure and the sputtering yield (the number of atoms ejected from the sample per impinging ion) with respect to the ion energy (300–5000 eV) and mass ($^{40}\text{Ar}^+$ and $^{131}\text{Xe}^+$). Our results show that craters of mainly 1–5 unit cells are generated and that the atoms from the craters are either ejected from the surface or displaced onto

the surface as adatoms. The average crater size increases moderately with ion energy while the sputtering yield is basically unchanged. Furthermore, the observed differences between Ar^+ and Xe^+ bombardments are not significant. These results will be compared with those for other samples and with theoretical studies,^{5,8,10,11} and their implications on the fundamental theory of ion bombardment will be discussed. We have also investigated the effects of ion incident geometry and the evolution of surface morphology.¹²

The experiments were performed in an ultrahigh vacuum chamber (base pressure 2×10^{-10} Torr) with surface analysis capabilities of STM and low-energy electron diffraction. Well-ordered GaAs(110) surfaces were prepared by *in situ* cleaving of *p*-type ($\sim 2 \times 10^{18} \text{ cm}^{-3}$ Zn-doped) single crystals. The density of vacancies on the cleaved surface was below $5 \times 10^{11} \text{ cm}^{-2}$. The differentially pumped ion gun was thoroughly degassed before every bombardment experiment and the chamber pressure did not exceed the 10^{-9} -Torr range during ion bombardment. The surfaces were exposed to ions generated with high purity Ar or Xe gas. Ion flux was determined by measuring the current from the sample to ground. Typical values were in the range of 5×10^{10} to $5 \times 10^{11} \text{ cm}^{-2} \text{ s}^{-1}$, with which the heating effect by the beam was negligible. The surface temperature was raised to 675–775 K by a hot filament during bombardment for sputtering yield measurement. The temperature was monitored with an optical pyrometer and a thermocouple to an accuracy of ± 20 K. STM images were taken in constant current mode at room temperature, normally with a negative sample bias of 2–3 V and a tunneling current 0.05 to 0.5 nA. Positive bias and dual-bias images were taken occasionally.

Figure 1 displays representative images for surfaces bombarded at normal incidence with Ar and Xe ions of different energies. By exposing a well-ordered surface to a low fluence (10^{12} to 10^{13} cm^{-2}) of bombarding ions, we were able to observe defects created by individual impacts. As shown in Figs. 1(a) and 1(b), individual defects created by 300-eV and 3-keV Ar^+ ions at normal incidence appear similar. Since the appearance of a point defect in an STM image depends on its charging state, dopant type, imaging polarity, and the tip condition,¹³ it is difficult to identify all details of a defect. Nevertheless, more than 90% of the defect sites showed both missing As and Ga atoms in dual-bias images, indicating removal of roughly equal numbers of As and Ga

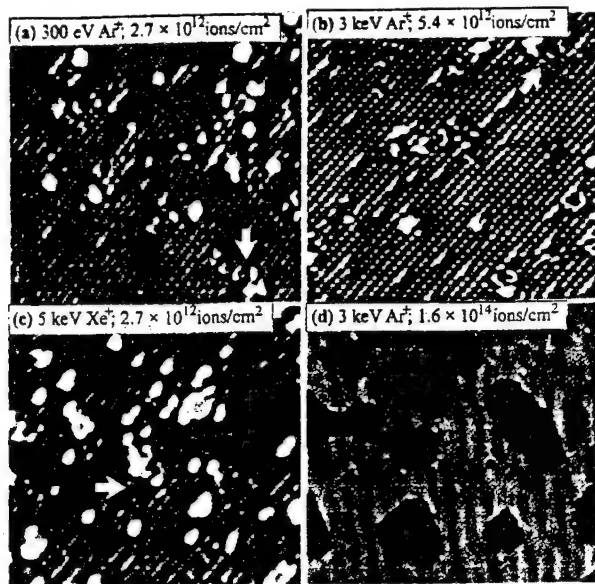


FIG. 1. Filled-state STM images of GaAs(110) after Ar^+ or Xe^+ bombardment. (a)–(c) are areas of $200 \text{ \AA} \times 200 \text{ \AA}$ after exposure to low ion fluences at 300 K. Defects are typically 1–5 unit cells in size but the arrows point to larger defects. (d) shows a $500 \text{ \AA} \times 500 \text{ \AA}$ area that was sputtered at 725 K for yield measurements. Dark regions are single-layer deep vacancy islands. In all images, [001] is from upper left to lower right with [110] pointing from upper right to lower left.

atoms. This is in contrast to preferential sputtering of As that has been reported¹⁴ after removal of hundreds of monolayers of material with beams with intensities $\sim 10^2$ times higher than those used here. Such conditions differ markedly from ours in that a high fluence at room temperature can produce surface species and bonding configurations that are far from those of ideal GaAs, including formation of volatile species like As_2 or As_4 . Desorption of such species during a subsequent energetic impact is likely, producing Ga enrichment because the equivalent Ga_x species have very different desorption characteristics. Most of the defects in Figs. 1(a) and 1(b) are voids of 1–5 unit cells. A few features 6–20 unit cells in size, consisting of missing atoms and lattice disorder, can also be observed, as those marked with arrows. The depth of some pits may be more than one atomic layer, but the STM tip can only reach a limited depth, especially for small pits. The defect densities on these samples are $4 \times 10^{12} \text{ cm}^{-2}$ for (a) and $9 \times 10^{12} \text{ cm}^{-2}$ for (b), roughly proportional to the ion fluence. The average pit size increased from 2.1 unit cells for 300-eV Ar^+ to 3.1 for 3-keV Ar^+ , a relatively small change compared with that of ion energy. The bright protrusions that appear on both surfaces are adatoms ejected during sputtering. They are more likely to be found near the larger defects. Adatom-vacancy recombination is observed upon annealing above 675 K. Finally, we searched for isolated point defects that might be created just beneath the surface, such as interstitials and vacancies. Due to their effect on local electronic states, these defects should be distinguishable when they are in the second or third layer.¹⁵ Their absence on bombarded surfaces indicates that, if they are generated, they are either so close to the pits or they are too deep.

Replacing Ar^+ with Xe^+ increases the momentum by a factor of 1.8 for the same energy. Moreover, the interaction cross section of a Xe^+ was expected to be larger than Ar^+ (ionic radius is 1.54 \AA for Ar^+ and 1.91 \AA for Xe^+). However, the average pit size created by normal incident 3-keV Xe^+ bombardment is 3.0 unit cells, which is basically the same as that of 3-keV Ar^+ . STM images for this surface were equivalent to Fig. 1(b). An increase in the Xe ion energy to 5 keV produced the surface displayed in Fig. 1(c). Analysis shows that the average pit size was increased to 3.8 unit cells. The extent of damage normal to the surface is again not accessible to STM. As far as lateral damage is concerned, we conclude that the effect of ion energy increases but remains moderate.

To measure sputtering yield, we bombarded the sample at 675–775 K. In this temperature range, adatom diffusion and adatom-vacancy annihilation processes occur, and vacancy migration and coalescence become apparent. Evaporation of GaAs is negligible in this temperature range although surface degradation due to As evaporation was observed above 775 K. The sputtering yield is determined by measuring the area of vacancy islands.^{5,9} For example, single-layer-deep vacancy islands cover about 23% of the surface shown in Fig. 1(d). This sample was sputtered by 3-keV Ar^+ with a fluence of $1.6 \times 10^{14} \text{ ions cm}^{-2}$, 30 times greater than that depicted by Fig. 1(b). Since the atom density on GaAs(110) is $8.84 \times 10^{14} \text{ cm}^{-2}$, the yield was about 1.3 atoms/ion. The uncertainty of the measured yield is about $\pm 15\%$, which is induced mainly by variations in ion flux. We measured the sputtering yield in this way for several incident energies and for both Ar^+ and Xe^+ . As the data plotted in Fig. 2 show, the yield is nearly a constant in the range of energies used. We also note that the yield was nearly constant in the range 675–775 K. This can be understood in terms of the competing effects of temperature, namely creation of thermally activated vacancies and disorder and the healing of damage induced by ion impact. Generally, both forms of disorder will increase the yield by reducing channeling.¹

The experimental results provide important insight into the ion-crystal impact process on GaAs(110). Most of the observed small pits (~ 1 –5 unit cells) are believed to be created by single knock-on collisions in which only a few atoms are displaced after a direct encounter with a bombarding ion. The larger sized pits are more likely generated by linear cascade events. Since the probability to initiate a collision cascade increases with primary ion energy, the average pit size should also increase with ion energy. While the experimental data show increases in the number of large-size pits and, hence, the average pit size, the magnitude of the observed increase is small. This probably indicates that many of the high-energy ion cascade events occur deep under the surface. Even for 5-keV Xe^+ bombardment, the resulting defects are rather limited in size.

The observation of small pits for GaAs(110) is in sharp contrast to that observed for 5-keV Xe^+ bombardment of Pt(111),⁸ where single collision events were found to cause a few hundred atoms to be ejected onto the surface. For Xe–Pt, these phenomena are definitely in the spike regime, and a large fraction of ion energy must be transferred in the

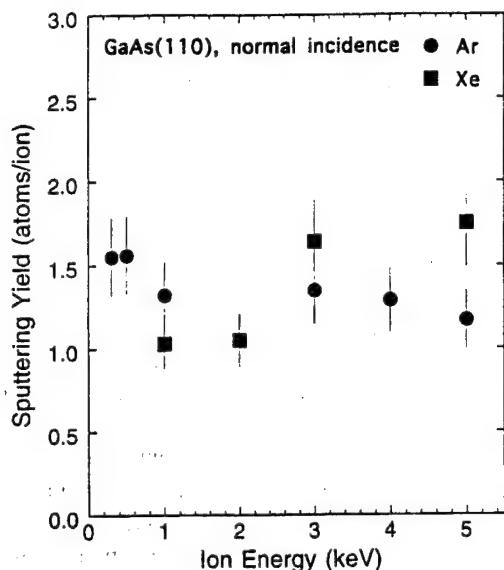


FIG. 2. Sputtering yield for Ar^+ and Xe^+ bombardment of GaAs(110) at normal incidence measured from STM images like Fig. 1(d).

collision processes. The insensitivity of sputtering yield with respect to ion energy and mass for GaAs(110) is also in contrast to the results of sputtering for metal and amorphous materials. STM measurements of Au(111)⁵ showed that the sputtering yield increased from 1 to 4 when the energy of Ne^+ varied from 600 eV to 3 keV. For amorphous Si targets, the sputtering yield was also found to increase significantly with ion energy and mass.¹⁰ Finally, molecular-dynamics simulations¹¹ predict a rapid increase of the sputtering yield with ion energy for crystalline Si targets.

These discrepancies indicate that the relative importance of the ion-solid interactions varies from material to material. The relatively small defect size and weak ion energy dependence of sputtering yield observed for GaAs(110) during the initial stages of sputtering indicate a lower stopping power [nuclear and/or electronic (Ref. 16)] and, therefore, lower energy deposition near the surface, compared with other cases studied quantitatively. In turn, the stopping power reflects differences in atomic bonding and electronic structures between these materials. First, channeling will reduce sputter damage, and the probability of channeling depends sensitively on the atomic configuration of the target. It is obvious that the ion channeling probability is very small for an amorphous target or for a sample that has been disordered during excessive bombardment [a common situation in traditional sputtering experiments (Ref. 10)]. The atomic structure of GaAs is open compared with that of metals (e.g., Au and Pt) due to its low atomic density. Consequently, it is expected that ion channeling is more probable for GaAs than for metals over relatively short distances, and major energy loss events will occur well below the surface. Furthermore, normal incidence on GaAs(110) corresponds to the [110] direction and this provides the largest channels. As direct evidence for the effect of channeling, we have observed significant variations in sputtering yield and defect size when the incident ion direction was changed.¹² Second, major dif-

ferences in electronic structure exist between GaAs and metals. The density of electrons of GaAs is lower than that of Pt, and the contrast is even more for the density of free carriers. The lower electron (and free-electron) density implies a lower stopping power. Finally, energy dissipation mechanisms, such as electron-phonon coupling,³ have a strong impact on the effect of ion bombardment. The exact nature of the dissipation process could be remarkably different even for similar materials.³ While such factors make the formulation of an accurate ion-surface interaction theory problematic, this work and that reported by others⁵⁻⁸ demonstrate that STM measurements can provide important information to reveal characteristics of the ion bombardment process. Ultimately, these could help determine the relative significance of material parameters in ion-crystal interaction.

In summary, we have observed that the bombardment of GaAs(110) surfaces with normal incident 300–5000 eV Ar^+ and Xe^+ is characterized by collision events in the single knock-on and linear cascade regimes. The defects generated are relatively small though the size increases gradually with ion energy. The sputtering yield is about 1.5, without noticeable dependence on ion energy and mass. The bombardment behavior on GaAs(110) is quite different than that on metal and amorphous surfaces, and this can be attributed to the high channeling probability and weak impinging ion-electron interaction.

The authors thank D. Rioux and M. Chander for helpful discussions. This work was supported by the U.S. Army Research Office.

¹ *Sputtering by Particle Bombardment I*, edited by R. Behrisch (Springer, Berlin, 1981).

² P. C. Zalm, *Surf. Interface Anal.* **11**, 1 (1988).

³ M. Ghaly and R. S. Averback, *Phys. Rev. Lett.* **72**, 364 (1994); C. P. Flynn and R. S. Averback, *Phys. Rev. B* **38**, 7118 (1988).

⁴ W. O. Hofer, in *Sputtering by Particle Bombardment III*, edited by R. Behrisch and K. Wittmaack (Springer, Berlin, 1991), p. 15.

⁵ C. A. Lang, C. F. Quate, and J. Nogami, *Appl. Phys. Lett.* **59**, 1696 (1991).

⁶ H. J. W. Zandvliet, H. B. Elswijk, E. J. van Loenen, and I. S. T. Tsong, *Phys. Rev. B* **46**, 7581 (1992).

⁷ H. Feil, H. J. W. Zandvliet, M.-H. Tsai, J. D. Dow, and I. S. T. Tsong, *Phys. Rev. Lett.* **69**, 3076 (1992).

⁸ C. Teichert, M. Hohage, T. Michely, and G. Comsa, *Phys. Rev. Lett.* **72**, 1682 (1994).

⁹ T. Michely and G. Comsa, *Nucl. Instrum. Methods Phys. Res. B* **82**, 207 (1993).

¹⁰ P. C. Zalm, *J. Appl. Phys.* **54**, 2660 (1983); S. Tachi and S. Okudaira, *J. Vac. Sci. Technol. B* **4**, 459 (1986).

¹¹ R. A. Stansfield, K. Broomfield, and D. C. Clary, *Phys. Rev. B* **39**, 7680 (1989); R. Smith, D. E. Harrison, Jr., and B. J. Garrison, *ibid.* **40**, 93 (1989).

¹² X.-S. Wang, R. J. Pechman, and J. H. Weaver (unpublished).

¹³ G. Lengel, R. Wilkins, G. Brown, M. Weimer, J. Gryko, and R. E. Allen, *Phys. Rev. Lett.* **72**, 836 (1994); L. Ruan, F. Besenbacher, I. Stensgaard, and E. Laegsgaard, *ibid.* **70**, 4079 (1993).

¹⁴ Y.-X. Wang and P. H. Holloway, *J. Vac. Sci. Technol. B* **2**, 613 (1984); J. B. Malherbe, W. O. Barnard, I. Le, R. Strydom, and C. W. Louw, *Surf. Interface Anal.* **18**, 491 (1992).

¹⁵ R. M. Feenstra, J. M. Woodall, and G. D. Pettit, *Phys. Rev. Lett.* **71**, 1176 (1993); J. F. Zheng, X. Liu, N. Newman, E. R. Weber, D. F. Ogletree, and M. Salmeron, *ibid.* **72**, 1490 (1994).

¹⁶ G. Carter and W. A. Grant, *Ion Implantation of Semiconductors* (Edward Arnold, London, 1976).

Appendix 3

Preprint of "Vacancy Kinetics and Sputtering on GaAs(110)"

R.J. Pechman, X.-S. Wang, and J.H. Weaver

To be published in Phys. Rev. B.

Vacancy Kinetics and Sputtering of GaAs(110)

R.J. Pechman, X.-S. Wang, and J.H. Weaver

Department of Materials Science and Chemical Engineering
University of Minnesota, Minneapolis, MN 55455

ABSTRACT

Bombardment of GaAs(110) at $300 \leq T \leq 775$ K with Ar^+ ions at normal incidence creates surface-layer defects that generally span 1 or 2 unit cells, as shown by scanning tunneling microscopy. Vacancies produced in this way diffuse via thermal activation to form single-layer vacancy islands. The diffusion of divacancies favors $[\bar{1}\bar{1}0]$ and accommodation at islands produces roughly isotropic islands. Modeling of growth showed an overall Arrhenius behavior for diffusion with an activation energy of 1.3 ± 0.2 eV. Investigations of the surface morphology during multilayer erosion revealed deviation from layer-by-layer removal with scaling exponents between 0.4 and 0.5 for $625 \leq T \leq 775$ K.

PACS: 61.80.Jh 68.35.Fx 61.16.Ch

INTRODUCTION

Ions play an important role in processes involved with overlayer growth and with material removal. For example, ion-assisted growth can lead to smoother films by creating defects that act as nucleation sites and by transferring energy to enhance diffusion. Material removal via reactive-ion or ion-assisted etching relies on energy provided to create chemically volatile species. Ions can also have adverse effects by creating disorder near the surface, as in vacancies in semiconductor materials. In such complex systems there are competing processes and it is important to understand each so that processing conditions can be optimized.

In this paper, we focus on defects created on GaAs(110) by noble gas bombardment and vacancy migration under the influence of temperature and sustained ion impact. Vacancies can be created on a semiconductor surface by sputtering with ions at energies of a few hundred to a few thousand eV. When done at elevated temperature, it is possible to promote near-surface healing and the defects can be characterized in terms of size and structure using atomic resolution scanning tunneling microscopy (STM). Vacancy kinetics can be extracted by relating surface morphology after erosion to vacancy migration and the formation of vacancy islands. In such circumstances, the results can be explained using some of the vocabulary of thin film growth. Such parallels to growth have been developed recently for sputter erosion¹⁻⁵ and for spontaneous etching.⁶⁻⁸

Here, the activation energy for diffusion of vacancies has been determined from the temperature-dependent size and density distribution of single-layer-deep vacancy islands. Denuded zone analysis indicates migration of divacancies along $[1\bar{1}0]$ and offers insight into the mechanism for vacancy motion. Extension of these investigations to high fluence resulted in multilayer erosion. Analysis of height profiles as a function of fluence and temperature shows that ideal layer-by-layer conditions could not be achieved. We attribute this to insufficient interlayer mass transport and, ultimately, the instability of GaAs against As desorption.

EXPERIMENTAL

The experiments were conducted in an ultrahigh vacuum chamber equipped with a Park Scientific Instruments STM. The base pressure was $\sim 1 \times 10^{-10}$ Torr. Clean (110) surfaces were prepared by cleaving GaAs posts that were doped p-type with Zn at $\sim 2 \times 10^{18} \text{ cm}^{-3}$ and n-type with Si at $\sim 1 \times 10^{17} \text{ cm}^{-3}$. Sputtering was done with a differentially pumped ion gun using high purity Ar introduced via a precision leak valve. The gun was thoroughly degassed before every bombardment. Vacancy island nucleation studies involved sputtering with 300 - 500 eV Ar^+ at fluxes of $3 - 6 \times 10^{11} \text{ ions-cm}^{-2}\text{-s}^{-1}$ at temperatures of 625 - 775 K. Multilayer erosion studies used 3000 eV Ar^+ at a flux of $1.9 \times 10^{12} \text{ ions-cm}^{-2}\text{-s}^{-1}$ at temperatures of 625 - 775 K. The pressure in the STM chamber did not exceed 6×10^{-9} Torr during bombardment. Temperatures were measured with a thermocouple near the sample base that was calibrated using an optical pyrometer. Quoted values were accurate to ± 20 K and reproducible to ± 10 K. This relatively large uncertainty reflects the fact that the samples were cleaved posts which had a range of shapes and overall profiles. The sample was cooled rapidly to room temperature after sputtering for STM experiments. Electrochemically-etched tungsten tips were cleaned *in situ* by electron irradiation. Micrographs shown here represent occupied states images (As sublattice) acquired in a constant current mode with biases of 1.5 - 3.0 V. They were not corrected for thermal drift and some show slight distortions. $[1\bar{1}0]$ runs from upper left to lower right in all images. The piezoelectric scanner was calibrated by comparing driftless atomic resolution images of GaAs(110) to the known lattice spacings and by measuring monatomic step heights on GaAs(110).

RESULTS AND DISCUSSION

A. Vacancy Island Nucleation and Growth

Wang *et al.*⁹ recently showed that Ar^+ ions having energies of 300 eV to 5000 eV induce surface damage on GaAs(110) that generally spans 1 - 5 unit cells where a unit cell is taken to be $4.00 \times 5.65 \text{ \AA}^2$. Room temperature sputtering indicated that some material ejected from pits by ion impact remained on the surface as adatoms. The adatoms produced by sputtering at $600 \leq T \leq 775$ K were mobile and thermal effects promoted local healing so that surface defects were well-

defined. For 300 eV ions, dual-bias imaging indicated that most impacts removed 1-4 atoms localized within a single row along $[1\bar{1}0]$. The yield of surface atoms removed per ion was constant when sputtering was done at normal incidence at $600 \leq T \leq 775$ K. The surface healing and the formation of vacancy islands appeared independent of the trajectory relative to the surface, even though effects due to trajectory and beam energy were clearly evident on the yield. Damage done deep within the sample was either healed or had no effect on the surface diffusivity of vacancies or vacancy complexes. Accordingly, we used Ar^+ at 300 eV and normal incidence to create the vacancies and small vacancy complexes whose behavior is quantified here. Figure 1 summarizes the results of analysis of these defects and shows that two-atom removal was the most likely under conditions where the damage was frozen and defect size could be estimated; defects more than five atoms in size generally spanned more than one row. The fluxes corresponded to removal of $1 - 5 \times 10^{-3}$ monolayer (ML) per second. This ensured that a vacancy created within a diffusion length of a vacancy island would reach that island instead of encountering other vacancies to produce a new island that was stable at the formation temperature. With increasing temperature, of course, the sampled area increased and island coarsening occurred. This is analogous to atom deposition on a surface where nucleation competes with growth in a way that depends on the proximity of the deposited atom to an existing island. Exposures were limited to the removal of ≤ 0.08 ML to ensure that the islands did not grow together.

Figure 2 shows images for surfaces sputtered with 300 eV Ar^+ at fixed fluence for $625 \leq T \leq 775$ K. The upper limit of temperature was dictated by the fact that As desorbs above 800 K, even without surface disorder induced by sputtering. Sputtering below 600 K produced surfaces that were dominated by structures comparable in size to those created by single ion impacts because diffusion was insufficient to allow island formation. Areal analysis for each of the surfaces shown in Fig. 2 indicates the removal of about 0.05 ML with a yield that was nearly constant. Inspection reveals that single-layer-deep vacancy islands, I, were the dominant structures. The lateral dimension of these islands increased with temperature and their density decreased. Annealing for 5-15 min at the sputtering temperature did not alter the island density. Thus, their motion on the surface was sufficiently sluggish to prevent them from joining with other

islands. In addition, annealing to 775 K after sputtering at 625 and 675 K resulted in the same island density and size distribution as produced by sputtering at 775 K.

The STM images also revealed bright structures (A) that reflect material ejected onto the surface. Dual bias imaging typically showed these bright spots in both polarities and that they extend ~ 5 Å. For room temperature sputtering, the surface area covered by A-type features scaled with the pit area.⁹ These features were stable against tip-induced displacement under the imaging conditions used here. They were observed less frequently at higher temperatures because they could recombine with vacancy islands or, for As_x species, they could desorb. Annealing after sputtering at lower temperatures reduced the density of A-type features. We found no evidence for regrowth features on the surface layer of the sort seen for $\text{Si}(100)$ ^{1,5,7,8} or for adatom chains as reported for $\text{GaAs}(110)$.¹⁰

Figure 3(a) shows an image obtained after sputtering of a region having two monatomic steps running along $[001]$. The surface far from the steps was equivalent to that of Fig. 2(b), but the areal density of vacancies was much reduced close to the steps. Such denuded zones, labeled DZ, were absent along $[1\bar{1}0]$ steps, as shown in Fig. 3(b). This indicates that divacancy diffusion is preferred along the zig-zag chains of alternating Ga and As sites, perpendicular to $[001]$. The kinks along $[001]$ steps represent sites where vacancies were accommodated. Divacancies created sufficiently close to the $[001]$ step on the upper terrace were able to annihilate at the step. Those that diffused to the step from the lower terrace were not able to annihilate because this would involve atom dissociation from the step and transfer to the vacancy. These vacancies were reflected back onto the terrace under these low fluence conditions. Only at higher fluence did we observe the formation of extended vacancies along the step direction in the lower terrace, corresponding to creation of a double height step. The larger kinks along the edge in Fig. 3(b) probably represent vacancy islands that grew near the step and “broke through.” The linear density of these kinks is equal to the linear density of vacancy islands along $[1\bar{1}0]$ far from $[1\bar{1}0]$ steps.

Figure 3(c) depicts the top layer of a $\text{GaAs}(110)$ terrace with a single As vacancy (V_{As}), two GaAs divacancies (V_{GaAs}), and a vacancy island. The island is bounded by two GaAs $[1\bar{1}0]$ chains. The one on the right is terminated by As atoms while that on the left is terminated by Ga

atoms. The top and bottom edges are regular $[001]$ steps and the overall island is charge neutral. Atoms within the exposed second layer of GaAs are also shown. The images of Fig. 2 reveal such single-layer deep islands but with borders that are less regular because of kink sites and segments of $\langle 112 \rangle$ -type steps. Dual-bias imaging and inspection of the atomic sites of the exposed second layer shows the Ga and As aspects of the $[1\bar{1}0]$ and $[001]$ edges.

Vacancy diffusion can be visualized from Fig. 3(c). For a V_{GaAs} unit like II or III, movement by one atomic site along $[1\bar{1}0]$ will occur when a Ga or As atom jumps from one end of the vacancy to an equivalent site at the other end, as depicted by the dashed downward arrows, and discussed for GaAs(110) by Gwo *et al.*¹⁰ and Lengel *et al.*¹¹ Motion of V_{GaAs} (or larger complexes contained within a zig-zag row having an even number of missing atoms) can be accomplished by net hopping of As and Ga atoms along $[1\bar{1}0]$. The activation energy for such diffusion is dominated by the breaking of one surface bond and one backbond as the atom dissociates from one end of the vacancy. The divacancies depicted in Fig 3(c) could be accommodated at the island such that II would cause elongation along $[001]$ and III elongation along $[1\bar{1}0]$. The fact that the aspect ratio for the islands in Fig. 2 is approximately unity indicates accommodation at both types of island edges.

Gwo *et al.*¹⁰ have assessed diffusion anisotropy of native vacancy complexes on purposely mis-cleaved GaAs(110) at 300 K. Multiple scanning of the same area revealed occasional vacancy hopping events along $[1\bar{1}0]$ and far fewer hops along $[001]$ that led them to deduce an anisotropy in diffusion of $\sim 10^3$ in favor of motion along the zig-zag rows. Ebert *et al.*¹² found tunneling conditions under which they were able to move divacancies along the zig-zag rows of GaP(110) with an STM tip at 300 K. Lengel *et al.*¹¹ performed a similar study concerning single As vacancy hopping events on GaAs(110). They found that V_{As} moved across zig-zag rows, as depicted by the horizontal arrow in Fig. 3(c) under the influence of the tip. Such an event involves breaking of only one backbond and bond rotation of the surface bonds as the atom swings out of the surface plane and into the vacancy site.¹¹ The alternate pathway, diffusion of a single vacancy along $[1\bar{1}0]$, is unlikely because an event that avoids an antisite defect must break at least one surface bond and a backbond somewhere along its path while overcoming a barrier to motion that is complicated

by the presence of the opposite species [e.g. the Ga atoms on either end of the As vacancy in defect I in Fig. 3(c).] Lengel *et al.* deduced activation energy barriers of ~ 1.5 and ~ 3.5 eV for these two channels. We have not observed tip-induced diffusion at 300 K and we deliberately imaged at low bias to avoid tip effects. Tip-induced events are easily detected by discontinuities in successive line scans at the affected site and by differences in successive images of the same area. We conclude that the tip did not play a significant role in activating the large number of vacancy hops needed to produce the observed vacancy islands.

Sputtering at low energy can create trivacancies in a single row. Motion for trivacancies along $[1\bar{1}0]$ is complicated by the barrier just noted for single atom vacancies. These immobile, odd-numbered vacancies can be converted to even-number structures via capture of a single atom vacancy or capture of a surface adatom. Alternatively, a trivacancy can dissociate into a divacancy and a single atom vacancy on an adjacent row, both of which can diffuse along their low-energy directions. In this case, the final thermodynamic state involves a net loss of one surface bond.

The shape of a vacancy island will change as atoms at the perimeter break away, diffuse on the island floor, and are rebonded. Dissociation events like IV and V in Fig. 3(c) are governed by the same bond breaking energies as for V_{GaAs} diffusion. Accommodation of an atom diffusing on an island floor must be limited to chemically favorable sites. The result of atom dissociation from edges and reaccommodation at favorable sites is a reduction in kinks at vacancy island borders, leading to a smooth appearance of edges.

The activation energy for diffusion, E_d , can be calculated from analysis of images like those of Fig. 2 where island densities can be determined directly. The area associated with each island defines an average separation between islands. The problem of determining E_d is analogous to determining activation energies for diffusion of adatoms and clusters during growth. Mo *et al.*¹³ have proposed a model that takes an atomistic view, first counting the number of sites visited by a diffusing species after H hops of length a . When H is large and diffusion is highly anisotropic, the number of distinct sites visited is $\sim H^{1/2}$. The island density, N , is important when calculating the number of hops needed to find an existing island. From this a nucleation rate, dN/dt , can be deduced that depends on diffusivity, D , deposition rate, R , and total coverage, θ . Integration then

gives $N^7 = 7R^2\theta/D^2a^4$. Since N is determined by counting the islands, D can be calculated. This applies only to systems with highly anisotropic diffusion, low coverages where island radii are much smaller than the average island separation, and for low deposition rates where diffusing species interrogate large areas before encountering other migrating species. The low Ar^+ fluxes and fluences used for our pit nucleation studies and the results of denuded zone analysis ensured that these conditions were satisfied.

The calculation of an activation energy for diffusion requires that there is a single dominant pathway so that competing rate processes can be neglected. In our case, the rate processes can be categorized as vacancy creation, annihilation, migration, and nucleation and growth. Vacancy creation is governed by Ar^+ impact events, and removal was found to be constant with temperature at the fluxes used here. Vacancy annihilation occurs when adatoms fill vacancies. For $625 \leq T \leq 775$ K, the adatoms could combine with vacancies and were not often observed. Such events must have occurred locally as part of the healing of disorder at impact sites and their time scale must have been much shorter than that for vacancy migration. By limiting the amount of material removed, the effects of growth rate were minimized, and it is reasonable to expect that vacancy accommodation at island edges was not sensitive to temperature in the range of interest. Finally, the rate of island nucleation was certainly temperature dependent and tied to island density. This was exploited to calculate the activation energy for divacancy migration. Thus, the conditions of low flux ensured that vacancy diffusion was the rate process that was important in these nucleation studies.

Figure 4 summarizes the results of calculating D from the island density for surfaces sputtered at 625, 675, 725, and 775 K. Each datum point represents D averaged over vacancy island densities for fluences that resulted in 1-8% vacancy coverage. Hundreds of vacancy islands were counted for each experiment with at least four experiments done at different fluences for each of the four temperatures studied. Linearity of the fit indicates that vacancy diffusion follows an Arrhenius behavior. The slope gives $\Delta E_d = 1.3 \pm 0.2 \text{ eV}^{14}$ where the uncertainty reflects variations in ion flux during bombardment.⁹ This activation energy reflects divacancy motion along zig-zag chains. Single vacancies that were created contributed to island growth but the fact

that they were rarely observed after sputtering at elevated temperature indicates that they were sufficiently mobile to be accommodated at vacancy islands. While incorporation into an existing island would not affect the island density, it would alter the diffusion characteristics of the island, as noted above. For example, capture of a single vacancy by a divacancy would immobilize the complex and prevent the divacancy from sampling its full diffusion length. The net effect of such processes would be an increase in island density. The measured value for E_d would then be higher than it should be for simple divacancy diffusion. We estimate that the slope of the Arrhenius plot would give a higher value for E_d by ~ 0.1 eV if the presence of single vacancies led to an increase in island density by 20%. This was deduced by rescaling the original island density data to reflect a 20% reduction and then recalculating D .

B. Multilayer Erosion

The above has focused on vacancy islands in the top layer. With continued material removal, top layer islands grow and coalesce and new islands can be produced in the exposed layer before original layers are completely eroded. As the surface morphology evolves, vacancy accommodation at upper and lower steps becomes increasingly important in determining pit shapes and the probability for interlayer mass transport.

Wang *et al.*⁹ have shown that the sputtering yield for normal incidence bombardment of GaAs(110) depends weakly on ion energy because the probability for channeling increases with energy. However, the vacancy size produced by individual ions averages 4 - 6 atoms at 3000 eV instead of 2 - 4 atoms for 300 eV. In multilayer erosion studies, we used 3000 eV ions and higher fluxes to minimize exposure times and main chamber pressure. The total amount of material removed was determined by scaling the sputter yield with the total ion exposure, again expressing the value in monolayer-equivalents of GaAs(110). These values were checked against areal analysis of exposed layers for lower fluences where the original surface could be identified.

Figure 5 shows the surface morphology after removal of 0.9 ML and 9.5 ML at 725 K. It is clear from the images that erosion proceeds in a simultaneous multilayer fashion with the probability of sputter removal from a particular layer governed by the fractional area exposed. In

general, these surfaces are comprised of a main layer, M, remnant islands, R, and vacancy islands, I. The total number of layers reflects the effectiveness of interlayer transfer, a temperature-dependent quality. The remnant structures appear in stacks as more material is removed and the step height between layers is generally one layer. The single-layer vacancy islands also appear in stacks as more material is removed. Figure 5(c) represents a general height profile after multilayer erosion. The horizontal axis is the fast diffusion direction for divacancies and possible vacancy accommodation mechanisms are indicated by I-V. In I, a vacancy in the main layer diffuses to a vacancy island and is accommodated. In II, a vacancy island abuts a portion of a remnant island where an atom dissociates from the upper terrace and is transported into the vacancy island. This interlayer vacancy diffusion via atom transfer reduces the root mean square surface roughness. In III, a vacancy in a remnant island diffuses to a single height [001] step and reduces the size of the remnant. In IV, a next layer vacancy migrates to an edge to form a double-height step. In V, an adatom liberated from a remnant island is accommodated at a favorable site of a step edge. This interlayer atom diffusion also reduces surface roughness. The shapes and distributions of the structures on eroded surfaces offers insight into the importance of these vacancy accommodation and interlayer mass transport phenomena.

In Fig. 5(a) there is no preferred alignment of the vacancy islands relative to the substrate crystallographic directions and the islands have aspect ratios that are roughly 1:1. This indicates vacancy accommodation at both local [001] and $[1\bar{1}0]$ steps. The remnant islands in Fig. 5(a) do show elongation but there is no preferential alignment because the island shape reflects vacancy coalescence. Remnant structures are formed when two isotropic vacancy islands meet, grow, and engulf other vacancy islands. Other growing vacancy islands are more likely to meet this large elongated one along the extended edge. If coalescence happens near an end point, the vacancy island will form a "C" shape that may meet itself at the ends, forming an elongated remnant island. The vacancy and remnant islands are bordered by irregular edges made up of segments of $[1\bar{1}0]$ and [001] steps. The $[1\bar{1}0]$ segments tend to be atomically straight over a few to several tens of angstroms while the [001] steps are more kinked. This reflects the weaker interaction between adjacent chains compared to atoms in the same chain, as well as the higher probability for

divacancy annihilation at [001] steps. Occasionally, double-height steps are formed at the junction of a vacancy island and remnant island [center of Fig. 5(a)]. In all cases, the double-height step segment roughly follows $[1\bar{1}0]$ or $\langle 112 \rangle$. Double-height steps along these directions form {111} microfacets. This is favorable since GaAs(111) reconstructs with a two-times periodicity to reduce the number of dangling bonds at a double-height edge. Such microfaceting was also observed following spontaneous etching of GaAs(110) with Br_2 and Cl_2 .¹⁵

Figures 5(a) and 5(b) show that the average height deviation from the main layer increased with material removal at 725 K. Studies of multilayer sputtering at 625, 675, and 775 K showed the same trend. A measure of roughening can be obtained by defining an interface width, $\langle H \rangle = [\langle h^2(x) \rangle - \langle h(x) \rangle^2]^{1/2}$, where $h(x)$ is the height at position x and $\langle \rangle$ denotes the average over the measured area. Here, interface widths were calculated as a function of total material removed for the different temperatures of sputtering. When measured along a particular dimension, $\langle H \rangle$ showed no directional dependence so that the roughness was independent on the choice of axis. This quantifies the observation above that there was no preferred shape or orientation for pits and islands formed during erosion.

Figure 6 plots the temperature dependence of the interface width versus material removed for surfaces sputtered at 625, 675, 725, and 775 K. Fewer data points were available for surfaces sputtered at 625 and 675 K since significant roughness for high fluences resulted in structures that were difficult to probe with an STM tip (deep and narrow). The slope of the linear best fit for each data set decreases from 0.5 at 625 K to 0.4 at 775 K. This is consistent with a “growth” law whereby the interface width increases with time as $\langle H \rangle \propto t^\beta$ during deposition at constant flux and the growth exponent β depends on temperature. Thus, Fig. 6 reflects the dependence of the scaling exponent β on temperature for multilayer erosion.

Discussions of the growth exponent and its temperature dependence¹⁶⁻¹⁹ show that $\beta = 0.5$ corresponds to a situation where there is no net mass transport between layers, and the morphology is statistically consistent with an ideal “hit and stick” picture. With increasing temperature, β decreases and there is a transition temperature at which it goes to 0, reflecting a steady-state characterized by layer-by-layer growth and an interface width that is independent of

time. β increases again above the roughening temperature because the adatom sticking probability decreases, the effects of thermal desorption can not be ignored, and the growth front is roughened.^{18,20}

From Fig. 6, it is clear that the erosion studied here for GaAs(110) occurs below the transition temperature since β did not reach a value near 0 and ideal layer-by-layer material removal was not observed. Erosion analogous to the roughening transition of growth occurs at ~ 800 K, corresponding to thermal desorption of As as As_x .²¹ Accordingly, conditions where ideal layer-by-layer sputtering occurs cannot be realized. It should be noted that the behavior of β with time is asymptotic and quantitation may require the removal of many tens of monolayers to obtain an accurate value. However, roughening observed here occurred sufficiently fast to determine the trend of β with temperature. Additional information about roughening during erosion can be obtained by tracking step density with temperature and fluence. Such analyses and the implication for quantitative understanding of physical erosion of GaAs will be described in detail elsewhere.²²

Figure 7 shows STM images of surfaces sputtered to remove 1.5 ML at $625 \leq T \leq 775$ K. At 625 K, six layers are visible and the range of lateral continuity is small; at 775 K, four layers are visible and the terraces are large, indicating increased intra- and interlayer migration at higher temperature. Inspection reveals structures with relatively small lateral dimensions and little change from 625 to 675 K. More noticeable lateral smoothing occurred at 725 and 775 K, although mathematical analysis shows that the scaling exponent changed only from 0.5 to 0.4 (Fig. 6), which indicates that interlayer mass transport is much more difficult than same-layer diffusion. Indeed, the interface width increases with time in an unbounded fashion during erosion.

The lateral dimension of structures after erosion reflects the details of lateral diffusion. Inspection of the images indicates that a main layer vacancy created on the surface in Fig. 7(d) would need to travel ~ 10 times farther to find a suitable accommodation site than for a main layer vacancy on the surface in Fig. 7(a). From Fig. 4, divacancy diffusivity is ~ 100 times larger at 775 K for Fig. 7(d) than at 625 K for Fig. 7(a). The diffusion lengths, $x = \sqrt{Dt}$, then differ by a factor of ten for the same time. Thus, the average lateral size correlates well with the lateral diffusivity, and the ranges of motion for vacancies governed by terrace sizes and by diffusion lengths scale

equally with temperature. However, this does not account for the reduced roughness seen at the higher temperatures.

To understand the role of interlayer mass transport in reducing the surface roughness, we refer back to Fig. 5(c). Events like II and V constitute interlayer diffusion of vacancies and liberated atoms and decrease the interface width. Structure IV represents a vacancy created within an island. The size of the vacancy island will scale with temperature, as does the diffusion length. Moreover, the vacancy will be reflected back into the island floor when accommodation at the boundaries is not possible. Each time the vacancy reaches an edge there is a chance for an interlayer diffusion event like that depicted as II of Fig. 5(c). The fact that island boundary sampling rates are roughly independent of temperature indicates that interface smoothing is due to the activation barrier to interlayer diffusion events and not a reduction in the frequency factor (i.e. number of attempts) at lower temperatures.

In addition to the mechanism of interlayer vacancy motion, events like V in Fig. 5(c) could occur to reduce the interface width. Such events represent atom dissociation from a remnant structure. The atom may then interrogate the surface to find a chemically favorable site at a remnant island or at a vacancy island. An encounter with a vacancy island would result in interlayer diffusion if the mobile atom hopped down at the island boundary and was accommodated. In principle, the diffusing adatom could encounter another liberated adatom and nucleate a separate island or, for the case of volatile As_x moieties, desorb. Such processes appear unlikely since we have not observed small islands or detected a temperature dependence in the sputtering yield that would suggest significant desorption of As at higher temperatures. Moreover, we have annealed surfaces like those shown in Fig. 7 to their respective sputtering temperatures for 5 - 10 minutes and observed no noticeable change in the size of remnant or vacancy islands or in surface roughness. This indicates that dissociation events like process V in Fig. 5(c) are not important for net interlayer mass transport and cannot exclusively account for the reduction of interface width with temperature. We conclude that the unbounded surface roughening correlates to the difficulty of interlayer vacancy diffusion relative to the in-plane migration of these vacancies.

CONCLUSIONS

This paper has focused on the morphology of GaAs(110) under low and medium energy Ar⁺ bombardment. STM analysis of vacancy island nucleation has shown an Arrhenius behavior for vacancy diffusion with an activation energy for divacancy diffusion of 1.3 ± 0.2 eV. Multilayer erosion studies revealed that sputtering leads to surface roughening below 775 K. Coverage- and temperature-dependent measurements of the interface width after bombardment showed ineffective mass transport between layers. It will be interesting to extend these studies to include ion enhanced growth and etching to gain insight into more complicated materials processing problems.

ACKNOWLEDGEMENTS

This work was supported by the Army Research Office. The authors gratefully acknowledge discussions with D. Rioux, C.M. Aldao, D.W. Owens, and P.J. Benning.

REFERENCES

1. P. Bedrossian, J.E. Houston, J.Y. Tsao, E. Chason, and S.T. Picraux, *Phys. Rev. Lett.* **67**, 124 (1991); P. Bedrossian, *Surf. Sci.* **301**, 223 (1994).
2. S. Gauthier, Y. Samson, J.C. Girard, S. Rousset, and J. Klein, *J. Vac. Sci. Technol. B* **12**, 1754 (1994).
3. T. Michely and G. Comsa, *Nucl. Instr. Methods. Phys. Research B* **82**, 207 (1993).
4. J.C. Girard, Y. Samson, S. Gauthier, S. Rousset, and J. Klein, *Surf. Sci.* **302**, 73 (1994).
5. H.J.W. Zandvliet, H.B. Elswijk, E.J. van Loenen, and I.S.T. Tsong, *Phys. Rev. B* **46**, 7581 (1992).
6. J.C. Patrin, Y.Z. Li, M. Chander, and J.H. Weaver, *Appl. Phys. Lett.* **62**, 1277 (1993).
7. D. Rioux, R.J. Pechman, M. Chander, and J.H. Weaver, *Phys. Rev. B* **50**, 4430 (1994).
8. M. Chander, Y.Z. Li, J.C. Patrin, and J.H. Weaver, *Phys. Rev. B* **47**, 13035 (1993).
9. X.-S. Wang, R.J. Pechman, and J.H. Weaver, *Appl. Phys. Lett.* **65**, 2818 (1994); X.-S. Wang, R.J. Pechman, and J.H. Weaver, *J. Vac. Sci. Technol.* (submitted).
10. S. Gwo, A.R. Smith, and C.K. Shih, *J. Vac. Sci. Technol. A* **11**, 1644 (1993).
11. G. Lengel, M. Weimer, J. Gryko, and R.E. Allen, *J. Vac. Sci. Technol. A* **12**, 1855 (1994).
12. P. Ebert, M.G. Lagally, and K. Urban, *Phys. Rev. Lett.* **70**, 1437 (1993).
13. Y.-W. Mo, J. Kleiner, M.B. Webb, and M.G. Lagally, *Phys. Rev. Lett.* **66**, 1998 (1991).
14. This value is lower than the typical value of ~ 1.7 eV reported for bulk diffusion of Ga vacancies, consistent with the fact that the diffusion at surfaces is more facile than in the bulk. See T.Y. Tan, U. Gösele, and S. Yu, *Crit. Rev. Solid State Mater. Sci.* **17**, 47 (1991); D.E. Bliss, W. Walukiewicz, and E.E. Haller, *J. Elect. Mat.* **22**, 1401 (1993); and J.-L. Rouviere, Y. Kim, J. Cunningham, J.A. Rentschler, A. Bourret, and A. Ourmazd, *Phys. Rev. Lett.* **68**, 2798 (1992).
15. J.C. Patrin and J.H. Weaver, *Phys. Rev. B* **48**, 17913 (1993).
16. M.G. Lagally, R. Kariotis, B.S. Swartzentruber, and Y.-W. Mo, *Ultramicroscopy* **31**, 87 (1989).
17. R. Kariotis, and M.G. Lagally, *J. Vac. Sci. Technol. B* **7**, 269 (1989).

18. Z. Zhang, J. Detch, and H. Metiu, Phys. Rev. B **48**, 4972 (1993).
19. Z.-W. Lai, and S. Das Sarma, Phys. Rev. Lett. **66**, 2348 (1991).
20. Y.-W. Mo, R. Kariotis, D.E. Savage, and M.G. Lagally, Surf. Sci. **219**, L551 (1989).
21. We have observed sample degradation and the effects of Ga puddle formation at temperatures between 775 K and 800 K.
22. X.-S. Wang, R.J. Pechman, and J.H. Weaver (unpublished).

FIGURE CAPTIONS

- FIG. 1** Size distribution of defects formed by individual 300 eV Ar⁺ impacts. Defects corresponding to two atoms are the dominant structures. For defects greater than about five atoms, the structures extend over two $[1\bar{1}0]$ chains.
- FIG. 2** $250 \times 250 \text{ \AA}^2$ images of GaAs(110) sputtered with 300 eV Ar⁺ at 3×10^{11} ions-cm⁻²-s⁻¹ to remove ~ 0.05 ML. I denotes single-layer-deep vacancy islands and A labels features associated with material ejected onto the surface.
- FIG. 3** (a) $450 \times 450 \text{ \AA}^2$ image showing a denuded zone (DZ) near a $[001]$ step, labeled $S_{[001]}$. The island density is reduced near down-steps (upper left) but unaffected near up-steps (lower right). A typical vacancy island is indicated by I. (b) $470 \times 470 \text{ \AA}^2$ image of a surface sputtered to remove twice as much material as in (a). A monatomic $[1\bar{1}0]$ step is seen and no denuded zone exists. (c) Schematic representation of GaAs(110) with Ga atoms shown as filled circles and As atoms as open circles. Distinct vacancy sites are shown: a single As vacancy (V_{As}), two GaAs divacancies (V_{GaAs}), and a larger vacancy island. The zig-zag row direction is indicated. Diffusion of V_{GaAs} -type defects was found to be highly anisotropic along $[1\bar{1}0]$. The arrows indicate that single atom hopping is the mechanism for net displacement.
- FIG. 4** Plot of vacancy diffusivity vs. $1/T$. The slope of the straight line fit gives the activation energy for diffusion, $E_d = 1.3 \pm 0.2$ eV. Vertical error bars account for flux variations during bombardment.
- FIG. 5** $800 \times 800 \text{ \AA}^2$ images of GaAs(110) sputtered with 3000 eV Ar⁺ at 1.9×10^{12} ions-cm⁻²-s⁻¹ at 725 K to remove (a) 0.9 ML and (b) 9.5 ML. Each surface is comprised of a main layer (M), remnant layers (R), and vacancy islands (I). Three layers are exposed in (a) whereas at least eight layers are exposed in (b). (c) Surface profile during multilayer erosion depicting possible vacancy accommodation and annihilation events.
- FIG. 6** Log-log plot of the interface width, $\langle H \rangle$, versus total amount of material removed for sputtering between 625 and 775 K. The errors involved are represented by the size of

the symbols. The slope of each line gives the scaling exponent, β , at the corresponding temperature. β decreases slightly from 0.5 at 625 K to 0.4 at 775 K.

FIG. 7 $800 \times 800 \text{ \AA}^2$ STM images of GaAs(110) sputtered with 3000 eV Ar⁺ at 1.9×10^{12} ions-cm⁻²-s⁻¹ to remove ~ 1.5 ML. The morphology appears much smoother for the surfaces sputtered at higher temperatures although the interface width grows in an unbounded fashion due to ineffective mass transport between layers.

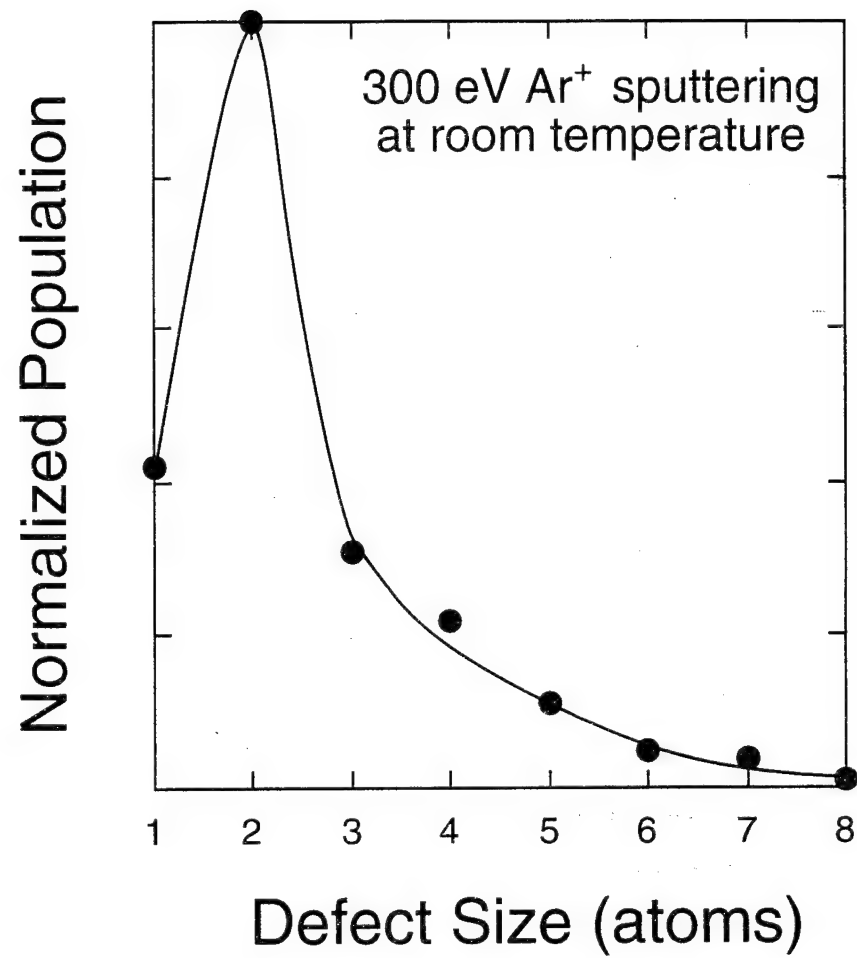


FIG. 1

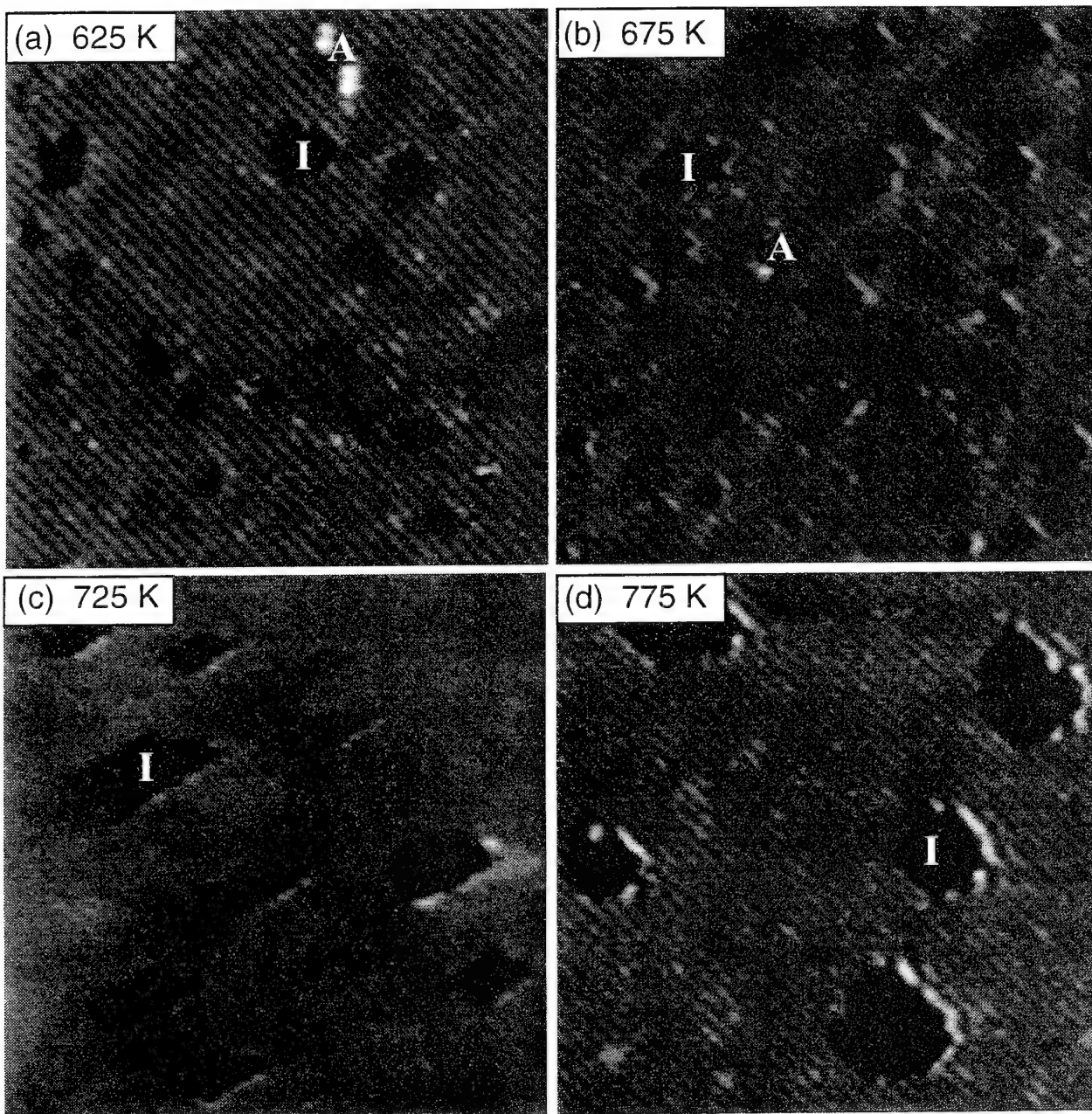


FIG. 2

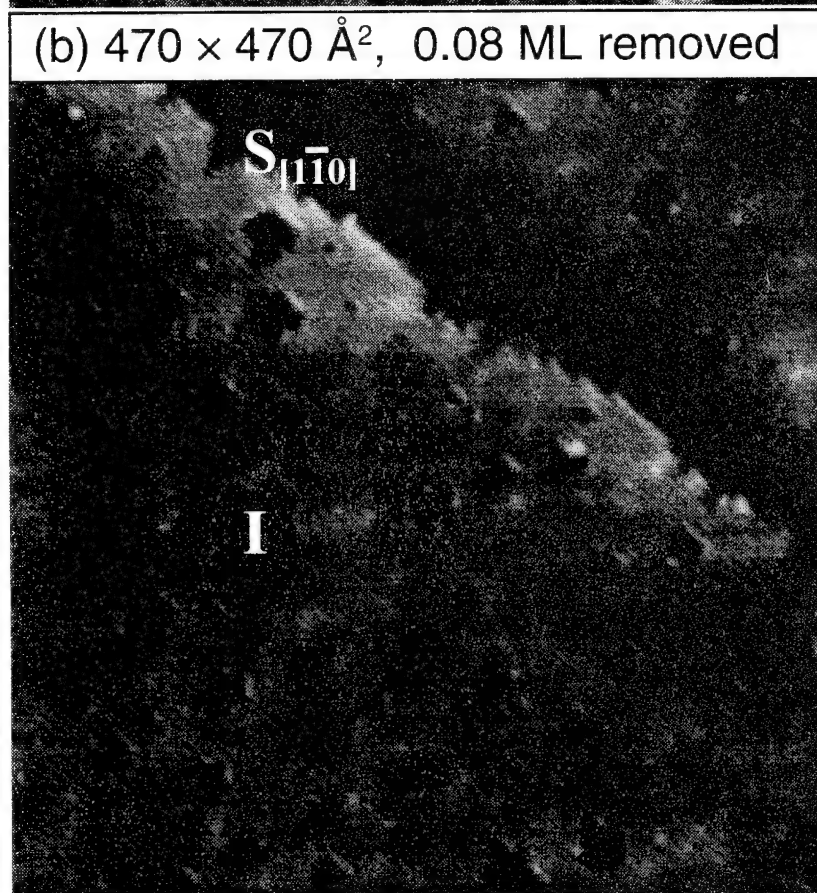
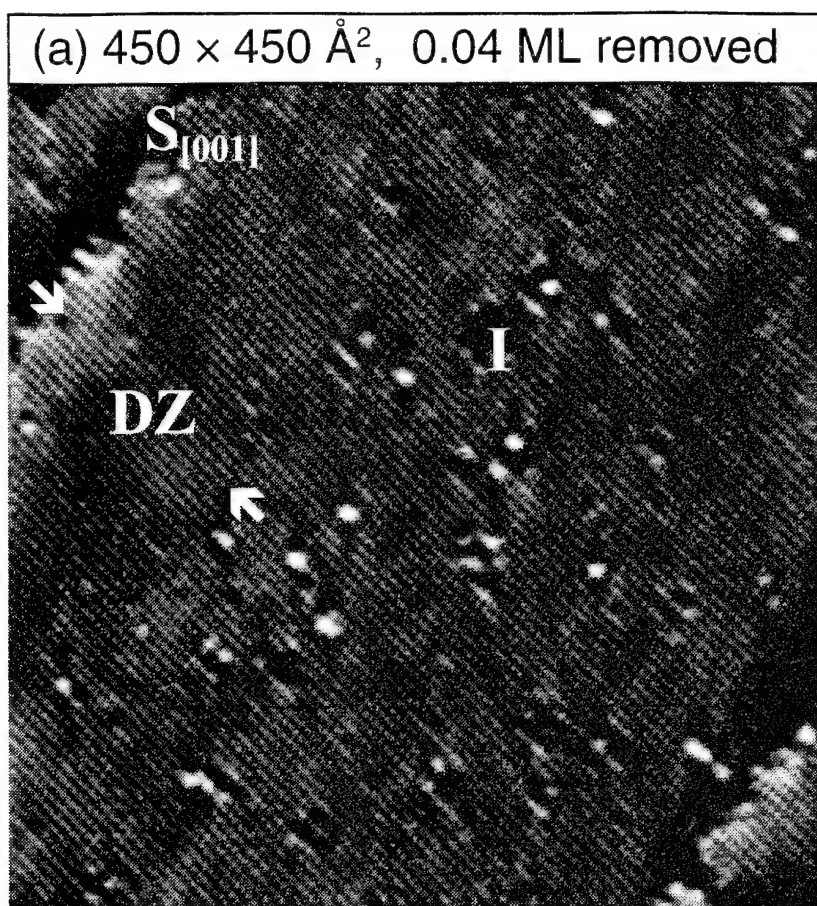


FIG. 3

(c)

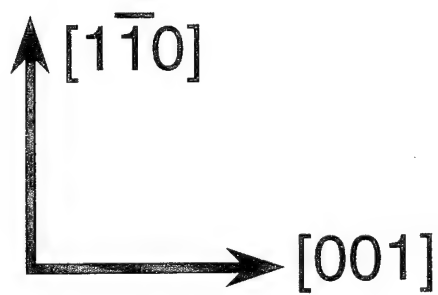
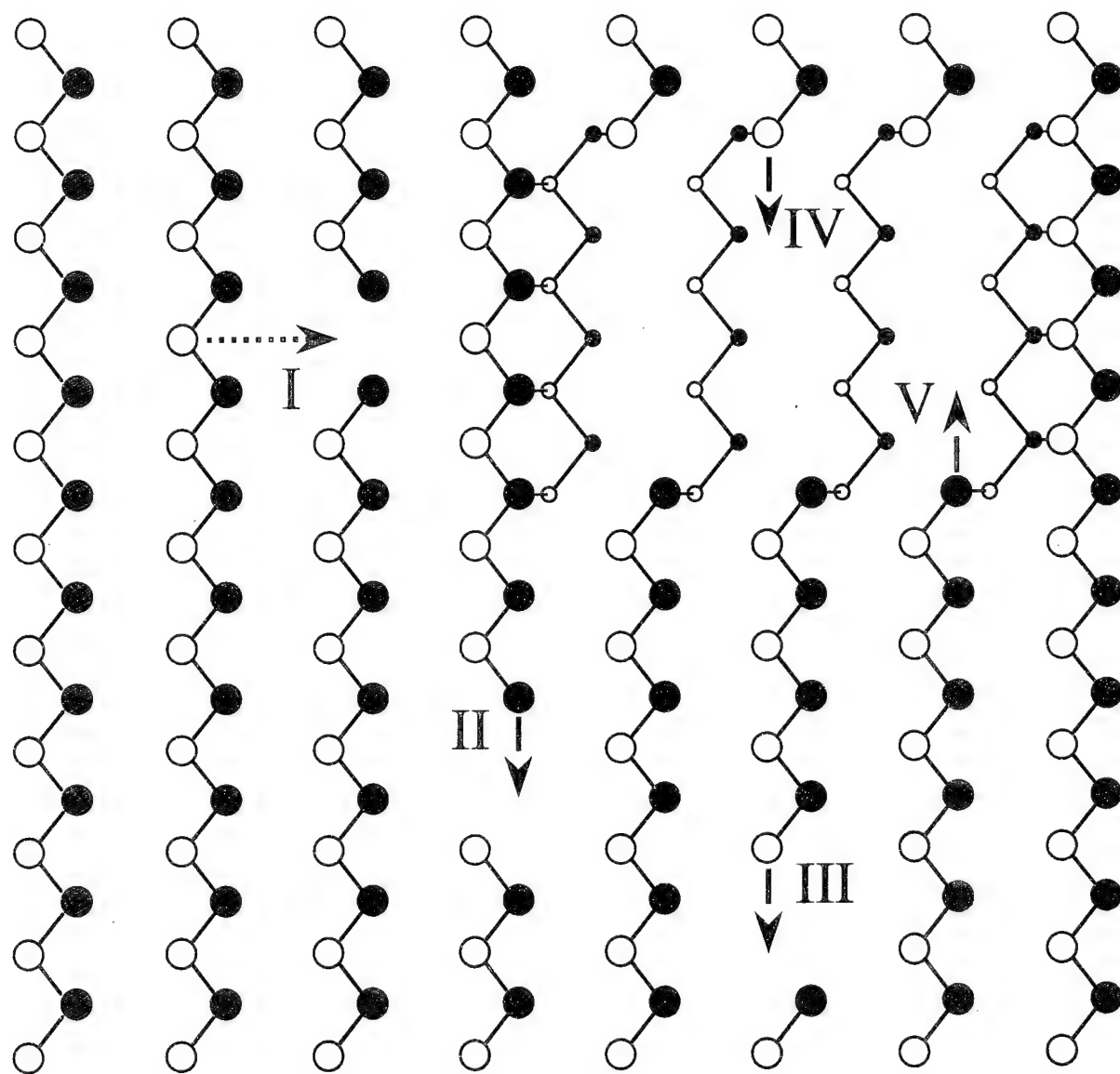


FIG. 3

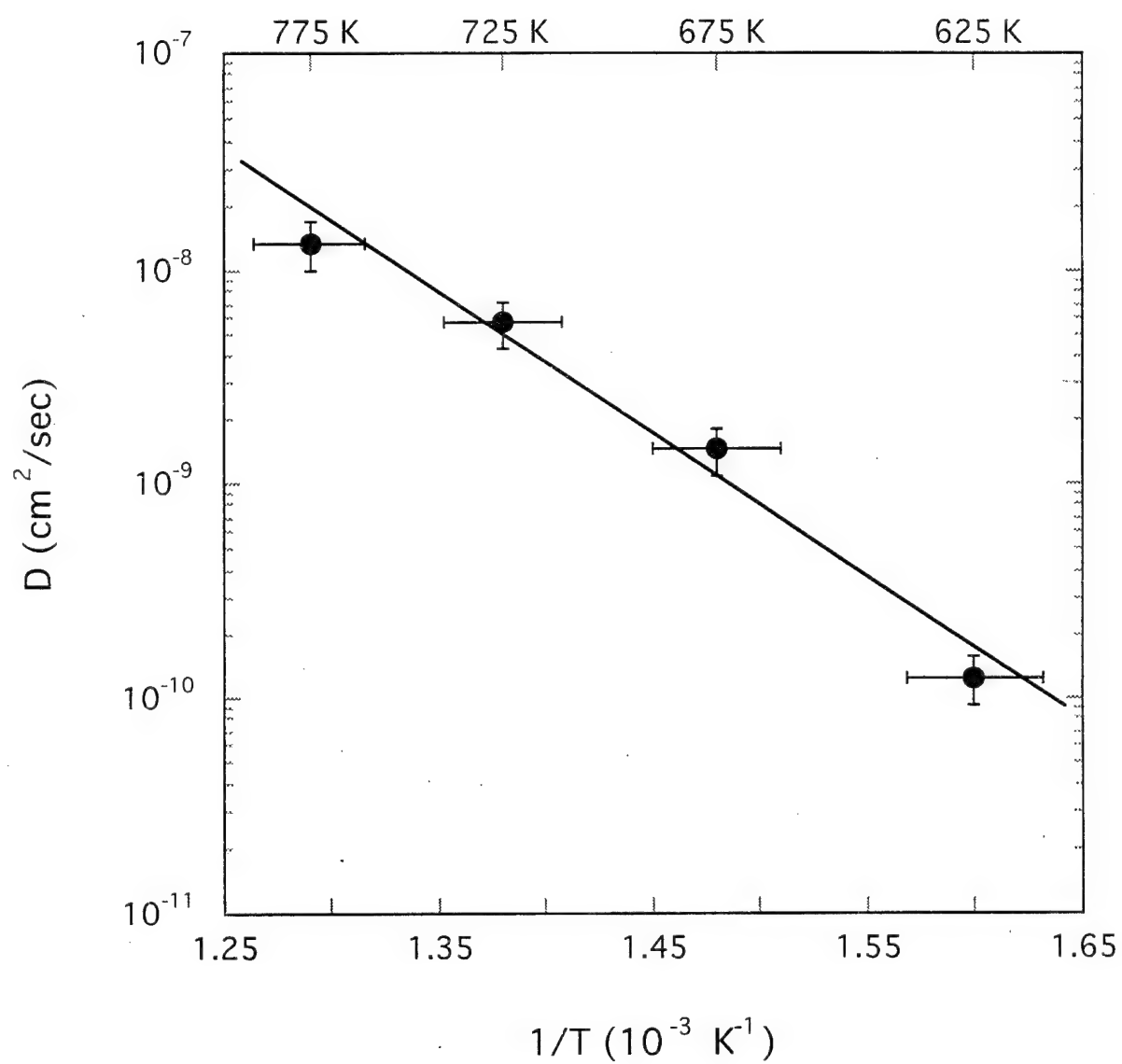


FIG. 4

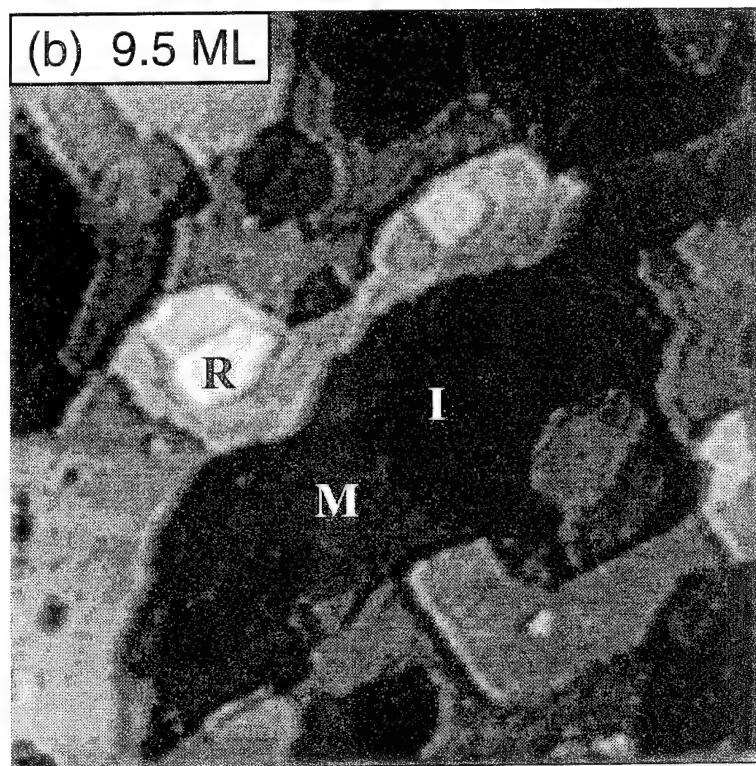
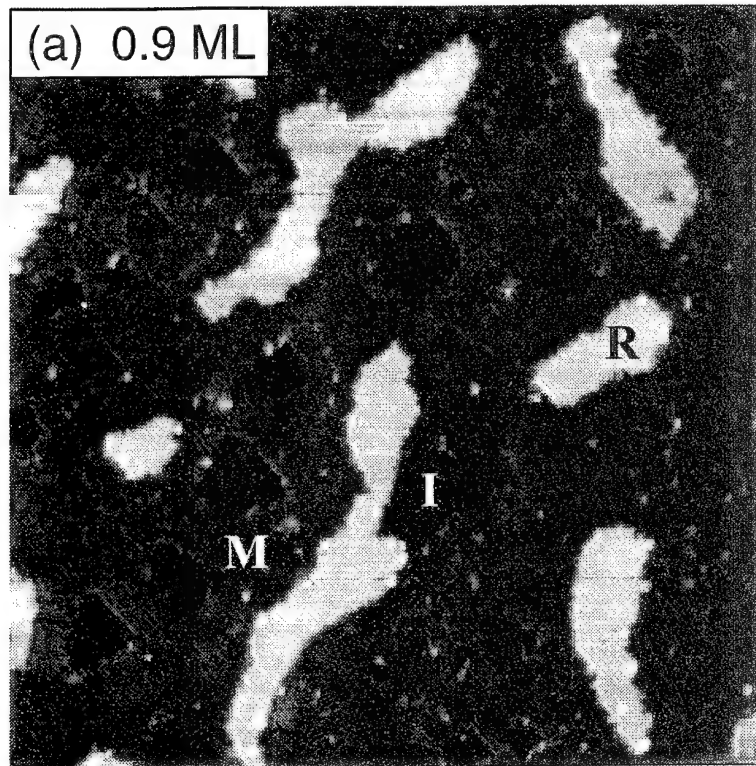


FIG. 5

(c)

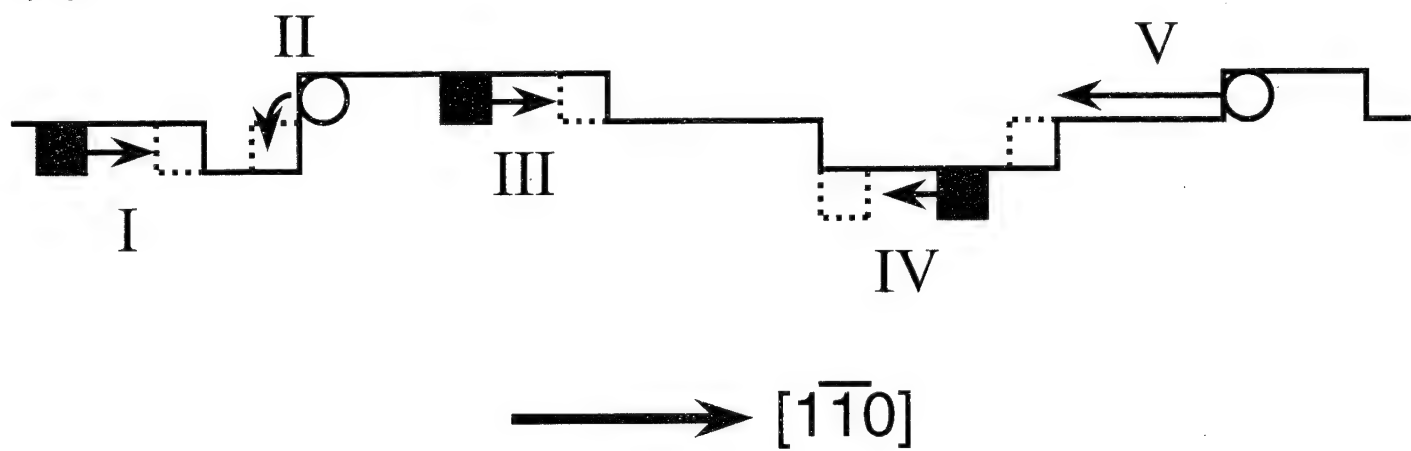


FIG. 5

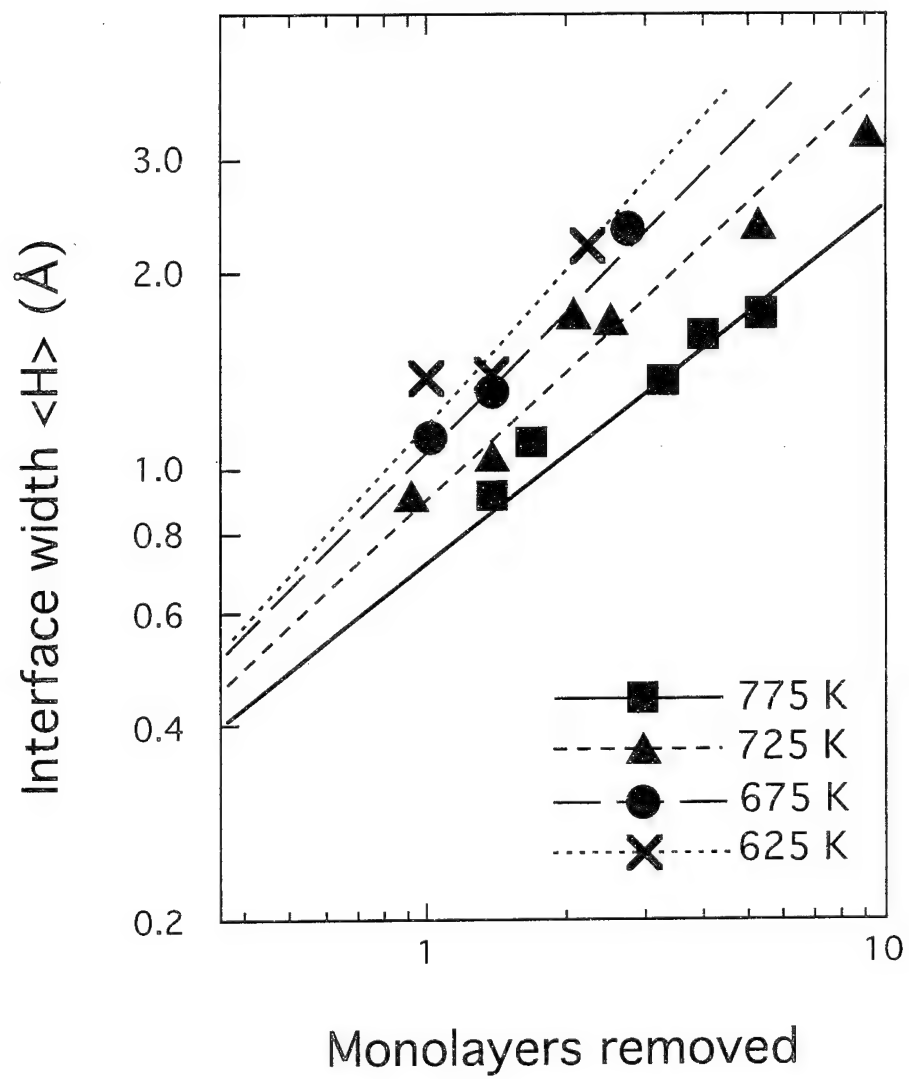


FIG. 6

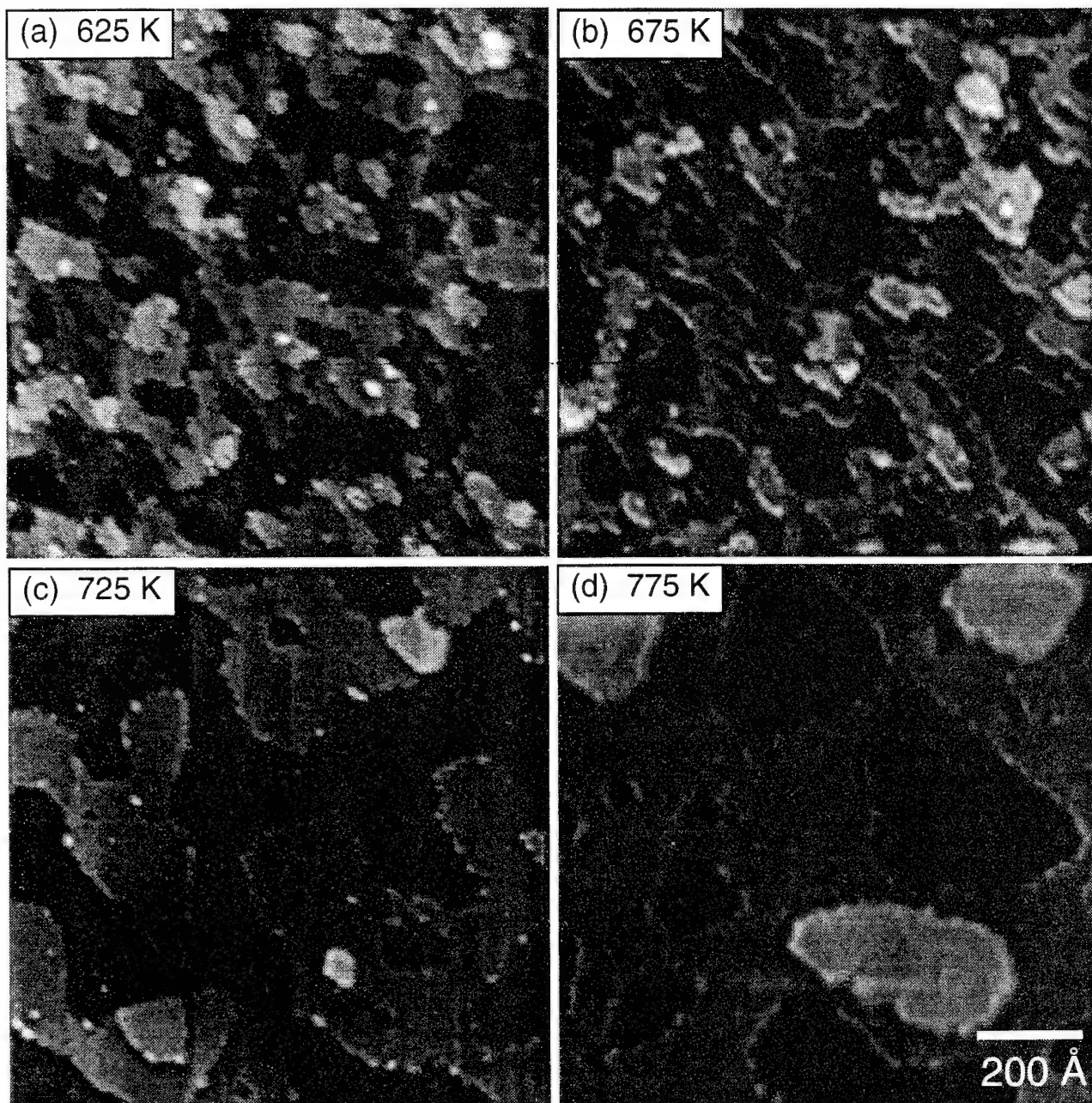


FIG. 7

Appendix 4

Preprint of "Ion Sputtering of GaAs(110):
From Individual Bombardment Events to Multilayer Removal"

X.-S. Wang, R.J. Pechman, and J.H. Weaver

To be published in J. Vac. Sci. Technol.

Ion sputtering of GaAs(110): from individual bombardment events to multilayer removal

X.-S. Wang, R.J. Pechman, and J.H. Weaver

Department of Materials Science and Chemical Engineering
University of Minnesota, Minneapolis, MN 55455

ABSTRACT

We have investigated the effects of ion mass (Ar^+ , Xe^+), energy (0.3 - 5 keV), trajectory and sample temperature on the ion sputtering processes for GaAs(110). Scanning tunneling microscopy images reveal that most ion bombardment events at 300 K create pits that are 1–5 unit cells in size, indicating that direct knock-on collisions dominate. The average pit size increases moderately with ion energy but shows a significant variation with the incident angle. Vacancies are sufficiently mobile at 625–775 K that vacancy islands form and the yield can be determined directly. The sputtering yields for these nearly ideal surfaces exhibit structure that can be related to the nuclear stopping power and ion channeling, showing the influence of such geometric factors as surface path-length, ion radius, and projected atom column density. Temperature dependent results for monolayer and multilayer sputtering show that adatoms ejected onto the surface refill vacancies but that the surface roughness, as measured by surface width, increases with ion fluence. While inter-layer atomic transport is measurable at 625 K and increases with temperature, it is not sufficient to achieve layer-by-layer removal because As_x desorption competes with interlayer transport above ~800 K.

PACS: 61.80.Jh 79.20.Rf 81.60.-j

INTRODUCTION

The interaction of energetic ions with solids has been studied for many reasons.¹⁻³ Ion implantation and sputtering are used to advantage in advanced materials processing and integrated circuit fabrication, but the defects generated by energetic ions also degrade semiconductor device performance. Ion-solid interactions are generally divided into nuclear and electronic contributions. The former denotes energy loss by collisions between ions and the core of target atoms while the latter involves losses due to electron-hole creation or excitations generated when ions travel in the electron media. This understanding of high energy collisions (≥ 100 keV) involving light ions is mature because nuclear and electronic contributions to the stopping power can be decoupled in theoretical formulations and the traces of high energy ions can be measured.³ However, an accurate description of ion-solid interactions is not available for massive ions such as Ar^+ and Xe^+ at low and medium energy (≤ 10 keV). In this case, the nuclear and electronic stopping powers depend on atomic and electronic structures of the target, and their effects are closely correlated.^{1,2} Moreover, the size of defects generated by low-energy ions is on the order of nanometers, and conventional probes cannot resolve such features. Finally, important quantities that describe bombardment processes, such as the average number of atoms removed by an impinging ion (the sputter yield), have normally been measured under conditions^{1,4,5} where surface disorder and contamination play an important role.

Recently, insights regarding low and medium energy ion-solid interactions have been made possible by using atomic resolution scanning tunneling microscopy (STM).⁶⁻¹² Indeed, STM can reveal details of ion bombardment related to vacancy and crater generation at the surface^{6-9,12} and sputtering yields can be measured for bombardment of crystalline surfaces.^{7,10} These results are relevant to advanced nanofabrication applications that use ion sputtering, plasma etching,¹³ ion-induced growth,^{14,15} and ion implantation.

We have used STM to study bombardment processes on GaAs(110) by measuring defect size distributions and sputtering yields for ions of different energy (0.3-5 keV), mass (40 amu for Ar, 131 amu for Xe), and incident direction. Our results show that the typical defect associated with a single event extends over 1-5 unit cells (the surface unit mesh corresponding to 1 Ga and 1 As

atom, spanning $4.00 \times 5.65 \text{ \AA}^2$) and that the average defect size increases slowly with ion energy. These collisions are confined to the direct knock-on and linear cascade regimes. The surface damage and sputtering yield can be reduced when channeling occurs. The measured data reveal the variations in the channeling probability as a function of ion energies, sizes and incident trajectories. Some of the characteristics of ion impact on crystalline GaAs surfaces are quite different from those found for amorphous and some metal surfaces, and those differences are discussed below.

The behavior of vacancies, adatoms, and other defects of crystal surfaces determines the evolution of the surface topology during ion sputtering, similar to etching^{16,17} and epitaxial growth. STM makes it possible to extract information that reflects surface dynamics and kinetics after sputtering and annealing.⁸⁻¹¹ Here, we discuss vacancy diffusion and interlayer mass transport following bombardment of GaAs(110) at $625 \leq T \leq 775 \text{ K}$ as a function of ion fluence.

EXPERIMENTAL

The experiments were performed in an ultrahigh vacuum chamber (base pressure $\leq 1 \times 10^{-10}$ Torr) equipped with STM and low-energy electron diffraction (LEED) capabilities. GaAs(110) surfaces were prepared by cleaving single crystals that were Zn doped at $\sim 2 \times 10^{18} \text{ cm}^{-3}$. Large ordered areas were produced routinely with vacancy densities below $5 \times 10^{11} \text{ cm}^{-2}$. The surfaces were bombarded at normal incidence, along [111] by tilting 35° to [001], and along [100] by tilting 45° to $[1\bar{1}0]$. Alignment of the ion beam with a crystal direction could be achieved within $\pm 3^\circ$. Heating was done with a filament behind the sample. The temperature was monitored with an optical pyrometer and a thermocouple. We estimate the absolute accuracy to be $\pm 20 \text{ K}$ (reproducibly $\pm 10 \text{ K}$) and note that this uncertainty is related to the fact that the samples are cleaved posts.

Beams of Ar^+ or Xe^+ were generated by a differentially-pumped ion gun that was thoroughly degassed before each exposure. High purity gases were used, and the chamber pressure was maintained below 1×10^{-8} Torr during bombardment. For most of the low fluence experiments, the pressure remained below 3×10^{-9} Torr. After sputtering, the gas inlet was turned off and the chamber pressure dropped below 1×10^{-9} Torr within a minute. We found no evidence of

significant contamination after ion exposures. The sputtered surfaces remained clean for ~3 days. Usually, for sputtering-yield measurement, a few iterations of sputtering-imaging were performed on samples after a cleave. The flux, corresponding to the current from sample-to-ground, was typically 10^{10} to 10^{11} $\text{cm}^{-2} \text{s}^{-1}$, at least two orders of magnitude lower than used in traditional sputtering studies.^{4,5,18} The presence of an unstable parasitic leakage current to the sample caused an uncertainty of $\pm 15\%$ in ion flux readings, especially during bombardment above ~650 K.

STM images were acquired in the constant current mode at room temperature. The electrochemically-etched tungsten tips were cleaned *in situ* by e-beam bombardment. Typically, the sample bias was - 2-3 V and the tunneling current was 0.05 to 0.5 nA. Positive bias and dual-bias images were also acquired. Different areas were scanned for each surface to obtain statistically-representative images. In addition, measurements at each sputtering condition (energy, mass, incident direction) were done at least three times. Care was taken to exclude the effects of pre-existing disorder and steps, especially in sputtering yield measurements where we only used images taken at least 1000 Å from pre-existing steps.

RESULTS AND DISCUSSION

1. Defect analysis

Figure 1(a) is an STM image taken to display As atoms on pristine GaAs(110). These atoms form a two-dimensional rectangular lattice with atomic spacings of 4.00 Å along $[1\bar{1}0]$ and 5.65 Å along $[001]$. Ga-sublattice images can be obtained with positive sample bias.¹⁹ Figures 1(b), (c) and (d) show the effects of bombardment at 300 K at normal incidence with 300 eV Ar^+ , 3 keV Ar^+ , and 5 keV Xe^+ , respectively. Pits (P) of one or a few missing atoms, adatoms (A) ejected onto the surface, and disordered regions (D) are evident in Fig. 1(b).

The pit size is an important measure of ion-surface interactions. As shown in Fig. 1(b), the lateral dimension of most pits generated by 300 eV Ar^+ ions at normal incidence was 1-5 unit cells. Pit size distribution was statistically measured over an surface area containing more than 1000 pits, and the sputtering and pit-counting were repeated a few times on freshly-cleaved samples. The data indicate that nearly half of them are 2 unit cells in size with 85% falling in the range 1-3 unit

cells.²⁰ Overall, the average pit size is 2.1 unit cells. When the Ar⁺ ion energy was increased tenfold, the average defect size increased 50% to 3.1 unit cells. This increase is somewhat deceptive because the average is skewed after 3 - 5 keV bombardment by pits extending over at least 10 unit cells. For example, arrows in Fig. 1(c) and (d) identify pits involving more than 20 unit cells in lateral dimension, with an unknown depth. Clearly, high energy ions are capable of inducing extensive damage, despite the limited effect of ion energy on average pit size and the observation that most high energy ions do not displace many surface atoms at normal incidence. It should be pointed out that, with the ion fluences used in Fig. 1, the average area per ion is $\geq 3.7 \times 10^3 \text{ \AA}^2$, or 160 surface unit cells. The probability for two impact events occurring within a distance of 5 unit-cells is $\leq 10\%$, and the probability for three or more impacts within 5 unit-cells is $\leq 0.5\%$. Therefore, some ($\leq 10\%$) of the pits seen in Fig. 1, especially the large ones, may be created by two ion impact events. The average pit sizes for single impact could be 10% lower than the values presented here.

The effect of ion momentum was investigated by replacing $^{18}\text{Ar}^+$ (40 amu) with $^{54}\text{Xe}^+$ (131 amu), increasing the momentum by a factor of 1.8 for the same energy. The increase of radius from 1.54 Å for Ar⁺ to 1.91 Å for Xe⁺ also enlarged the interaction cross-section. Analysis of the images showed, however, that the average defect size created by 3 keV Xe⁺ was 3.0 unit cells, essentially the same as for Ar⁺. An increase in energy from 3 keV to 5 keV for Xe⁺ increased the average pit size to 3.8 unit cells at normal incidence. As we will show below, the normal incidence sputtering yields for Ar⁺ and Xe⁺ are nearly equal at 3 keV, and the yields change slowly with ion energy from 1 keV to 5 keV.

The effect of ion trajectory was investigated by orienting the beam along [100] and [111], in addition to [110]. Figures 2(a) and (b) represent surfaces bombarded with 500 eV Xe⁺ along [100] and 3 keV Xe⁺ along [111], respectively. Comparing Fig. 2(b) with Fig. 1(c) reveals that impact along [111] generates a greater number of large defects. The average pit size is 4.6 unit cells for 3 keV Xe⁺ incident along [111], about 50% bigger than at normal incidence. Even 500 eV Xe⁺ ions directed along [100] create average pits of 3.7 unit cells. This reflects a notable increase of ion interactions with surface and near surface atoms. In addition to a longer ion path near the

surface for off-normal incidence, the increased interaction can be attributed to a higher probability of close ion-atom encounter along [111] and [100], as discussed in detail in Sect. 3.

2. Sputtering yield

Traditional measurements^{4,5} of the sputtering yield usually involve the removal of hundreds of atomic layers with beam intensities exceeding 10^{14} ions-cm⁻²-s⁻¹. As a result, undesirable effects such as surface amorphization, the formation of non-ideal bonding configurations, and thermal desorption influence the results. An alternate way to determine the yield involves using the STM to measure surface vacancy islands produced by ion impact.¹⁰ This requires that sputtering be done under conditions where atoms displaced onto the surface and vacancies produced in the surface are mobile. These conditions are met for GaAs(110) for temperatures above 625 K because the adatoms tend to refill vacancies and vacancy coalescence leads to single layer deep vacancy islands.²⁰

Images acquired on surfaces bombarded at 625-775 K indicate that the stoichiometry of GaAs was preserved. In particular, we have found no evidence of areas where the structure was modified because of a surplus of one species, even after the removal of 10 ML. Figure 3(a) displays a $500 \text{ \AA} \times 500 \text{ \AA}$ area sputtered with normal-incident Ar⁺ at 725 K (3 keV, fluence $1.6 \times 10^{14} \text{ cm}^{-2}$, flux $9 \times 10^{10} \text{ cm}^{-2}\text{s}^{-1}$). Inspection shows that adatoms and small vacancy complexes are replaced by vacancy islands that are one monolayer deep and that the top and exposed layers are well ordered. Images like those of Fig. 3(a) have been obtained following sputtering with Ar⁺ and Xe⁺ at energies between 300 eV and 5 keV, for $625 \leq T \leq 775 \text{ K}$, and for different trajectories. Details on the initial stages of vacancy island nucleation will be shown later (e.g. Fig. 7). Note that the vacancy islands did not increase in area after further annealing at 625-775 K, implying negligible evaporation and easy percolation of sub-surface vacancies to surface. Although we cannot exclude the possibility that adatoms ejected onto the surface by ion impact could be lost via subsequent ion impact or by thermally activated desorption (they are bound less strongly than normal surface atoms), we could expect that the yield would show temperature-, flux- and fluence-dependencies if these effects were significant.¹ No such variations were observed for material

removal between 0.1 and 10 ML. Likewise, surface disorder produced by ion bombardment or thermal excitation would affect the ion-surface interaction cross-section, but we found no indication that the effects were important in our low-flux measurements. Together, these results indicate the importance of defect annealing and adatom-vacancy recombination as well as negligible thermal disordering and desorption during sputtering. Accordingly, we calculate the sputtering yield at the sub-monolayer level from the area of the vacancy islands while crystal order is maintained.

The preservation of stoichiometry is reasonable because surface order is maintained under the conditions of ion flux and temperature in our experiment. Though mechanical collisions favor sputtering of lighter atoms and/or weakly-bound species, the Ga and As atoms are bound in equal strength on ordered GaAs(110) and their mass difference is small.^{1,21} The present results thus differ from those in the literature where preferential As loss was reported for bombardment of GaAs with high intensity beams ($\geq 10^{14}$ ions-cm²-s⁻¹) at room temperature.¹⁸ Under such sputtering conditions, surface order was destroyed, volatile molecules such as As₂ and As₄ could form, and the ion beam could stimulate their desorption. This contrast demonstrates the advantage of using low ion flux and fluence in STM measurement to maintain surface order so that the results reveal the nature of ideal ion-crystal impact. Preservation of stoichiometry has also been observed on Ar-sputtered InSb(110) by Cvetko *et al.*²² when crystalline order was maintained during bombardment. However, we observed surface deterioration ~ 800 K because of As_x evaporation. Figure 3(b) displays an area of such an As-depleted surface. Disordered clusters and islands, which are induced by excessive gallium, are easily observed, especially near step-edges. Such features have not been observed on samples sputtered at ≤ 775 K.

Figure 4 summarizes the yield data, Y , for trajectories along [110], [111], and [100] with lines that act as guides to the eye. Since our ion beam intensity decreases rapidly at low energy, we were not able to measure the behavior below ~ 300 eV. Errors of the data were mainly induced by a fluctuation leakage current in ion flux measurement. These were about 10% of the ion current for relatively high energies and more at 300 - 500 eV due to the beam intensity decrease. All of the fitting curves start at (0, 0) since there is no sputtering at $E=0$. The purpose of these curves is to

display the dependence of yield on the energy, mass and incident geometry. Although the fitting has uncertainty, the trends we intend to show are beyond the margin of error. From Fig. 4(a), the normal incidence yield for Ar^+ is about 1.3 atoms/ion between 300 and 5000 eV with a maximum at ~ 1100 eV. For Xe^+ , the yield increases from ~ 1 at 1 keV to 1.7 at 5 keV, crossing the curve for Ar^+ at ~ 3 keV. Overall, the absolute difference between the yields for Ar^+ and Xe^+ is below 50% for [110] incidence. For [111] and [100] incidence, however, the differences are more pronounced. From Figs. 4(b) and (c), the sputtering yields for Ar^+ peak at ~ 1.1 and ~ 1.3 keV and then fall off more sharply than for [110]. For Xe^+ , on the other hand, data points show a slight drop in the measured yield near 2 keV [Figs. 4(b) and (c)], but this decrease is probably an expanded artifact and a consequence of large error at low E_{ion} . Consequently, while the yields are quite close near 1 keV, Xe^+ bombardment removes nearly three times as many atoms at 5 keV.

From Fig. 4, we see that $Y_{[110]} < Y_{[111]} < Y_{[100]}$ for each ion type over almost the entire energy range. This can be rationalized using simple geometric arguments. First, at off-normal incidence, more ion-target interactions take place near the surface and target atoms are more likely to gain momentum in the normal direction. The crystal structure of GaAs provides the second reason. Figure 5 shows the atomic positions projected in the [110], [111], and [100] directions, where each atom represents a column of atoms. The lowest density of columns, 0.177 \AA^{-2} , is encountered for ions moving along [110], while the density is 0.216 \AA^{-2} for [111], and even higher at the [100] pole, 0.25 \AA^{-2} . In addition, the distribution of atom columns in the [110] projection opens up particularly large channels. For normal incidence, these factors increase the probability of channeling and reduce the cross-section of ion-surface interaction.

Sputtering yields have been measured for many ion-target combinations under high flux conditions.^{1,23} Results from targets with fcc and diamond structures have shown the lowest yield and the weakest energy dependence for [110] incidence. For Si and Ge, the relative order of yields for the three incident directions was the same as what we found for GaAs, reflecting the common crystal structures. However, stronger dependences on ion energy and mass were observed in the traditional studies, especially for [111] and [100], because the yield showed a maximum and this peak energy increased with ion mass. For Ar^+ the peak energy was above 5 keV, much higher than

we find. Similar measurements⁴ found that the peak position for amorphous and polycrystalline targets was at tens of keV, much higher than for single crystals, and the yield increased rapidly with ion energy for $E_{ion} \leq 5$ keV. Thus, structural disorder seems to increase the peak energy and to broaden it.

3. Ion-surface interaction mechanism

Ions interact with solids through hard core collisions (nuclear stopping) and electronic excitations (electronic stopping). Hard core collisions are closely related to the atomic configuration, energy, mass, and size of the particles involved. They are avoided when ions travel in the open channels but they cause damage when the impact parameter is small enough. For incident energy below ~ 1 keV, the energy transfer is relatively low and the defects created involve only a few atoms (direct knock-on regime). With increasing energy, the struck atoms displace other atoms (linear cascade regime). At even higher energy, many collision cascades occur along the ion trajectory and almost all atoms near the ion are set in violent motion (thermal spike regime). The pit size and sputtering yield measured here reflect the ion-surface interaction in that more energetic ions are able to create larger pits and eject more atoms. However, if they channel through distances of a few nanometers before the first collision, then damage will be well beneath the surface and sputtering will be less likely.

It is instructive to compare our results for GaAs(110) to those for other semiconductors and for Pt and Au. The small pits on GaAs(110) seen in Figs. 1 and 2 probably reflect direct knock-on collisions while those larger than about 10 unit cells were generated by linear cascade events. For GaAs(110), the average pit size increased slowly with ion energy. On other semiconductor surfaces, including Si(100), Si(111), and GaAs(100), typical defects created by medium energy ions are also limited to a few unit cells.^{9,12} From Fig. 4, the yield for Xe⁺ at normal incidence on GaAs(110) increased only 75% from 300 to 5000 eV and even less for [111] and [100] trajectories. Remarkably, the yield for 5 keV Ar⁺ was below the value for 300 eV Ar⁺. In contrast, Lang *et al.*⁷ observed a much larger size difference in defects created by 600 eV and 3 keV Ne⁺ incident on Au(111). Michely *et al.*⁶ related craters formed on Pt(111) after 5-keV Xe⁺

bombardment to thermal spikes. Such thermal spike events are associated with the effusion of hundreds of atoms onto the surface as a result of local melting.²⁴ For Au(111),⁷ the yield increased from 1 to 4 for Ne⁺ between 600 eV and 3 keV. On Pt(111),^{6,10} the yield increased from 0.58 at 200 eV to 7.4 at 5 keV for Ar⁺ and 1.0 to 14.5 over the same range for Xe⁺.

Part of these different responses can be attributed to the probability of close encounters near enough to the surface that damage can be observed with STM. Clearly, the higher the projected atom (or atomic column) density, the greater the probability of a near-surface collision, and hence, the larger the defect size and sputtering yield. For Pt and Au, the atomic density is nearly 50% higher than for GaAs. Viewed along [111], the Au and Pt atom positions are similar to those in Fig. 5(b) but the density of columns is about 0.286 Å⁻² instead of 0.216 Å⁻². Furthermore, the ion cores of Pt and Au are larger than Ga and As.

Beyond simple structural differences, it is important to recognize that the cohesive energies of these materials are roughly comparable, with the semiconductors falling between Au and Pt, but that the number of neighbors is 4 for the semiconductors and 12 for the metals. As a result, it is far easier to introduce disorder in metals than in the covalently bonded semiconductors and the energies associated with atom diffusion are much lower for metals. The absence of large craters for GaAs(110) after bombardment by ions of energies sufficient to induce spike events reflects the lattice response more than the absence of small impact parameter events. The effusion of atoms onto the surface following impact can be described by interatomic potentials that reflect the activation energy for such motion. The fact that the activation energy for diffusion for Pt adatoms on Pt(111)²⁵ is much smaller than that for Si on Si²⁶ and Ga or As on GaAs should be reflected in the higher structural integrity of the semiconductors.

From Fig. 4, the energy dependence of the sputtering yield is relatively weak near 5 keV. Quantitative analysis of the yields for 5 keV-Ar⁺ incidence along the three trajectories shows that they were proportional to the product of the projected atom-column density and $(\cos \theta)^{-1}$, the surface sensitivity factor, where θ is the angle of incidence relative to the surface normal. This scaling relation demonstrates that hard-core collisions dominate sputtering at high energy. To emphasize the dependence on trajectory at low energy, we rescaled the off-normal yield data to that

for normal incidence, [110], using the ratio of the yields at 5 keV, as shown in Figs. 6(a) and (b). These results can be compared to what would be expected based on nuclear stopping. To determine the latter, we calculated the linear rate of ion energy loss, dE/dx , according to Thomas-Fermi screening theory for hard-core collisions,³ and plotted this nuclear stopping power in Fig. 6. In the theory, the target is treated as an amorphous solid. In the energy range of interest here, the stopping power varies with ion energy roughly as E^α where $\alpha = 0.46$ for Ar^+ and 0.50 for Xe^+ .

From Fig. 6, it is apparent that the calculated energy dependence of the stopping power is quite different from the measured sputtering yields. The difference is particularly dramatic for Ar^+ . We propose that the discrepancy arises from channeling, an effect ignored in the theory, and that channeling effectively reduces ion-surface interaction at high energy due to increased ion speed. Thus, the yield increases with the stopping power at low energy but declines as channeling becomes more probable at higher energy. Since the importance of channeling should depend on the atom-column density, the yield peak for [100] should be shifted to higher energy than [111] and it should be broadened. At high energy, our data show that the yield depends on atom-column density and path length near surface, while energy change has little effect. This emphasizes the two-dimensional atom density, instead of the three-dimensional atom density used in conventional theory.³ The latter does not take the lattice ordering into account. For the [110] trajectory, because of the open profile, the channeling effect starts to dominate at even lower energy where the yield determined by nuclear stopping nearly equals the high energy limit. Hence, the relationship of yield to ion energy does not show a pronounced peak.

Channeling should be less probable for Xe^+ than Ar^+ and the importance of incident angle should be reduced because Xe^+ is larger than Ar^+ and its velocity is less than that of Ar^+ at the same energy. Indeed, Fig. 6(b) shows that the energy dependence of the yield is more nearly like the energy dependence of the nuclear stopping power, without a pronounced peak at low kinetic energy. Similarly, on more compact metal surfaces such as $\text{Pt}(111)$ and $\text{Au}(111)$, this energy-dependent channeling effect should be weak. Finally, it should be emphasized that structural disorder can change the sputtering behavior enormously because channeling is compromised. This is obvious on amorphous semiconductor surfaces^{4,5} where the sputtering yields peak at much

higher ion energies than those of Fig. 4, in good agreement with the conventional theory.

4. Vacancy diffusion and surface roughness

Figure 7 displays STM images of surfaces sputtered at 625 - 775 K with about 0.05 ML removed using Ar^+ at 300-500 eV. At these temperatures, there is activated diffusion of the vacancies and adatoms. In Fig. 7(a), there are very few adatoms compared to Fig. 1 where such features were immobile. Moreover, disordered patches are hard to find, and vacancy islands have formed. From Fig. 7(b), the number of small vacancy islands (1-2 unit cells) has decreased significantly compared to 625 K. This indicates that such structures can diffuse on the surface and combine with others. Images obtained after sputtering at 725 K showed that pits smaller than 5 unit cells were rare and that vacancy islands were adjusting their shapes according to the crystal symmetry with edges aligned preferentially along $[1\bar{1}0]$. At 775 K, the islands were even larger and better defined. The exposed layers were also ordered. Thermal desorption was significant only above ~ 800 K where surface deterioration due to As_x sublimation was observed.

The formation of large vacancy islands from individual vacancies is similar to the nucleation and growth of islands from deposited atoms. At temperatures too low for the system to achieve thermodynamic equilibrium, the growth processes are governed by kinetic factors like the deposition rate, the particle diffusivity, and the stability of islands of various sizes.²⁷ In our experiment, the vacancy creation rate is low enough that it can be disregarded. Employing the method of Mo *et al.*²⁶ for measuring diffusion parameters of Si on Si(100), we evaluated the activation energy of vacancy diffusion on GaAs(110).²⁰ This was based on measuring the vacancy island densities for $625 \leq T \leq 775$ K after removal of ≤ 0.05 ML. The activation energy was 1.3 ± 0.2 eV, as discussed in detail elsewhere.²⁰ In addition, analysis shows that thermally activated diffusion of GaAs vacancy pairs occurs along the zig-zag rows, $[1\bar{1}0]$. These pairs were easily accommodated by a vacancy island at both $[001]$ and $[1\bar{1}0]$ edges, making the islands grow isotropically.

Vacancy islands on sputtered surfaces at low fluence are mainly 1 ML in depth for sputtering below ~ 725 K, in contrast to halogen etching of GaAs(110) where only double layer vacancy

islands are observed.¹⁶ For sputtering above ~725 K, however, we do see the formation of double-layer vacancy islands. These double-layer steps appear more stable against erosion than single-layer steps. The effect of increased ion fluence is to produce erosion of deeper layers. Figure 8 shows representative images of surfaces after removal of about 2.5 ML at $625 \leq T \leq 775$ K. Again, the surface morphology is determined by kinetic processes, namely generation, diffusion, recombination, and nucleation of vacancies and adatoms. The STM images show that the surfaces become rougher as more layers are exposed and that the roughness is temperature dependent. As for low fluence results, double-layer vacancy islands are evident above ~725 K.

Since ion sputtering is a localized process that occurs randomly on the surface, there will be material removed from exposed areas of vacancy islands and this will become increasingly important as the island grows. On the other hand, if damage to the newly-exposed layer can be healed by atoms from the outer layer, then erosion of the inner layer would be postponed until the outer layer is consumed (layer-by-layer sputtering). For GaAs(110), the experimental results demonstrate that the transfer of atoms from the outer layer is not sufficient to annihilate inner layer vacancies completely so that vacancy islands at different levels grow simultaneously. Figure 8 shows that six layers of the surface were exposed at 625 K. The amount of removal from each layer is shown quantitatively beneath the STM topograph via a plot of θ_i , the coverage, for layers $i = 1-6$. At 625 K, remnants of first and second layers persisted while the fourth and fifth layers showed significant erosion. At 625 K, the step edges were rough, indicating difficulty of both intralayer and interlayer diffusion. At 675 K, the surface layer was almost entirely removed ($\theta_1 = 0.002$) but the 6th layer was not yet eroded ($\theta_6 = 1$). At 675 K, the step edges were smoother, easier to identify, and there was a tendency to show alignment along $[1\bar{1}0]$. Surface smoothness improved further at 725 and 775 K, as shown by the images and analysis thereof.

A quantitative measure of the surface roughness is the surface width²⁸ that is defined as $H = [\langle h^2(x) \rangle - \langle h \rangle^2]^{1/2}$, where $h(x)$ is the surface height at location x and $\langle \rangle$ denotes averaging over the surface. H in monolayer units is related to layer coverage θ_i by $H^2 = \sum (\theta_i - \theta_{i-1})^2 - [\sum (\theta_i - \theta_{i-1})]^2$. This equation can be derived by simply considering a unit area with layer coverage given by θ_i and setting the height of the first layer to zero. A general derivation is in the Appendix.

The surface width was calculated for each surface and is given below each image in Fig. 8. Those numbers show a remarkable decrease in the width between 625 K and 725 K, in agreement with visual perception of the STM images. We note that the value of H is larger for the surface sputtered at 775 K than for 725 K. This reflects the greater probability of forming double-layer vacancy islands at 775 K. Finally, for comparison we show as dashed lines in Fig. 8(a) the predicted layer-by-layer coverage θ_i for a system where there is no interlayer exchange after 2.5 ML removed.²⁹ This model profile is superimposed on the experimental profile at 625 K because interlayer exchange should be minimized at low temperature. The model surface appears rougher than that measured at 625 K because more outer-layers remain and more deeper-layers were removed. For this model surface, $H = 1.58$ ML.

The surface widths have been measured on samples after sputtering with different amounts of material removed, as summarized in Fig. 9. In general, the increase in surface width scales with the amount of material removal, τ , as $H \sim \tau^\beta$ where τ is measured in monolayer-equivalents. Physically, the scaling exponent is a measure of the effectiveness of interlayer transport.²⁸ If there is no such transport, then $\beta = 0.5$. For layer-by-layer sputtering, $\beta = 0$. The solid lines represent fits to the data obtained after sputtering at 625 K and 775 K. The behavior expected for completely-hindered interlayer transport, $\beta = 0.5$, is also shown. The values of β demonstrate that interlayer atom transport does occur at 625 K but that such transport is not enough to achieve layer-by-layer removal, even at 775 K.

There are several possible processes by which atom transfer can occur on sputtered GaAs(110) to minimize roughness. First, adatoms produced during sputtering of the top layer can jump to a lower terrace to annihilate vacancies in that layer. The step between terraces usually acts as a special barrier (Schwoebel barrier³⁰) to such atom motion. This barrier originates from the reduced coordination of an atom on the upper terrace near a step. From the images, there were no adatoms on surfaces during the early stages of sputtering (≤ 0.5 ML removed) for $T \geq 625$ K. This indicates that they were able to step down, suggesting that the Schwoebel barrier is not very effective. A further reduction in the effectiveness of the barrier might be expected because the adatoms that are ejected onto the surface initially have energies in excess of thermal species.

Moreover, since the ejected atoms do not form stable islands that would reduce their surface diffusivity, the attempt rate to overcome the step-down barrier is enhanced. Second, atoms can detach from step edges and combine with sub-layer vacancies. Since extended annealing of a sample sputtered at 775 K did not induce major change in surface morphology, we conclude that this is not an important process. Third, lower-layer sputtering can eject adatoms to upper layers, forming a reverse transfer. This can always occur when several layers are exposed.

CONCLUSIONS

Analysis of STM images for GaAs(110) after various ion bombardment processes shows that low- and medium-energy ions create surface defects mainly by direct knock-on and linear cascade collisions, resulting in pits typically of 1-5 unit cells. The average pit size and sputtering yield change slowly with ion energy when compared to the bombardment of some metals, but they are quite sensitive to the trajectory of the incident beam. Hence, the efficiency of energy transfer from ions to near surface atoms reflects the detailed interaction inherent in channeling. During sputtering at $625 \leq T \leq 775$ K, we see that vacancy diffusion leads to the formation of large vacancy islands but surface roughening occurs during extended sputtering. While interlayer atom transport reduces surface roughness at 625 K, layer-by-layer sputtering cannot be realized due to reverse transfer of adatoms and the inherent thermal instability of the surface.

ACKNOWLEDGMENTS

This work was supported by the Army Research Office and the National Science Foundation. We thank D. Rioux, P.J. Benning, C.Y. Cha and D.W. Owens for helpful discussions.

APPENDIX

If a surface of overall area S has a layer coverage θ_i ($\theta_0 = 0$) and there is no overhang, then an area of $S\theta_1$ would have a height h_1 , $S(\theta_2 - \theta_1)$ of height h_2 , ..., $S(\theta_i - \theta_{i-1})$ of height h_i , and so forth. If we set $h_1 = 1$ and the monolayer thickness $h_i - h_{i-1} = 1$, then $h_i = i$, and

$$\begin{aligned} H^2 &\equiv \langle h^2(x) \rangle - \langle h \rangle^2 \\ &= [\sum S(\theta_i - \theta_{i-1})i^2]/S - \{[\sum S(\theta_i - \theta_{i-1})i]/S\}^2 \\ &= \sum (\theta_i - \theta_{i-1})i^2 - [\sum (\theta_i - \theta_{i-1})i]^2 \end{aligned}$$

The unit of H is the monolayer thickness, or simply monolayer (ML). The summation is from $i = 1$ to ∞ , but for the minimum n where $\theta_n = 1$, $\theta_{n+1} - \theta_n = 0$, the summation ends at $i = n$.

REFERENCES

1. *Sputtering by Particle Bombardment I*, edited by R. Behrisch (Springer, Berlin, 1981).
2. N. Winograd and B.J. Garrison, in *Ion Spectroscopies for Surface Analysis*, edited by A.W. Czanderna and D.M. Hercules (Plenum, New York, 1991), p. 45.
3. G. Carter and W.A. Grant, *Ion Implantation of Semiconductors* (Edward Arnold, London, 1976); J.F. Ziegler, in *Handbook of Ion Implantation Technology*, edited by J.F. Ziegler (Elsevier, Amsterdam, 1992).
4. P.C. Zalm, J. Appl. Phys. **54**, 2660 (1983).
5. S. Tachi and S. Okudaira, J. Vac. Sci. Technol. B **4**, 459 (1986).
6. T. Michely, K.H. Besocke, and G. Comsa, Surf. Sci. **230**, L135 (1990); C. Teichert, M. Hohage, T. Michely, and G. Comsa, Phys. Rev. Lett. **72**, 1682 (1994).
7. C.A. Lang, C.F. Quate, and J. Nogami, Appl. Phys. Lett. **59**, 1696 (1991).
8. P. Bedrossian and T. Klitsner, Phys. Rev. B **44**, 13783 (1991); P. Bedrossian, Surf. Sci. **301**, 223 (1994).
9. H. Feil, H.J.W. Zandvliet, M.-H. Tsai, J.D. Dow, and I.S.T. Tsong, Phys. Rev. Lett. **69**, 3076 (1992); H.J.W. Zandvliet, H.B. Elswijk, E.J. van Loenen, and I.S.T. Tsong, Phys. Rev. B **46**, 7581 (1992).
10. T. Michely and G. Comsa, Nucl. Instrum. Meth. Phys. Res. B **82**, 207 (1993); T. Michely and C. Teichert, Phys. Rev. B **50**, 11156 (1994).
11. J.C. Girard, Y. Samson, S. Gauthier, S. Rousset, and J. Klein, Surf. Sci. **302**, 73 (1994).
12. S. Ohkouchi, N. Ikoma, and I. Tanaka, J. Vac. Sci. Technol. B **12**, 2030 (1994).
13. J.W. Coburn, J. Vac. Sci. Technol. A **12**, 1417 (1994), and references therein.
14. C.-H. Choi, R. Ai, and S.A. Barnett, Phys. Rev. Lett. **67**, 2826 (1991).
15. G. Rosenfeld, R. Servaty, C. Teichert, B. Poelsema, and G. Comsa, Phys. Rev. Lett. **71**, 895 (1993); J.A. Meyer and R.J. Behm, Phys. Rev. Lett. **73**, 364 (1994).
16. J.C. Patrin and J.H. Weaver, Phys. Rev. B **48**, 17913 (1993).
17. D. Rioux, R.J. Pechman, M. Chander, and J.H. Weaver, Phys. Rev. B **50**, 4430 (1994).
18. See, for example, Y.-X. Wang and P.H. Holloway, J. Vac. Sci. Technol. B **2**, 613 (1984);

- J.B. Malherbe, W.O. Barnard, I. Le R. Strydom, and C.W. Louw, *Surf. Interface Anal.* **18**, 491 (1992); J.H. Weaver, "Formation and Properties of Metal-Semiconductor Interfaces," in *Electronic Materials*, edited by J.R. Chelikowsky and A. Franciosi, Springer Tracts in Solid Sciences, Vol. 95 (Springer Verlag, Berlin, 1991) pp. 135-214.
19. R.M. Feenstra, J.A. Stroscio, J. Tersoff, and A.P. Fein, *Phys. Rev. Lett.* **58**, 1192 (1987).
 20. R.J. Pechman, X.-S. Wang, and J.H. Weaver, *Phys. Rev. B* (to be published).
 21. J.B. Malherbe and W.O. Barnard, *Surf. Sci.* **255**, 309 (1991).
 22. D. Cvetko, L. Floreano, A. Morgante, M. Peloi, and F. Tommasini, *Surf. Sci.* **307**, 519 (1994).
 23. P.C. Zalm, *Surf. Interface Anal.* **11**, 1 (1988).
 24. M. Ghaly and R.S. Averback, *Phys. Rev. Lett.* **72**, 364 (1994).
 25. D.W. Bassett and P.R. Webber, *Surf. Sci.* **70**, 520 (1978); S. Liu, Z. Zhang, G. Comsa, and H. Metiu, *Phys. Rev. Lett.* **71**, 2967 (1993).
 26. Y.W. Mo, J. Kleiner, M.B. Webb, and M.G. Lagally, *Phys. Rev. Lett.* **66**, 1998 (1991).
 27. J.A. Venables, G.D.T. Spiller, and M. Hanbucken, *Rep. Prog. Phys.* **47**, 399 (1984), and references therein.
 28. Z.Y. Zhang, J. Detch, and H. Metiu, *Phys. Rev. B* **48**, 4972 (1993).
 29. If the atoms are removed randomly from the exposed area and there is no transfer between different layers, then the coverage of the n th layer after the removal of the equivalent of τ layers is $\theta_n = [1 + \tau + \tau^2/2 + \dots + \tau^i/i! + \dots + \tau^{n-1}/(n-1)!] \exp(-\tau)$.
 30. R.L. Schwoebel, *J. Appl. Phys.* **40**, 614 (1969).

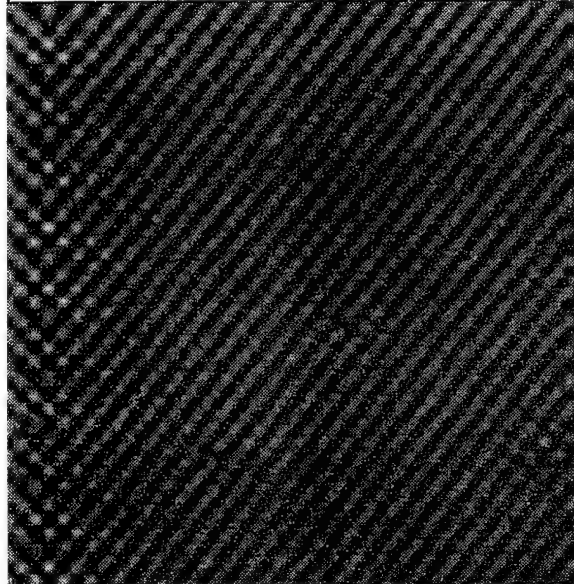
FIGURE CAPTIONS

- FIG. 1** Occupied states STM images of GaAs(110) before and after normal incidence ion bombardment at 300 K. All images are about $200 \times 200 \text{ \AA}^2$. $[1\bar{1}0]$ points from lower left to upper right and $[001]$ points from upper left to lower right. Examples of pits, adatoms and disordered patches are denoted in (b) as P, A and D, respectively. Arrows in (c) and (d) point to defects that extend over at least 20 unit cells where a unit cell corresponds to $4 \times 5.65 \text{ \AA}^2$.
- FIG. 2** STM images of GaAs(110) after low-fluence Xe^+ bombardment at room temperature with the beam directed along $[100]$ and $[111]$ incidence in (a) and (b), respectively. Images are $200 \times 200 \text{ \AA}^2$.
- FIG. 3** (a) A $500 \times 500 \text{ \AA}^2$ area of GaAs(110) after exposure to normal-incident 3 keV Ar^+ at 725 K (fluence $1.6 \times 10^{14} \text{ cm}^{-2}$). The dark areas are vacancy islands that are 1 ML deep. The areas exposed in the islands are ordered. (b) A $500 \times 500 \text{ \AA}^2$ area of GaAs(110) after sputtering at $\sim 800 \text{ K}$ showing surface disorder associated with significant As desorption. Further As-loss makes it difficult to image the surface with STM.
- FIG. 4** Plots of sputtering yield as a function of ion energy for GaAs(110) for Ar^+ and Xe^+ beams directed along (a) $[110]$; (b) $[111]$; and (c) $[100]$. The lines connecting the data points serve as guides to the eye.
- FIG. 5** Top view of the (a) (110), (b) (111) and (c) (100) surfaces of GaAs. Each atom represents an atomic row aligned along the surface normal direction.
- FIG. 6** Sputtering yields for beams directed along $[111]$ and $[100]$ scaled to coincide with the yields for $[110]$ measured at 5 keV for (a) Ar^+ and (b) Xe^+ . The scaling corresponds closely to the difference in atom density and path length. The solid line is the calculated nuclear stopping power, dE/dx , for Ar^+ and Xe^+ , assuming Thomas-Fermi screening (Ref. 3).
- FIG. 7** STM images acquired after removal of about 0.05 ML at 625-775 K. Images are about $375 \times 375 \text{ \AA}^2$.

FIG. 8 STM images acquired after removal of ~ 2.5 ML at 625-775 K. Image are about $630 \times 630 \text{ \AA}^2$. The corresponding layer-specific coverages are plotted below with solid lines. The surface width, H , was evaluated from the coverage data. The coverage profile for a model surface without interlayer atomic exchange is plotted in (a) with dashed lines and the corresponding value of H is 1.54 ML. Double-layer vacancy islands are denoted as D in (c) and (d).

FIG. 9 Surface width H as a function of amount of material removed τ (in monolayer-equivalents) at 625 K and 775 K. The solid lines correspond to fits using the scaling relationship $H \sim \tau^\beta$ and the value of β is given for each case. The scaling relationship for a model surface with no interlayer atom diffusion is plotted with a dashed line corresponding to $\beta = 0.5$.

(a) Before ion bombardment



(b) 300 eV Ar⁺; 2.7×10^{12} ions/cm²

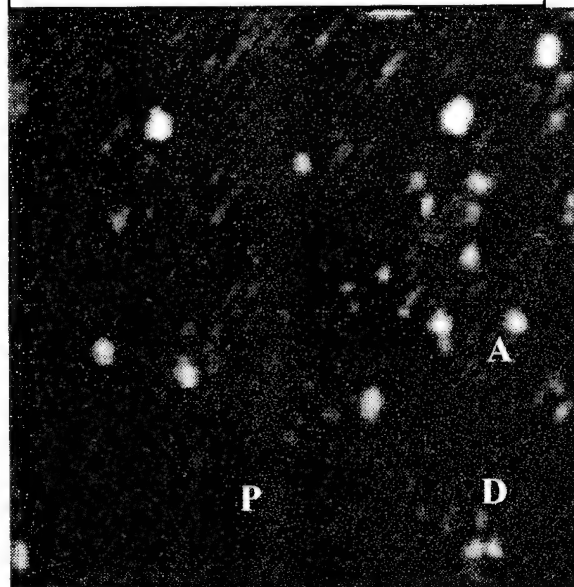
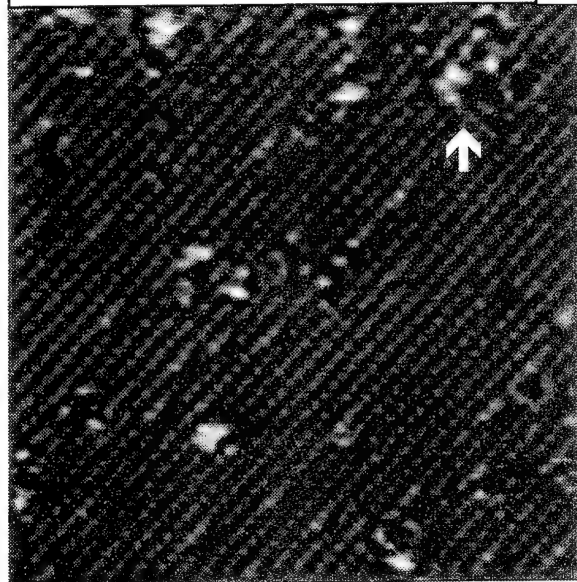


Figure 1

(c) 3 keV Ar⁺; 5.4×10^{12} ions/cm²



(d) 5 keV Xe⁺; 2.7×10^{12} ions/cm²

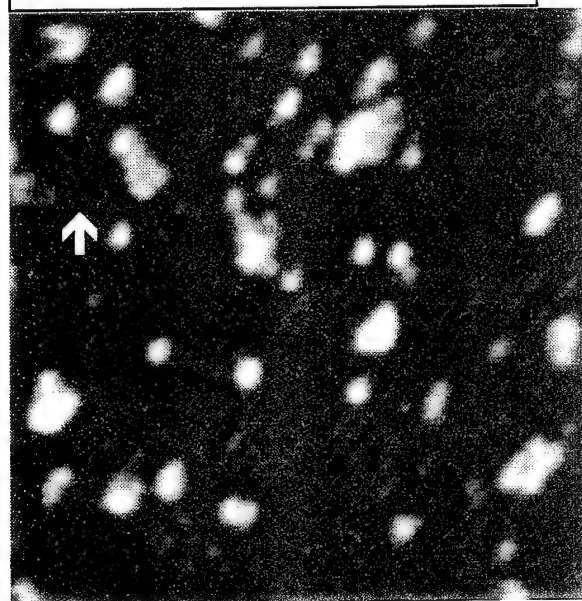


Figure 1

(a) 500 eV Xe⁺, 2.7×10^{12} ions/cm², [100]



(b) 3 keV Xe⁺, 1.3×10^{12} ions/cm², [111]

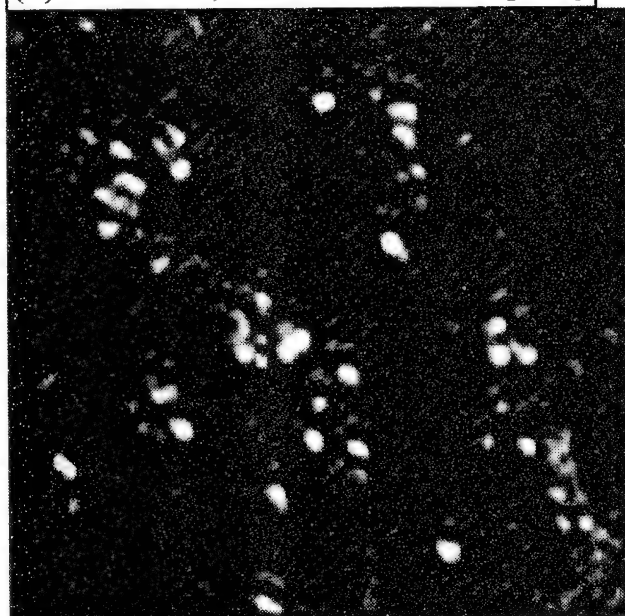


Figure 2

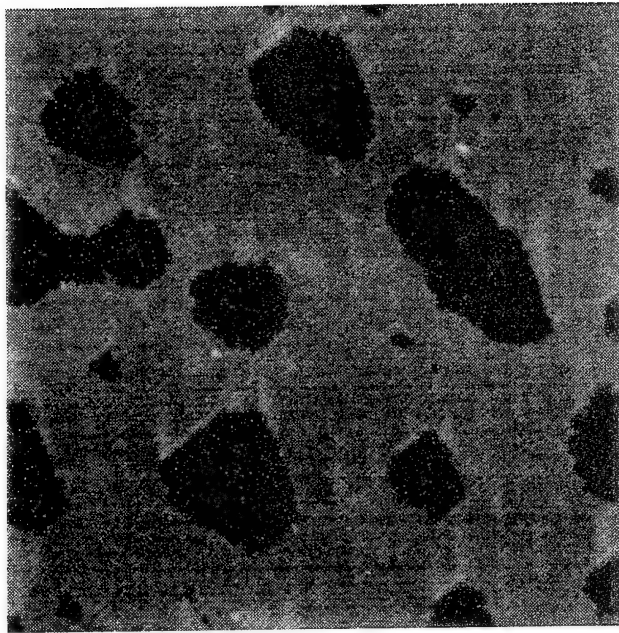


Figure 3

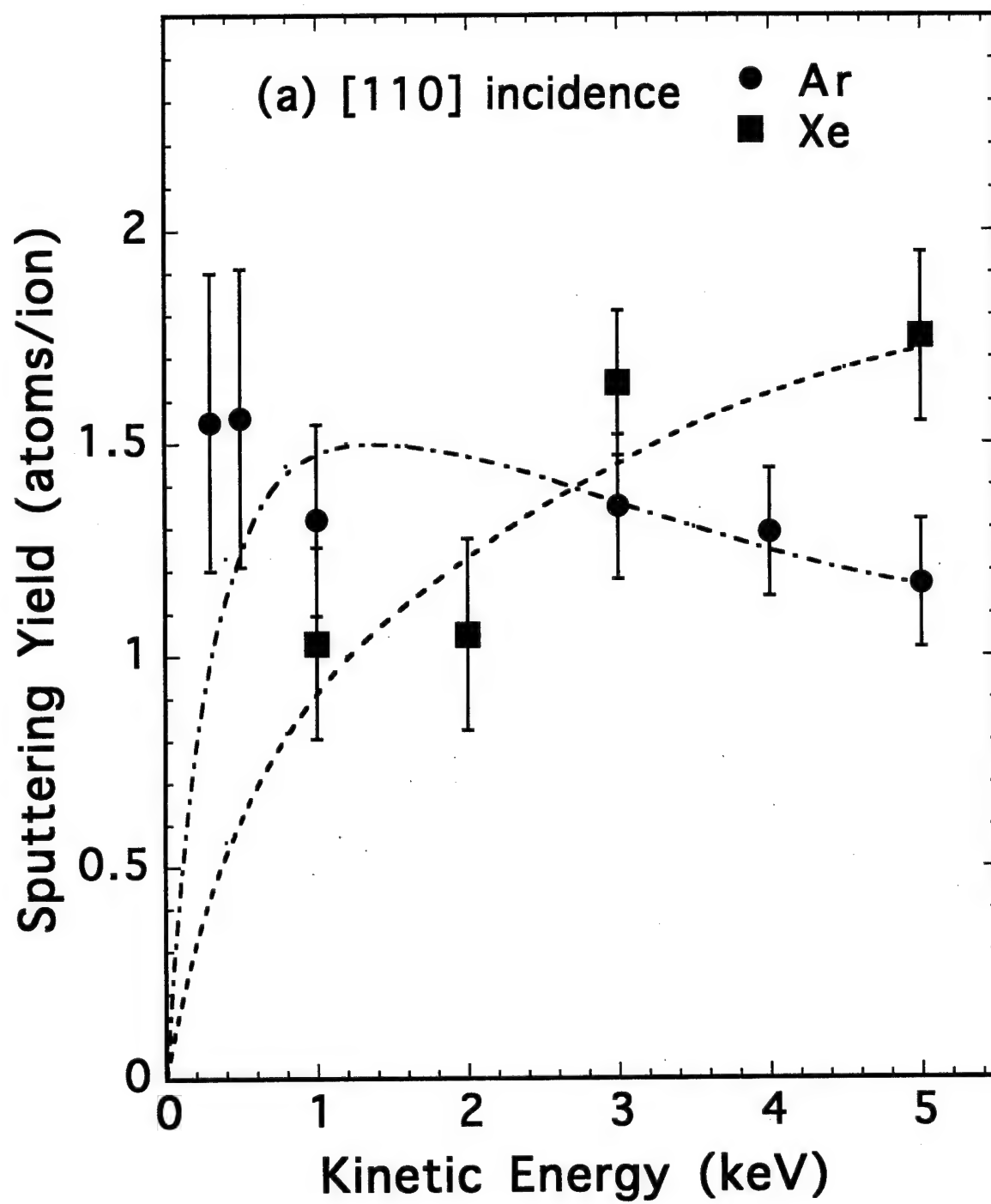


Figure 4(a)

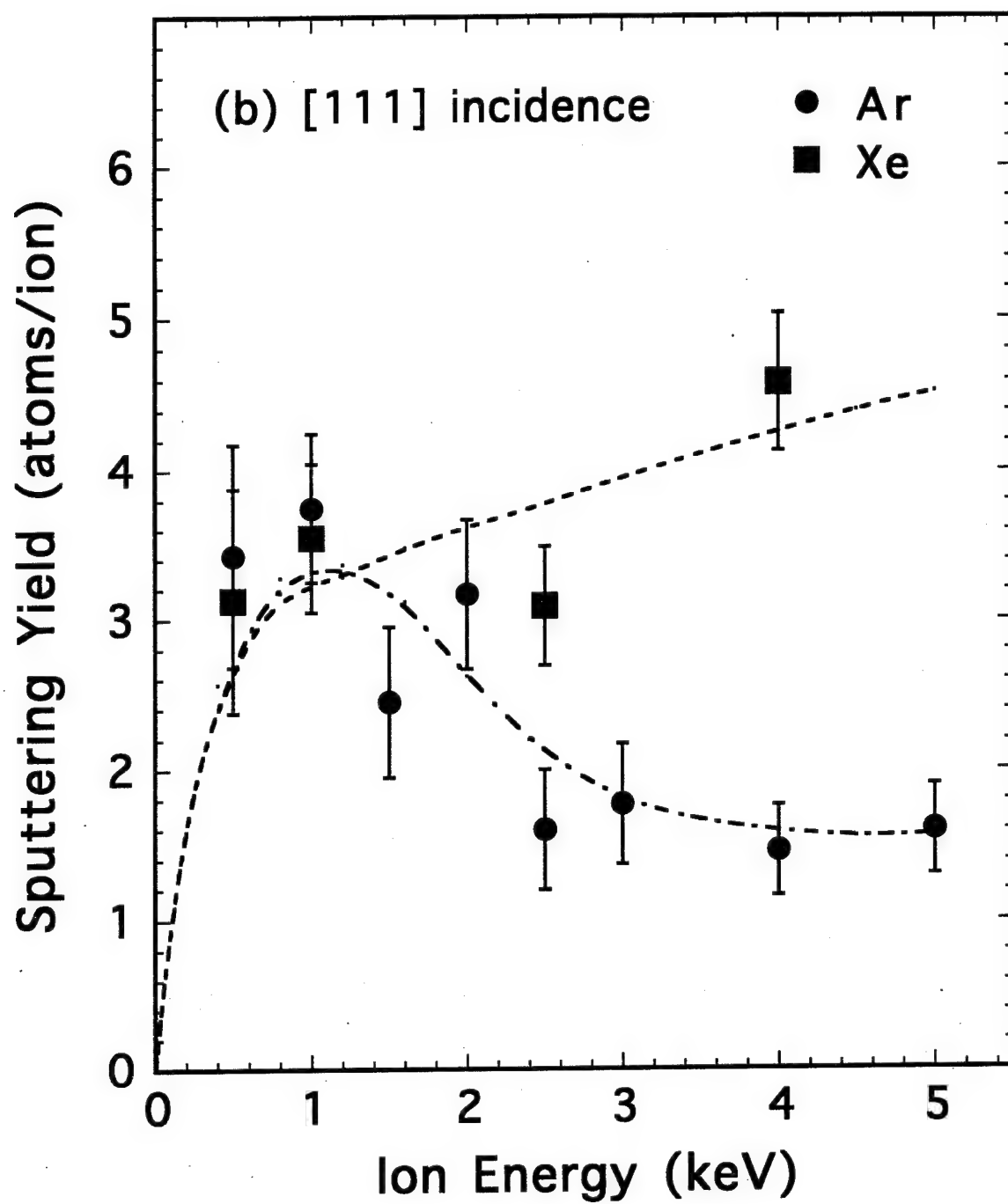


Figure 4(b)

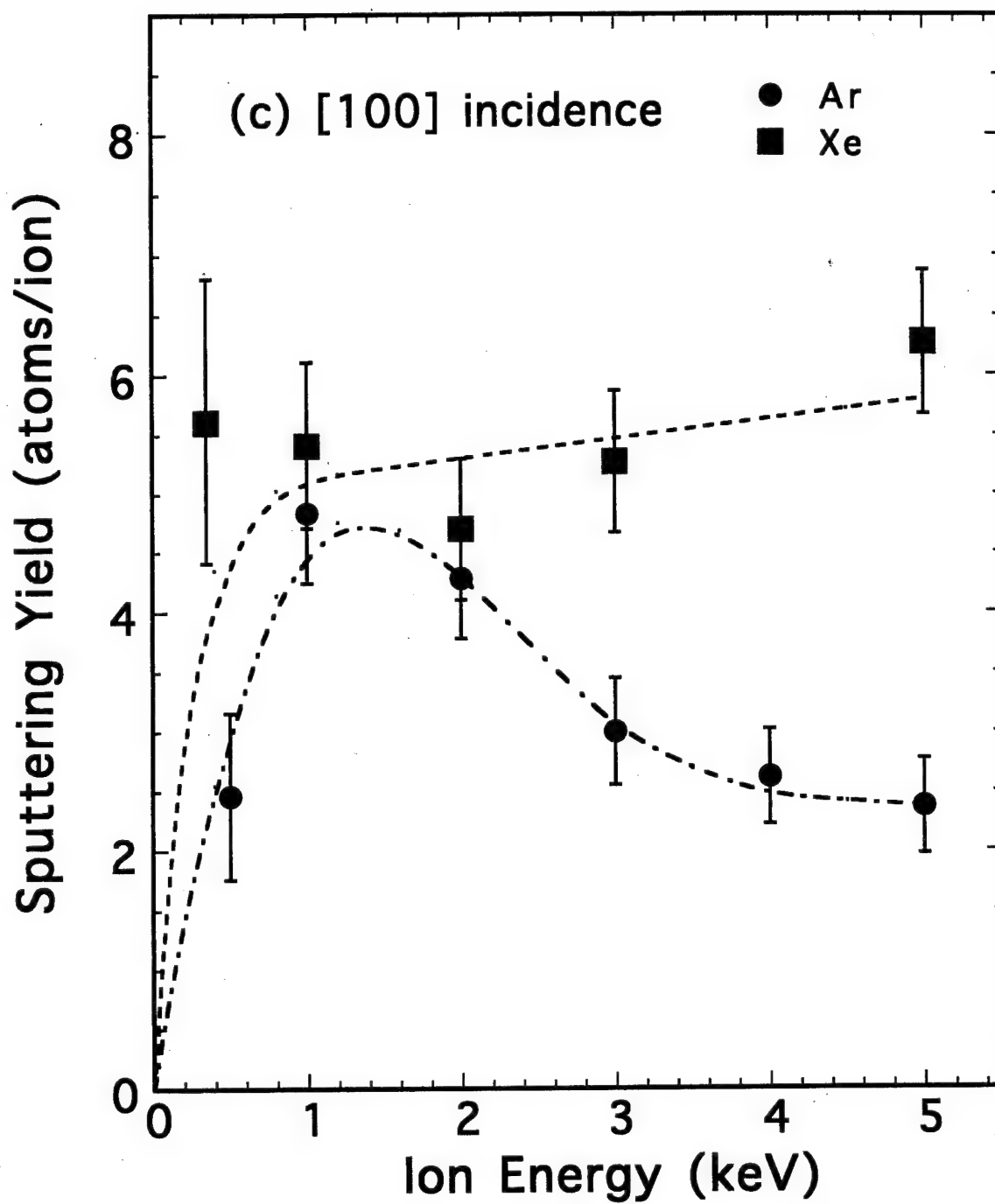


Figure 4(c)

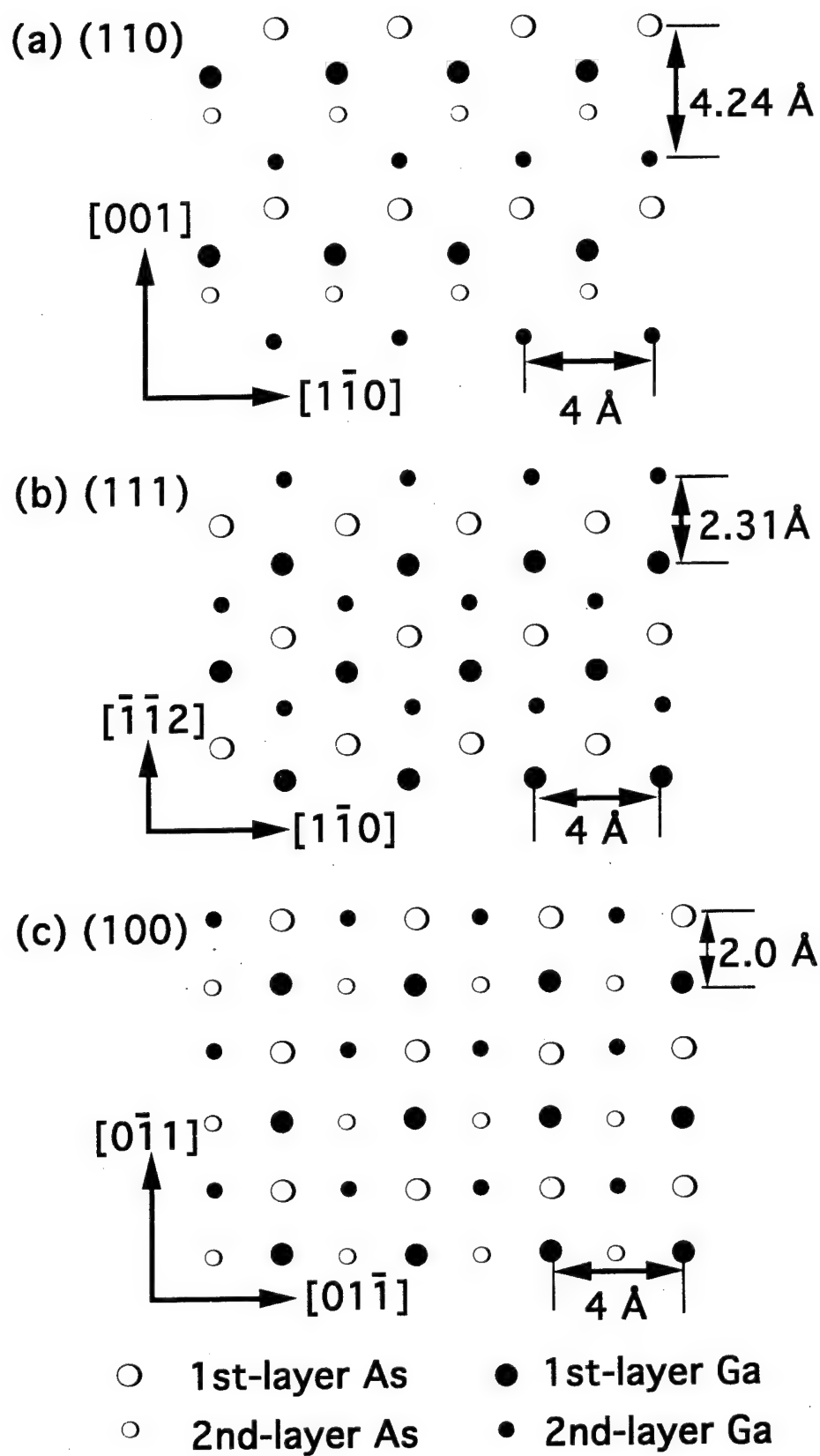


Figure 5

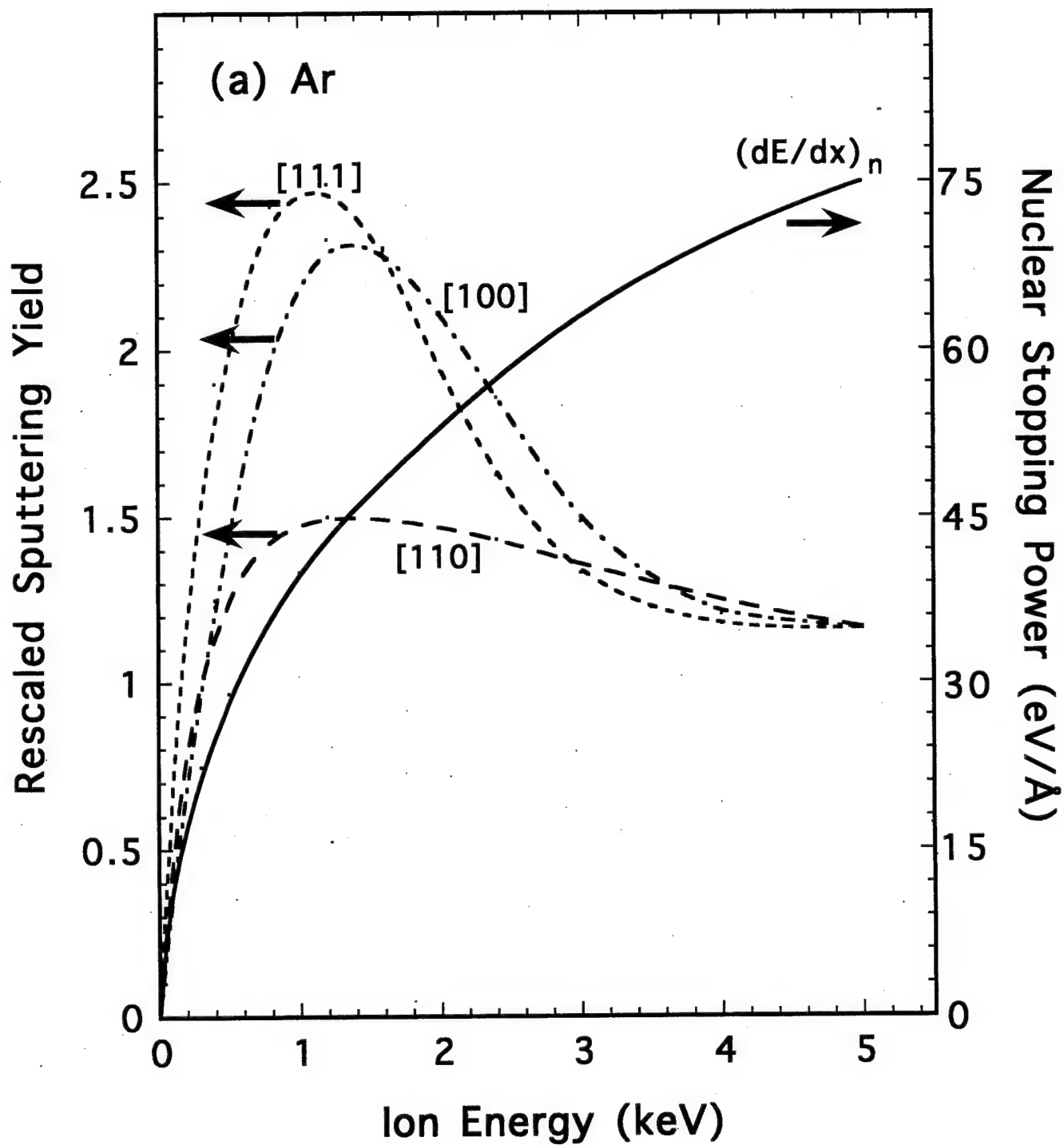


Figure 6(a)

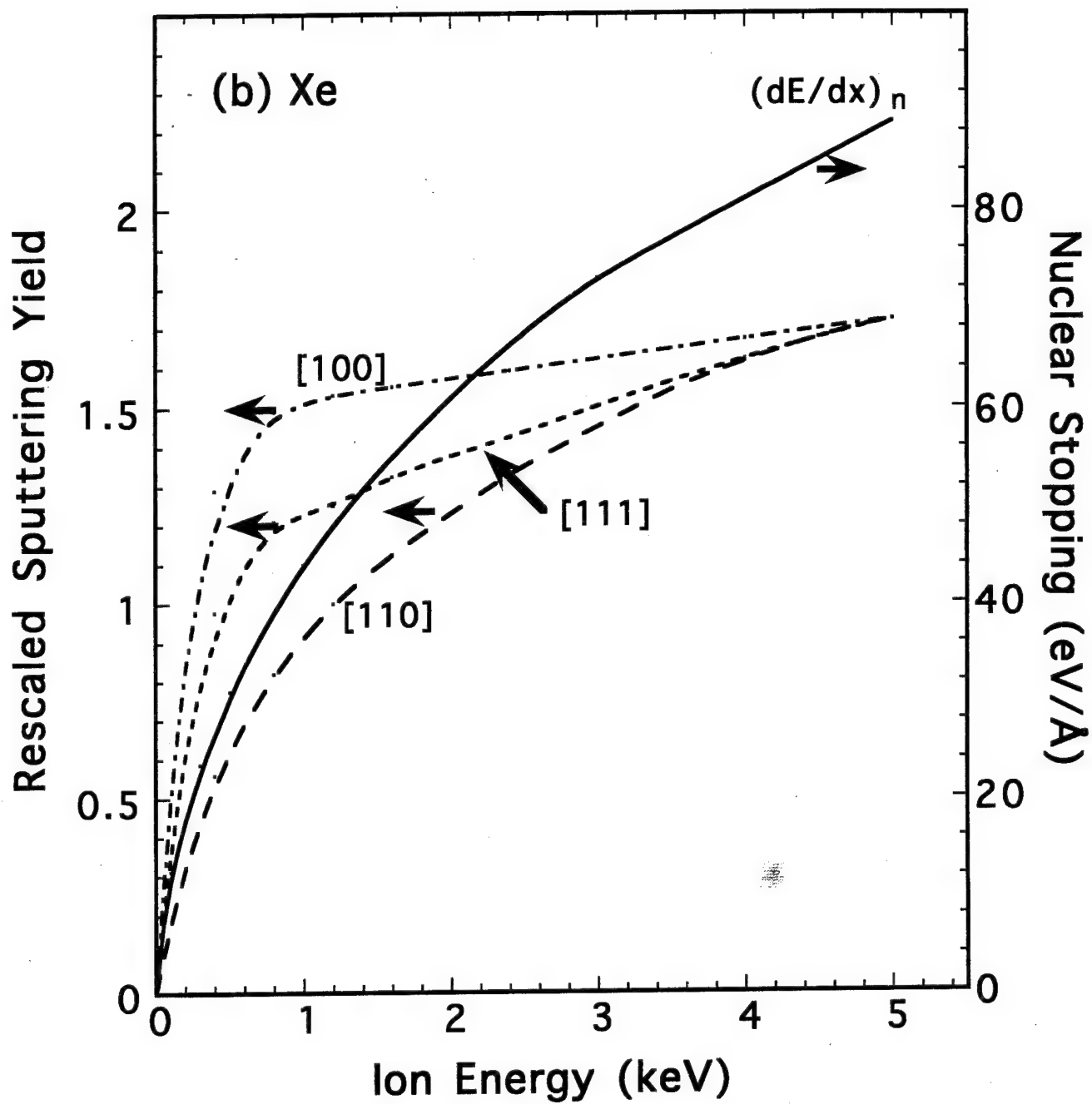


Figure 6(b)

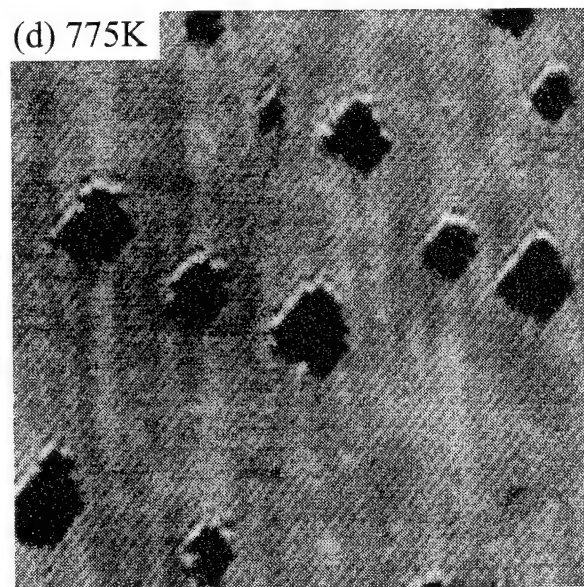
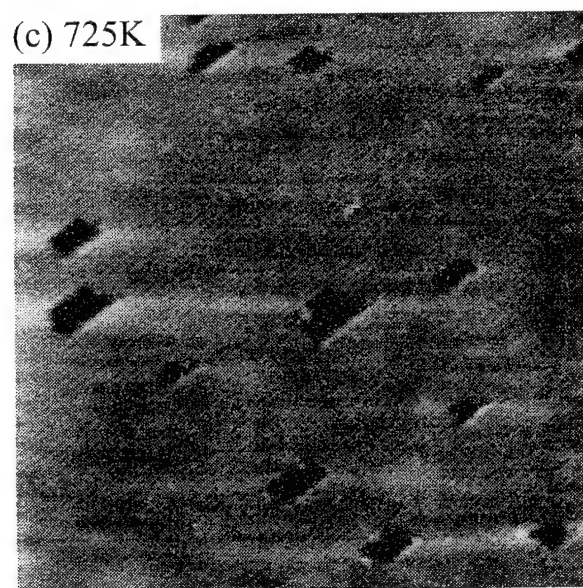
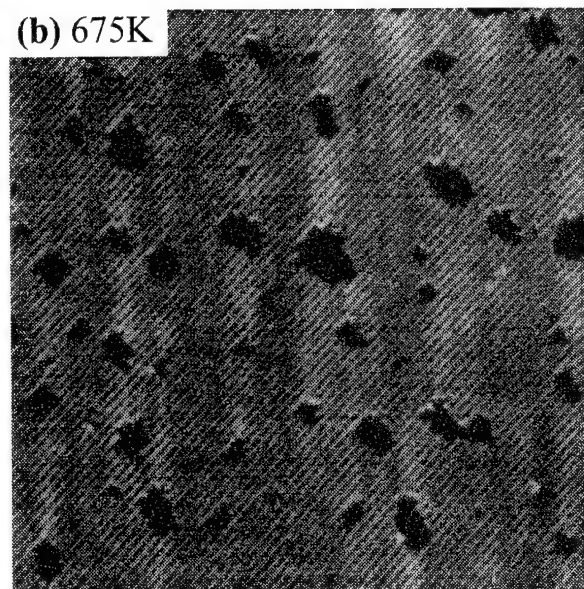
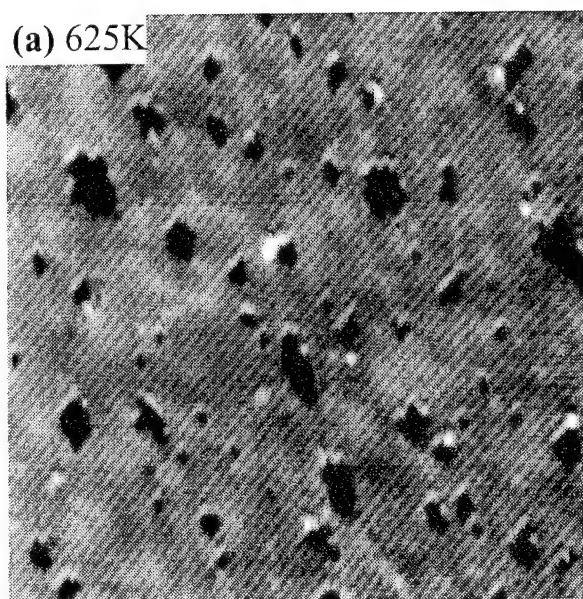


Figure 7

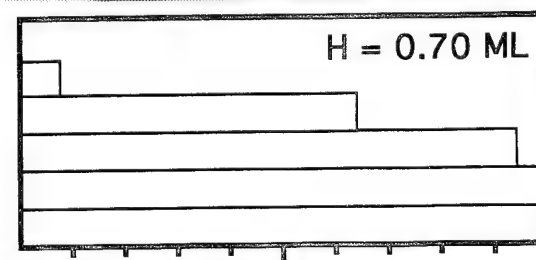
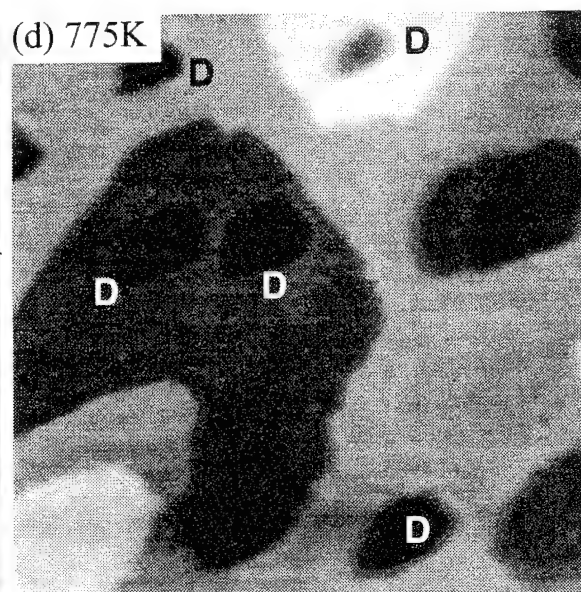
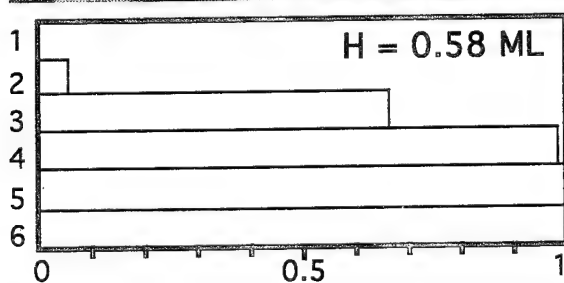
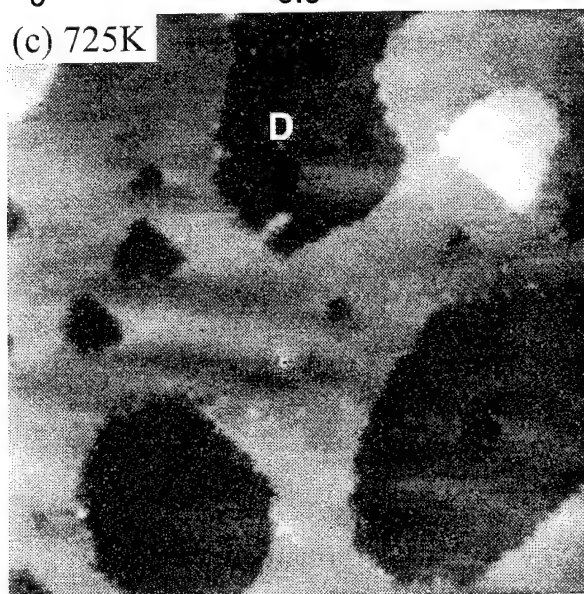
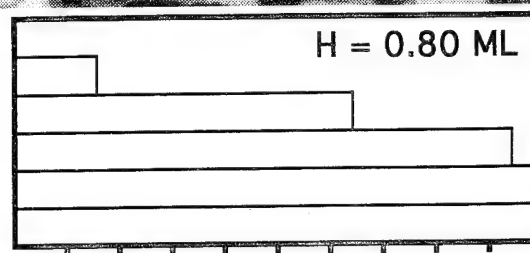
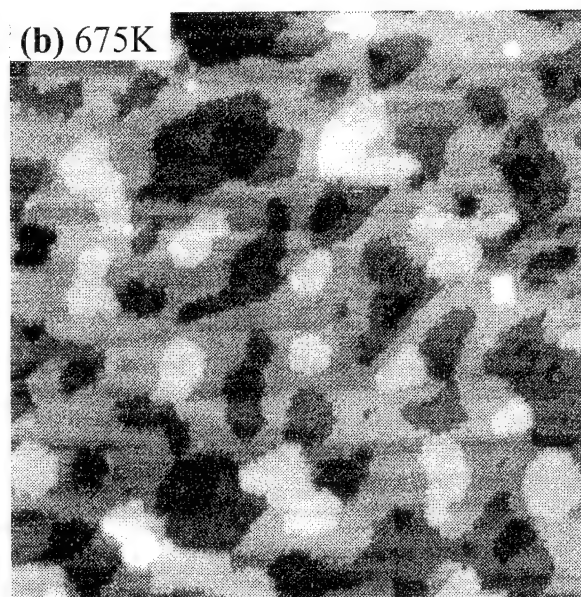
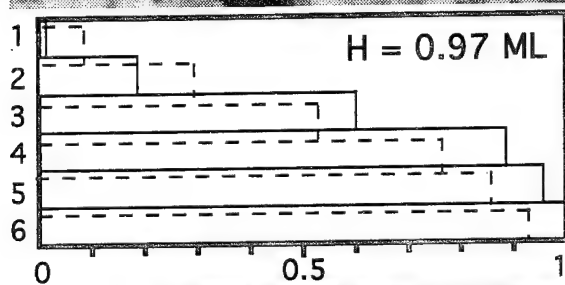
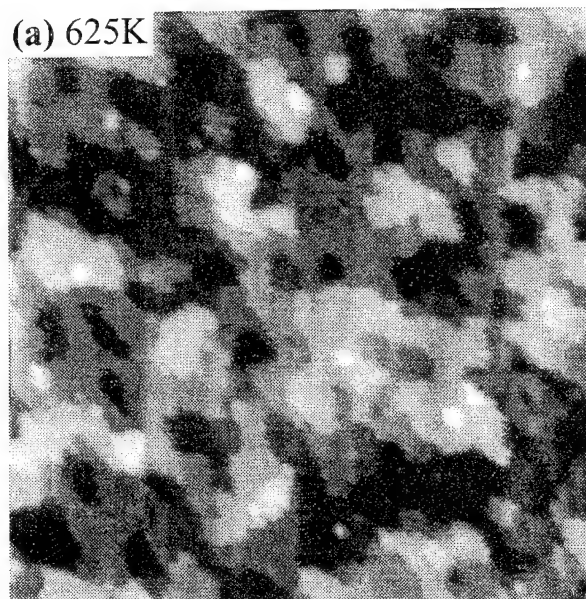


Figure 8

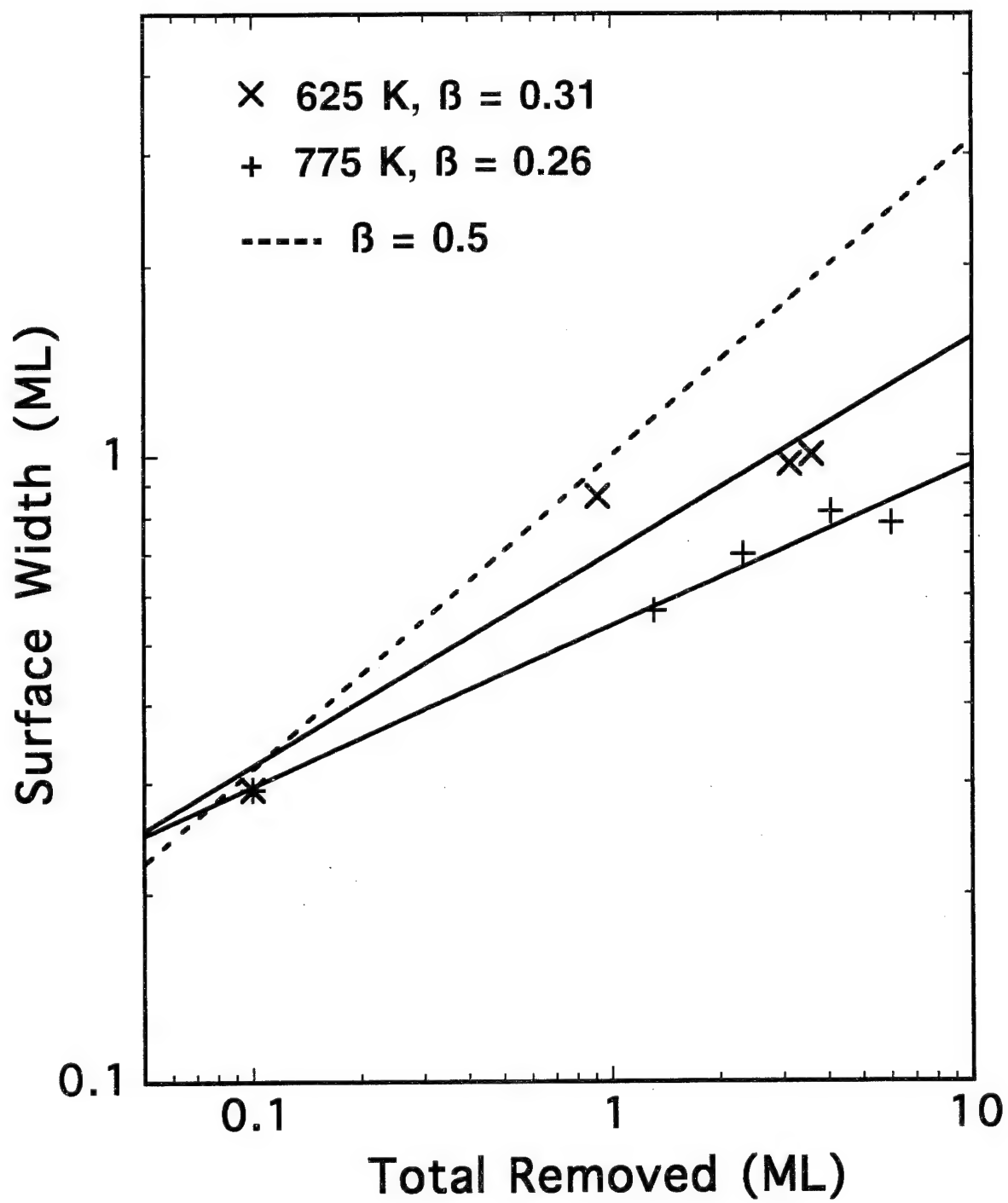


Figure 9

Appendix 5

Preprint of "Trends in Surface Roughening:
STM Analyses of Ion-sputtered GaAs(110)"

X.-S. Wang, R.J. Pechman, and J.H. Weaver

Submitted to Phys. Rev. Lett.

Trends in Surface Roughening: Analysis of Ion-sputtered GaAs(110)

X.-S. Wang, R.J. Pechman and J.H. Weaver

Department of Materials Science and Chemical Engineering
University of Minnesota, Minneapolis, MN 55455

ABSTRACT

The effects of diffusion kinetics on surface roughness were investigated by measuring the dependence of surface width and step density on the amount of material removed for GaAs(110) sputtered at different temperatures (T). Surfaces after several monolayers of material removal at 625 K were rougher on a small scale than those at 725 K, but they were smoother on a large scale. The increased large-scale roughness at high T was caused by increased diffusion on terraces and along step-edges but insufficient cross-step transport.

PACS: 61.50.Cj, 68.35.Bs, 68.35.Fx, 61.16.Di

Atomic level understanding of the surface morphology during crystal growth and sputtering is interesting from a scientific perspective and it has important applications.^{1,2} In growth processes, atoms arrive at random locations. Similarly, surface atoms are removed randomly during ion sputtering, and vacancies are generated.³ When the temperature is too low for the surface to achieve thermal equilibrium, diffusion and nucleation of these randomly-distributed species determine the surface morphology, along with the rate of deposition or sputtering. While it is often considered that increased diffusion will yield a smoother surface, diffusion takes various forms that have different effects on surface roughness at different T . Quantitatively, the morphology is characterized by surface height h as a function of lateral coordinates x , and roughness is measured by surface width w as

$$w(L, \tau) = \langle h^2(x) - \langle h(x) \rangle^2 \rangle^{1/2} \quad (1)$$

where $\langle \rangle$ denotes an averaging across the sampling area, L is the sampling size, and τ is the duration of sputtering (a measure of total amount of material removed).

The function $w(L, \tau)$ reflects the variation of surface-width with sputtering duration and the surface roughness observed at different lateral scales. The latter is important, for example, in transport in quantum structures.⁴ It has been widely accepted that w obeys the general scaling form^{1,2} $w \sim L^\alpha$ for large τ and small L and $w \sim \tau^\beta$ for large L and small τ where α and β are related to the surface transport mechanism. Several analytical models have been proposed to describe mass transport on surfaces,^{1,2,5} and different values of the scaling exponents have been derived. Computer simulations have been performed to highlight the roles of certain transport mechanisms.^{1,2,5,6} Experimental studies of kinetic roughening have been carried out using diffraction probes^{7,8} and real-space microscopy⁹ such as scanning tunneling microscopy (STM). Despite progress in understanding kinetic roughening, practical difficulties have limited the validity of these studies. For example, in both experimental and theoretical studies, only the scaling exponents were evaluated, instead of the complete function $w(L, \tau)$.

It is also a formidable task to describe accurately the various mass transport mechanisms in analytical Langevin equations.^{1,5} The effects of changing activation of various transport avenues at different T have been considered only rarely.^{5,10} Understanding these effects is crucial to

explain different morphologies for various solids and processing conditions. In principle, desirable materials could be prepared rationally based on this understanding. A particularly interesting phenomenon found recently in kinetically-limited epitaxy is reentrant layer-by-layer growth,^{11,12} the origin of which was suggested to be reduced island size and irregular shape, which enhance interlayer mass transport. The general implications of reentrant layer-by-layer growth have not been elucidated.

Here, we report results of STM investigations of GaAs(110) sputtered with low-energy ions. Complete evaluation of the function $w(L, \tau)$ shows that w increases as L^α for small L for a given τ with $\alpha = 0.38$ describing results obtained over a wide range of sputtering conditions. w becomes constant beyond a length L_c termed the correlation length. L_c increases rapidly with τ at high temperature. For $L \geq L_c$, the relation $w \sim \tau^\beta$ fits well at high T but the exponent decreases at lower T for large τ . Accordingly, the roughness at large scales is larger at higher temperature than that at lower T after substantial material removal. Further, the step density increases rapidly until about 1 monolayer (ML) of material removal, and the step density depends sensitively on T . In a certain range of T , large and compact-shaped islands are formed due to a significant increase in *intralayer* diffusion, but a large barrier for cross-step diffusion (Schwoebel barrier¹³) suppresses *interlayer* mass transport. *This trend in surface roughening should be general, as long as the Schwoebel barrier is relatively large. In the extreme, it becomes reentrant layer-by-layer growth (or sputtering as observed here).*

The experiments were performed in an ultrahigh vacuum chamber (base pressure 2×10^{-10} Torr) with STM and low-energy electron diffraction. GaAs(110) surfaces were prepared by cleaving single crystals. The surfaces were exposed to ions from a degassed differentially-pumped ion gun. Impact from high purity Ar or Xe gave equivalent results.³ The chamber pressure was in the 10^{-9} Torr range during bombardment. The ion energy was 2 keV and the flux was $\sim 5 \times 10^{11} \text{ cm}^{-2}\text{s}^{-1}$. The yield with normal incidence ions was constant in the range 300-3000 eV.³ During bombardment, the sample was heated to 625-775 K (accuracy ± 20 K, reproducibility ± 10 K). The samples were cooled to 300 K after bombardment for STM imaging.

Low-energy ions generate mostly pits spanning 1-5 unit-cells on GaAs(110).^{3,14} For $T >$

625 K, impact-induced disorder is healed as pits migrate to form vacancy islands. Here, we measured layer coverages and step densities as a function of T and τ . Such direct measurements eliminate the need to use model-dependent assessments, as in diffraction experiments.^{7,8} Surface widths were calculated using

$$w = \{\sum(\theta_i - \theta_{i-1})(i-1)^2 - [\sum(\theta_i - \theta_{i-1})(i-1)]^2\}^{1/2} \quad (2)$$

where θ_i is the coverage of the i th layer and w is expressed in monolayer units where 1 ML = 2.0 Å for GaAs(110). This can be derived by considering a sampling area of one unit with layer coverage given by θ_i .¹⁵ The height of the top-most layer is zero. $\tau = \sum(1 - \theta_i)$, and the summation is for $i \geq 1$. We note that τ was typically evaluated in a step-wise fashion where less than 2 ML were removed between measurements for a given T . In this manner, the original top layer could be identified at all stages of removal. Comparison of surfaces continuously sputtered to those sequentially sputtered showed no difference in roughness parameters for the same τ .

Figure 1(a) displays an STM image obtained after 1.4 ML removal at 725 K. About 3% of the original top layer remains as isolated monolayer islands. There are vacancy islands as large as 300 Å in the second layer ($\theta_2 = 0.58$), and small vacancy islands appear in the third layer ($\theta_3 = 0.98$). The surface width is 0.6 ML. The step density, determined by measuring the perimeters of these islands, is $1.9 \times 10^6 \text{ cm/cm}^2$ (or cm^{-1}). Figure 1(b) represents a surface after sputtering to remove 10 ML at 725 K. Ten layers were exposed, w increased to 1.8 ML, and the step density was $2.9 \times 10^6 \text{ cm}^{-1}$. The fact that many terraces extend over 200 Å indicates that there are flat regions on a small scale.

The surface roughness evolves differently at 625 K. Initially, w grows rapidly as deeper-layers are exposed and outer-layers are removed more slowly. The step density also increases quickly as many small-size and rough-edge vacancy islands are formed. At $\tau = 1.8 \text{ ML}$, about 6% of the original surface layer remained while 20% of the third layer and 4% of the fourth layer were sputtered [$w = 0.9 \text{ ML}$ and step density $5.5 \times 10^6 \text{ cm}^{-1}$, Fig. 1(c)]. These roughness parameters increased slowly with additional bombardment at 625 K. Figure 1(d) represents a surface where 10 ML had been removed at 625 K, characterized by 10 partial layers with $w = 1.8 \text{ ML}$ and a step density of $5.7 \times 10^6 \text{ cm}^{-1}$.

The height variations over small scales (~ 200 Å) are within 2 Å for most areas at 725 K (Fig. 1(b)) and within about 5 Å at 625 K (Fig. 1(d)). The height fluctuations increased with sampling size, as summarized in Fig. 2. For each T and τ , w increases with L initially and reached saturation at some length $L = L_c$, where L_c is termed as the height-correlation length. For $L < L_c$, each set of data can be fitted with L^α where $\alpha = 0.38 \pm 0.03$, which is close to the simulation result based on the model of Kardar *et al.*^{1,5} Once L_c and w are known at one point of $L < L_c$, the function $w(L)$ can be mapped out. For $L = 100$ Å, Fig. 2 shows that, at 625 K, w increased from 0.8 ML for $\tau = 1.8$ ML to 1.2 ML for $\tau = 10$ ML. w increased from 0.4 ML to 0.8 ML in the similar range of τ at 725 K for $L = 100$ Å. The rate of increase at 725 K is faster than at 625 K at small scales. Furthermore, L_c at 725 K increased from 200 Å to more than 1000 Å in this range of τ , as plotted in the inset of Fig. 2, but it increased only from 100 Å to 250 Å at 625 K. An overall-smoother surface is produced after multilayer sputtering at lower temperature because of the relatively slow increase of w with τ at a given $L < L_c$, and of L_c with τ at lower T . This trend is demonstrated at $\tau = 10$ ML because the surface width at 725 K exceeds that at 625 K when sampled at 1000 Å. For higher T , and in particular at 725 K, the surface width increased as $w \sim \tau^\beta$ with $\beta = 0.3$ over the entire range of measurement.

The step density provides additional insight into kinetic roughening. Figure 3 summarizes the measured step density after sputtering at $625 \leq T \leq 775$ K. The scatter reflects the uncertainty in temperature during sputtering, and the lines represent fits to the data. The fits are logarithmic except at 625 K where the rate of increase is slower.⁷ The step density increases rapidly during the early stages of material removal but the changes are more gradual at higher τ . Likewise, there is a large variation in step density at a given τ , reflecting strong influence of T on the sizes of islands and terraces. Surface roughness on small-scales also varies with T and τ since it is closely related to the step density. Specifically, for $\tau > 1$ ML, Figs. 2 and 3 demonstrate that w increased little with τ at 625 K for small lengths as the step density reached a saturation value, while at 725 K the increase of w with τ was significant as the step density showed noticeable growth.

The observed trends in roughening result from the interplay between intralayer and interlayer diffusion. In *intralayer* diffusion, species migrate on terraces or along step-edges. Terrace

diffusion leads to island nucleation and growth, while step edge diffusion changes the island shape. For this system, Pechman *et al.*¹⁴ deduced that the activation energy for vacancy diffusion on terraces is 1.3 ± 0.2 eV and it is likely that the barrier for edge migration is lower because less bond-breaking is involved. In *interlayer* diffusion, vacancies must diffuse to a step edge and must overcome a barrier associated with the jump from a lower to a higher layer. Collectively, the extra barriers associated with such an interlayer process is called the Schwoebel barrier.¹³ While it is the key to reduced surface width,¹⁰ it restricts interlayer vacancy transport. Terrace and edge diffusion occur more frequently than cross-step jumping since the barriers are lower. We also note that atoms rarely detach from step edges and move on terraces at low temperature, except for unstable small-size islands.

When the Schwoebel barrier is large, an increase in T will promote terrace and edge diffusion and will have relatively little effect on cross-step motion. As a consequence of facile terrace and edge diffusion, a small number of large and compact vacancy islands with smooth edges will be formed. Hence, the surface-height variation will be small on a small scale and the step density will be low. However, large-scale roughness should not improve since cross-step diffusion increases very little. Furthermore, due to the low step density, vacancies meet with step-edges less frequently and cross-step transport is suppressed. Thus, the probability of lower-level vacancy island nucleation increases relative to that of vacancy jump-up in a large vacancy island. On the other hand, vacancies on higher-level terraces migrate quickly to the edge and annihilate at steps, instead of nucleating new vacancy islands. These tendencies enhance height variation at large scales, and small-scale height variation should grow steadily with further sputtering. At lower temperature, the decrease in terrace and edge diffusion leads to many small-size rough-edge terraces with a high step density. This increases cross-step diffusion. Here, the trend in large-scale roughening at high T is reversed. Although diffusion rates are relatively low, a steady-state is maintained on such a high-step-density surface, i.e., w on a small scale does not increase significantly after 1-2 ML have been removed. High-step density and short diffusion ranges also limit L_c whereas the large diffusion ranges at high T lead to large L_c that increases rapidly with τ .

The above mechanisms are similar to those proposed by Poelsema *et al.*¹¹ for reentrant layer-by-layer growth of Pt on Pt(111). On GaAs(110), however, these mechanisms only reduce the increase rate of w at lower T , instead of achieving layer-by-layer removal. We expect that this is a more general manifestation of the interplay of different mass transport mechanisms. The reentrant layer-by-layer growth (or sputtering) is then an extreme case in which interlayer mass transport is probably enhanced by additional factors, such as a reduced Schwoebel barrier at kinks, instability of small clusters,¹¹ and the tendency to form fractal branches.¹⁶ Finally, this trend of surface roughening should be observed only within a limited temperature range. Above this range, atoms detach from step edges at a sufficient rate to fill vacancy islands at lower levels, thus reducing the surface width.

The direct evaluation of the surface width and step density functions discussed here shows that the surface-width function is characterized by a power-law increase with sampling size up to a height-correlation length where it saturates. Both the height-correlation length and small-scale surface width increase significantly faster with material removal at 725 K than at 625 K. The step-density increases with the sputter duration, showing a rapid increase up to ~ 1 ML, then a slow growth. Within a certain temperature range, raising the temperature enhances intralayer diffusion significantly but interlayer transport is still frozen. This leads to a high rate of increase of the large-scale roughness. At lower T , the surface becomes rough at small scales during the early stages of sputtering as the step density increases because many small vacancy islands and terraces are formed. However, small-scale roughness changes little and height-correlation length increases at a slow rate with prolonged sputtering. Overall, surfaces sputtered at a higher- T become rougher than those at a lower- T on large scales. In some special systems, these trends are evident as reentrant layer-by-layer growth or removal. Since the controlling factor is a relatively large Schwoebel barrier, which is expected to exist for many surfaces, these trends should be considered when roughness on various scales is crucial.

The authors thank J. Brake for experimental assistance and Zhenyu Zhang for helpful discussions. This work was supported by the US Army Research Office.

REFERENCES

1. P. Meakin, Phys. Rep. **235**, 189 (1993), and references therein.
2. J. Lapujoulade, Surf. Sci. Rep. **20**, 191 (1994), and references therein.
3. X.-S. Wang, R.J. Pechman, and J.H. Weaver, Appl. Phys. Lett. **65**, 2818 (1994).
4. For example, N. Trivedi and N.W. Ashcroft, Phys. Rev. B **38**, 12298 (1988).
5. S.F. Edwards and D.R. Wilkinson, Proc. Roy. Soc. A **381**, 17 (1982); M. Kardar, G. Parisi, and Y.C. Zhang, Phys. Rev. Lett. **56**, 899 (1986); S. Das Sarma and P. Tamborenea, *ibid.* **66**, 325 (1991); Z.-W. Lai and S. Das Sarma, *ibid.* **66**, 2348 (1991); D.A. Kessler, H. Levine, and L. M. Sander, *ibid.* **69**, 3076 (1992).
6. H. Yan, D. Kessler and L.M. Sander, Phys. Rev. Lett. **64**, 926 (1990); H.C. Kang and J.W. Evans, Surf. Sci. **269**, 784 (1992); M. Kotrla, A.C. Levi, and P. Smilauer, Europhys. Lett. **20**, 25 (1992); P. Smilauer, M.R. Wilby and D.D. Vvedensky, Surf. Sci. **291**, L733 (1993).
7. Y.-L. He, H.-N. Yang, T.-M. Lu, and G.-C. Wang, Phys. Rev. Lett. **69**, 3770 (1992); H.-N. Yang, G.-C. Wang, and T.-M. Lu, Phys. Rev. B **72**, 7635 (1994).
8. H.-J. Ernst, F. Fabre, R. Folkerts, and J. Lapujoulade, Phys. Rev. Lett. **72**, 112 (1994).
9. E. A. Eklund, R. Bruinsma, J. Rudnick, and R.S. Williams, Phys. Rev. Lett. **67**, 1759 (1991); J. Krim, I. Heyvaert, C. Van Haesendonck, and Y. Bruynseraede, *ibid.* **70**, 57 (1993); H. You, R.P. Chiarello, H.K. Kim, and K.G. Vandervoort, *ibid.* **70**, 2900 (1993); G. Palasantzas and J. Krim, *ibid.* **73**, 3564 (1994).
10. Z. Zhang, J. Detch, and H. Metiu, Phys. Rev. B **48**, 4972 (1993).
11. R. Kunkel, B. Poelsema, L.K. Verheij, and G. Comsa, Phys. Rev. Lett. **65**, 733 (1990), and B. Poelsema *et al.*, Appl. Phys. A **53**, 369 (1991).
12. H. Morkoc, T.J. Drummond, W. Kopp, and R. Fischer, J. Electrochem. Soc. **129**, 824 (1982); A.M. Dabiran, S.K. Nair, H.D. He, K.M. Chen, and P.I. Cohen, Surf. Sci. **298**, 384 (1993).
13. R.L. Schwoebel, J. Appl. Phys. **40**, 614 (1969).
14. R.J. Pechman, X.-S. Wang, and J.H. Weaver, Phys. Rev. B **51**, 10929 (1995).

15. X.-S. Wang, R.J. Pechman, and J.H. Weaver, J. Vac. Sci. Technol. B (submitted)
16. T. Michely, M. Hohage, M. Bott, and G. Comsa, Phys. Rev. Lett. **70**, 3943 (1993).

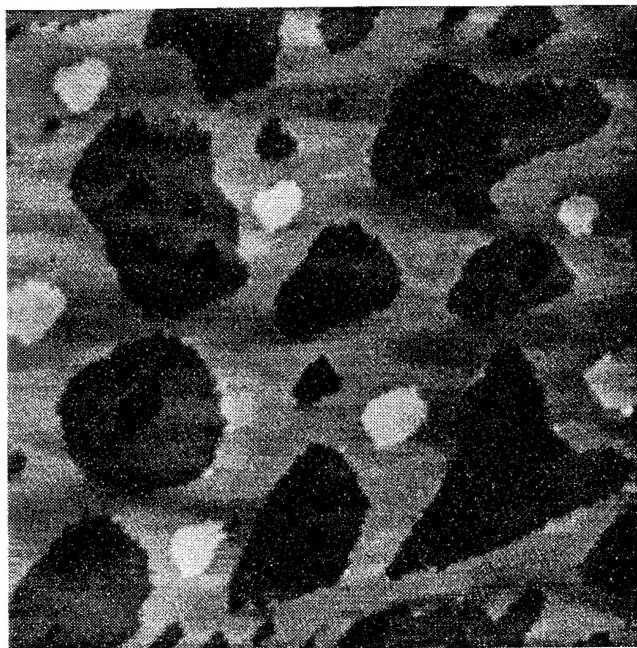
FIGURE CAPTIONS

FIG. 1 Filled-state STM images of GaAs(110) after Xe^+ sputtering at 725 K for (a) and (b), and 625 K for (c) and (d). Image size, measured amount of material removal (τ), and surface width (w) are given for each image. For low τ [(a) and (c)], sputtering at lower temperature yields a rougher surface. After prolonged sputtering [(b) and (d)], roughness measurements taken at large scales are comparable for high and low temperature.

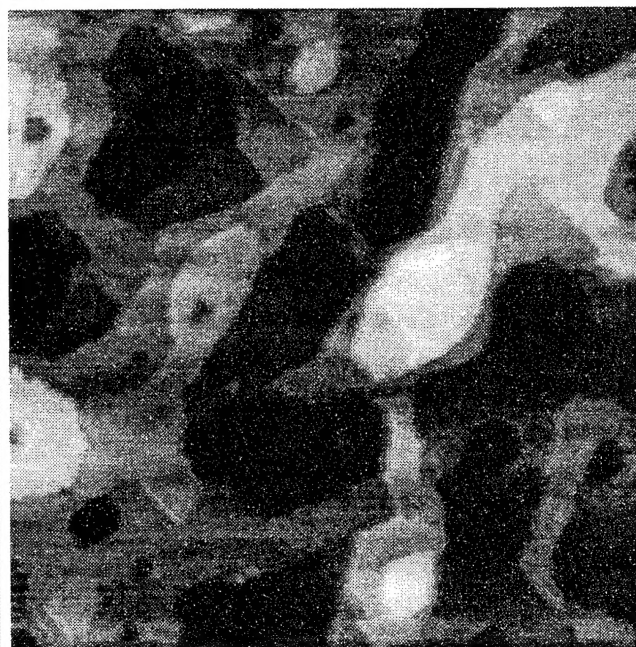
Fig. 2 Surface width as a function of sampling scale L measured for different amounts of material removal at 625 K and 725 K. The data fit a universal power-law $w \sim L^\alpha$ for small L with $\alpha = 0.38 \pm 0.03$. Above the correlation length (L_c) the surface width saturates at the large-scale value. Although surfaces sputtered at 625 K are initially rougher than those at 725 K, prolonged sputtering (up to 10 ML) yields rougher surfaces at high temperatures. The inset shows L_c as a function of τ at 625K and 725K. The dashed lines are guides-to-the-eye. The slower increase of L_c at 625 K indicates higher roughening at smaller scales which contributes to enhanced interlayer diffusion.

Fig. 3 Step densities as a function of amount of sputtering at different temperatures. Higher step density at lower temperature is indicative of small and irregularly-shaped islands. For all temperatures, the step density increases rapidly in the initial stages of sputtering. This increase slows for high τ . At 625 K, the step density saturates at a relatively low τ indicating improved interlayer transport.

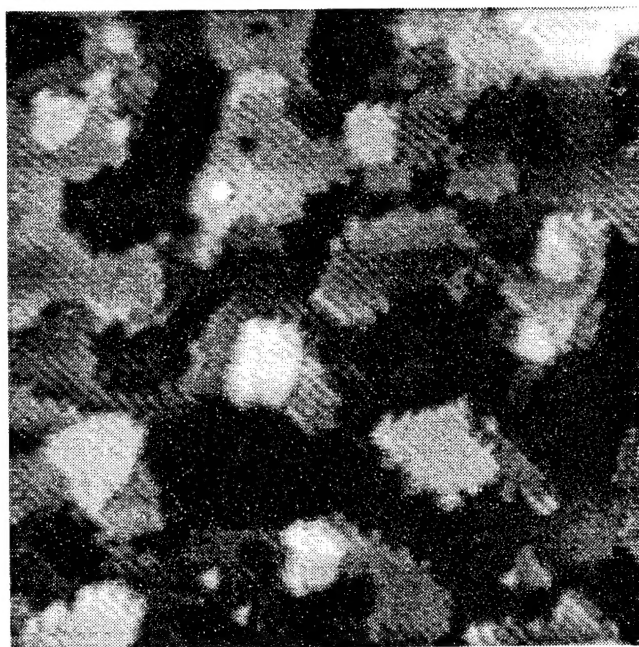
(a) 725K, 900Å, $\tau=1.4\text{ML}$, $w=0.6\text{ML}$



(b) 725K, 1080Å, $\tau=10\text{ML}$, $w=1.8\text{ML}$



(c) 625K, 450Å, $\tau=1.8\text{ML}$, $w=0.9\text{ML}$



(d) 625K, 1080Å, $\tau=10\text{ML}$, $w=1.8\text{ML}$

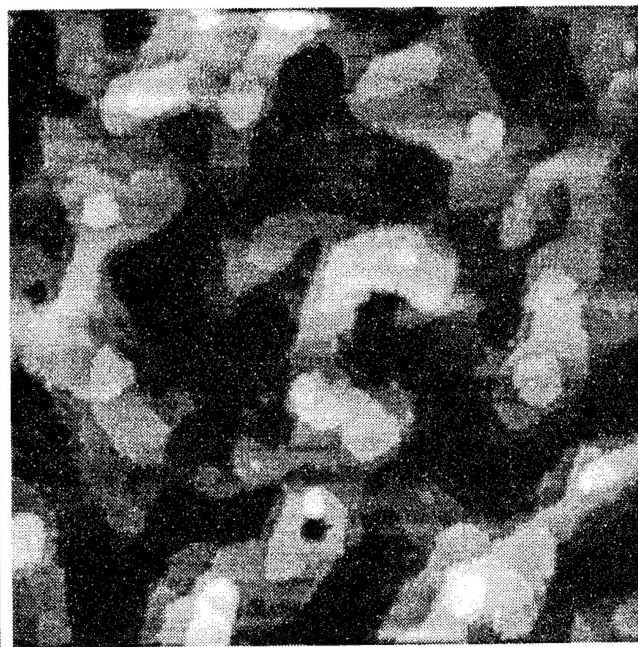


Figure 1

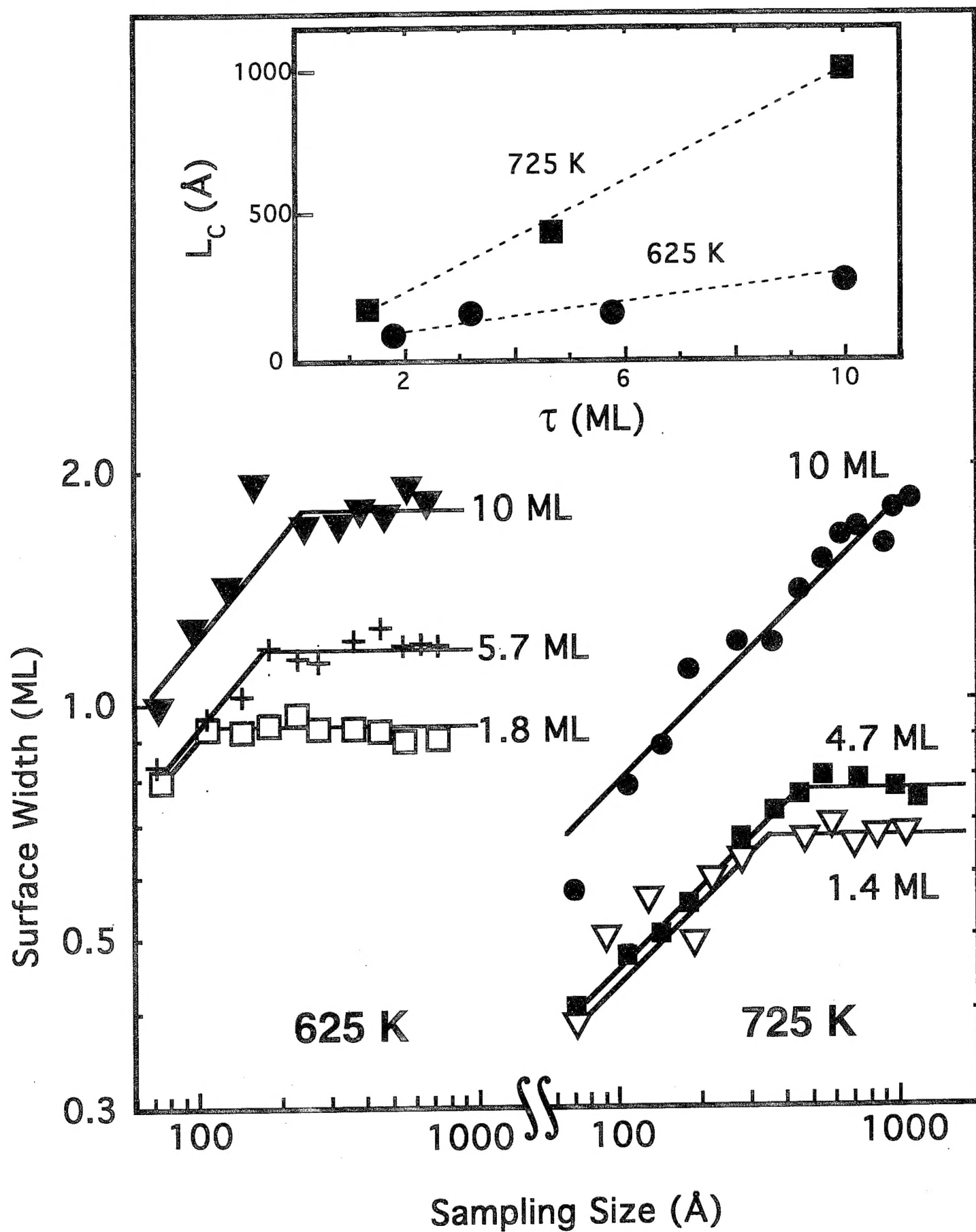


Figure 2

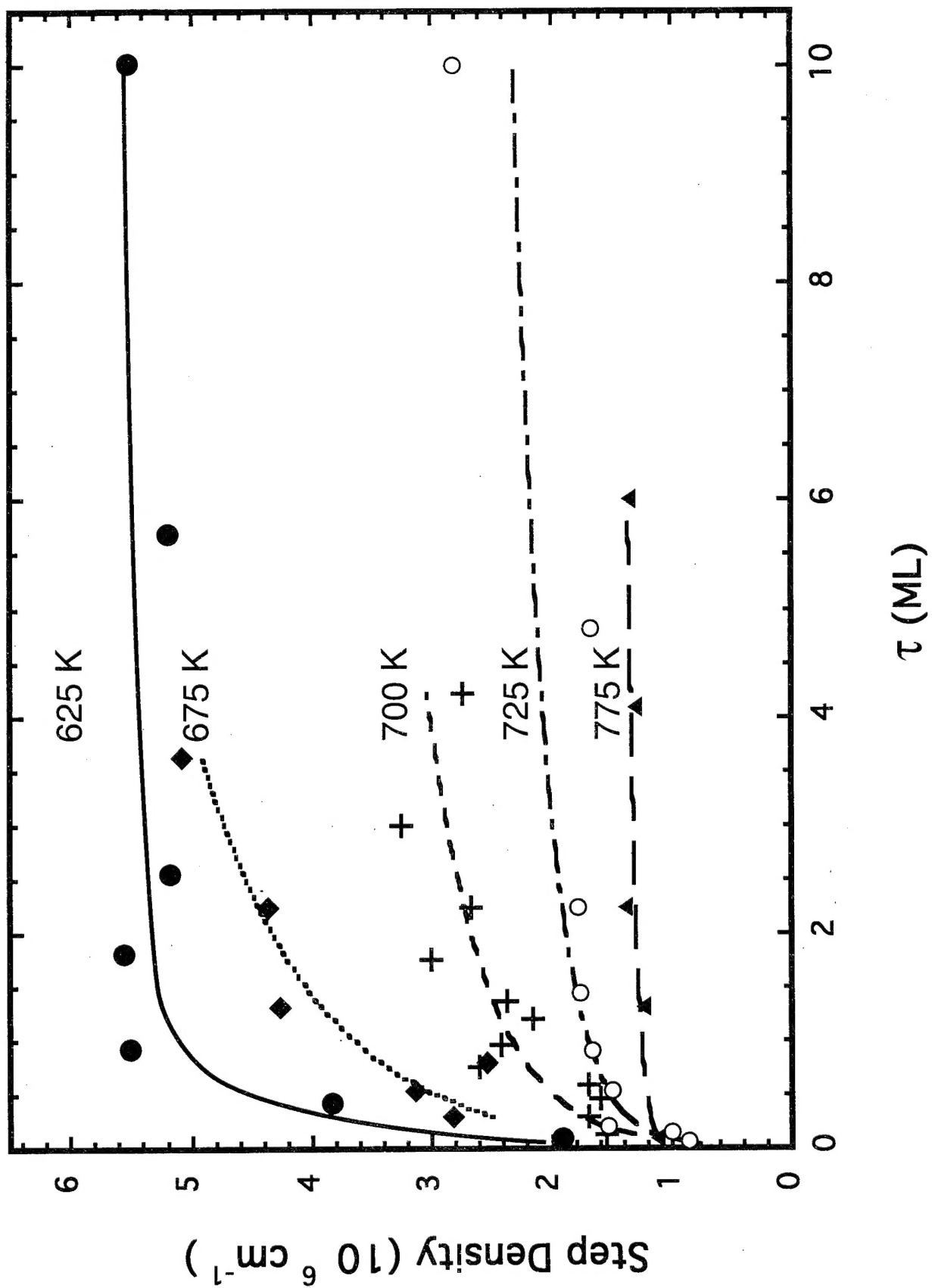


Figure 3